The Pennsylvania State University

The Graduate School

College of Engineering

A RECIPROCITY APPROACH FOR ANALYZING RADIATION FROM APERTURE AND MICROSTRIP ANTENNAS

A Thesis in

Electrical Engineering

by

Dean Yasuo Arakaki

Submitted in Partial Fulfillment
of the Requirements
for the Degree of

Doctor of Philosophy

May 2000

We approve the thesis of Dean Yasuo Arakaki.

Date of Signature

Raj Mittra
Professor of Electrical Engineering
Thesis Co-Advisor, Co-Chair of Committee

Douglas H. Werner
Associate Professor of Electrical Engineering
Thesis Co-Advisor, Co-Chair of Committee

Lynn A. Carpenter
Associate Professor of Electrical Engineering

Anthony J. Ferraro
Distinguished Professor Emeritus of Electrical Engineering

Raymond J. Luebbers
Professor of Electrical Engineering

Akhlesh Lakhtakia
Professor of Engineering Science and Mechanics

W. Kenneth Jenkins
Professor of Electrical Engineering
Head of the Department of Electrical Engineering

ABSTRACT

Conformal antennas, used extensively on mobile communications systems, generally have complex configurations and are often times mounted on or used within large structures. Hence, the modeling of such antennas is a challenging problem. The most frequently used numerical techniques either require excessive computational resources or cannot effectively model such structures. Thus, hybrid techniques have recently been employed to take advantage of each method’s strengths, while minimizing weaknesses.

To enhance computational efficiency, a new methodology is introduced in this thesis, based on a combination of the Finite Difference Time Domain (FDTD) and the Method of Moments (MoM) numerical techniques in conjunction with the Surface Equivalence and Reciprocity Theorems. Several antenna configurations are considered to illustrate the new methodology: 1) radiating slots on conducting cylinders, 2) microstrip patch antennas mounted on large conducting structures, and 3) reflector antennas with partial circular symmetry.

In the transmit mode, the region containing the radiation source is first analyzed using either the MoM or FDTD technique to determine “equivalent currents” at the radiating aperture. The Surface Equivalence Principle is then applied, allowing the material in the radiating region to be theoretically modified to match its surroundings. This creates a homogeneous structure for the first two antenna types, and a circularly symmetric structure for the last type.

The operation of the antenna system is then reversed to the receive mode, and the fields produced at the radiating aperture are determined. By analyzing this mode of operation, difficult integrals and asymmetric sources are avoided for antenna types 1 and 2, and 3, respectively. For antenna types 1 and 2, the MoM technique is used to compute the surface fields, which reduces computational resource requirements since the surface of the structure – as opposed to its volume – is modeled. For antenna type 3, the effective removal of asymmetric sources allows a 2-D FDTD simulation of the antenna structure, instead of a full 3-D model.

Finally, utilizing the Reciprocity Theorem, the surface fields determined for the receive mode case are combined with the “equivalent currents” calculated in the transmit mode in order to compute far-zone fields. Through use of the technique, computational savings on the order of 95% are realized.

TABLE OF CONTENTS

LIST OF FIGURES

ACKNOWLEDGMENTS

I am dedicating this thesis to my wife, Lisa, for her patience and constant support throughout my graduate studies. Without her encouragement over the years, the completion of this thesis would not have been possible. I would also like to thank my Dad, Mr. James Arakaki, for encouraging me to study electrical engineering and for his constant support of my educational endeavors.

I am grateful to my co-advisors, Drs. Raj Mittra and Douglas Werner for their patience, guidance, and support throughout the course of this research. I also thank my committee members for reviewing my thesis and administering the Comprehensive and Final Oral Examinations.

I appreciate the support and advice from members of the Electromagnetic Communications Research Laboratory at Penn State, especially Dr. Wenhua Yu, Mr. Sourav Chakravarty, Dr. Vladimir Veremey, and Mr. Yi Yang. I have benefited from our many discussions and the development of new ideas. I would also like to thank Dr. Karthikeyan Mahadevan for his help with the edge to surface current calculation program that we developed. I am also grateful for the support I received from Mr. Jeff Nucciarone in the use of the IBM RS/6000 SP computer at Penn State.

Finally, I would like to thank Mr. Jerry Chang, staff engineer at Hughes Aircraft Company, whom I worked with for four years. His skill in modeling electronic circuit phenomena served as an inspiration to me, and instilled in me a desire to improve my knowledge through graduate studies in electrical engineering.

Chapter 1

INTRODUCTION

Low profile conformal antennas used on mobile communications systems are receiving widespread attention due to the advantages of minimized aerodynamic friction and radar cross-section, reduced risk of antenna structural damage, and simplified construction requirements over conventional antennas. Conformal microstrip antennas were first proposed in 1953 by Deschamps [1] and patented in France in 1955 by Gutton and Baissinot [2]. Conformal antennas were shown to have useful practical applications on systems such as aircraft and rockets [3]; thereby initiating substantial interest and research into the understanding and design of conformal antennas. Analysis on basic rectangular and circular microstrip patch antennas was conducted in 1975 by Howell [4].

Since conformal antennas generally have complex configurations and are usually mounted on large structures, the modeling of such antennas continues to be a challenge. Simulation methods that excel at modeling complex structures require excessive computational resources when the problem geometry is large with respect to the wavelength. Alternatively, simulation techniques that are well-suited for the modeling of large arbitrarily-shaped structures are limited to structures composed of a low number of materials arranged in simple configurations. By using a combination of techniques, one can take advantage of the strengths of each method and simultaneously minimize the effects of any weaknesses. One of the chief concerns in using these hybrid methods is the design of the interface between the techniques. It must unite the various methods used with minimal effect on the accuracy and run-time efficiency of the computation.

This thesis describes a new hybrid method that uses a combination of the Finite Difference Time Domain technique (FDTD) [5] and the Method of Moments (MoM) [6]. In the first problem geometry – a conformal antenna mounted on a large conducting structure – the FDTD method is used in the region containing the conformal antenna, while the MoM technique is used to model the structure the antenna is mounted on. In the second geometry – a reflector antenna system – the MoM method is used to model the conformal microstrip feed antenna, while the FDTD technique is used to simulate the remainder of the reflector system. The interface between these two methods, in both cases, is provided by the Surface Equivalence and Reciprocity Theorems. The objective of this thesis and an overview of the proposed technique will now be presented.

1.1 Research Objective and General Technique

The objective of this thesis is to develop an efficient method for pattern computation. The geometries of interest are conformal antennas mounted on arbitrarily-shaped conducting bodies or used within large antenna systems.

The proposed hybrid technique is first verified on known canonical problems described in [7], followed by applications to geometries solvable by numerical methods only. For these cases, convergence to the canonical geometries is demonstrated.

For the first problem geometry, the proposed method is to be used within a design optimization loop for the attainment of a specified radiation pattern. This loop alters the patch shape and placement on the mounting structure as it optimizes. The computational efficiency is enhanced by utilizing the synergy of the hybrid method, which exploits the strengths of both the FDTD and the MoM numerical techniques. The FDTD method is initially used to determine the equivalent currents at the radiating aperture of the conformal antenna, followed by the application of the Surface Equivalence Principle, which allows closure of the aperture with perfectly conducting material. This results in a large conducting body of arbitrary shape, which is readily modeled by the MoM approach.

Simulation of the region containing the conformal antenna by a volume cell approach (FDTD), followed by a simulation of the mounting structure by a surface discretization method (MoM), results in computational resource savings of greater than 95%, when compared to an FDTD-gridded computational model of the entire geometry. Radiation pattern accuracy is maintained to within 1 to 2 dB when compared to patterns generated by alternate means [8]. In addition, when the proposed method is used within the patch antenna shape and location optimization loop mentioned above, further computational resource savings are realized, as only a portion of the entire model requires resimulation.

In the case of the reflector antenna system, the MoM method is used to compute equivalent currents at the radiating feed antenna. This is followed by another application of the Surface Equivalence Principle, which allows the asymmetric radiating conducting elements to be replaced with the equivalent currents, yielding a symmetric structure. The remainder of the now-symmetric geometry is analyzed by a body-of-revolution (BOR) FDTD algorithm [9]. Computational resource savings of greater than 97% are realized when compared to a full 3D volume discretization of the entire geometry. The resultant radiation pattern compares closely with actual test data.

The proposed method is also used to model the same reflector antenna system, but with an asymmetrical radome covering the main reflector system [10], [11]. The method is used to compute radiation patterns as a function of the tilt angle between the radome and the main reflector antenna system.

Improvements to the standard FDTD algorithm have been made to enhance modeling accuracy for patch antennas with curved edges [12], and codes have been developed to compute radiation patterns for the various geometries mentioned earlier [8]-[10].

1.2 Thesis Outline

Chapter 2 provides a background on the simulation techniques used in the proposed method, namely the FDTD and MoM techniques, along with a description of the geometries best suited for analysis by each method. Hybrid techniques previously used on structures similar to those described in this thesis are also discussed, including their advantages and disadvantages. Finally, the Surface Equivalence and Reciprocity Theorems are described, as they form the interface between the two numerical techniques in the proposed hybrid method.

Validation of the proposed method is illustrated in Chapter 3 by modeling narrow radiating slots mounted on an infinite-length conducting cylinder. A description of the proposed method – a Reciprocity Approach – to pattern computation is presented followed by radiation patterns for slots oriented in both the axial and azimuthal directions.

These plots are compared to patterns computed by analytical means and are shown to be in exact agreement. Finally, pattern computations for the same slots but mounted on finite-length conducting cylinders are shown, and convergence to the infinite-length case is demonstrated as the cylinders are increased in length.

Chapter 4 presents the analysis of an elliptical microstrip patch antenna contained within a dielectric cavity and mounted on an infinite-length conducting cylinder. The infinite length was chosen to allow comparison of the pattern to an alternate method. A description of the problem geometry is first presented, followed by a description of the Reciprocity Approach applied to this specific geometry. Electric field distributions produced by the patch antenna and plane wave-generated current distributions on the surface of the conducting cylinder are presented, as determined by the improved conformal FDTD algorithm and analytical formulas, respectively. Finally, the radiation pattern derived from the electric fields and surface currents is presented and compared to a pattern computed by an alternate method. They are shown to be in close agreement. A description of the alternate method is also included in this chapter.

Chapter 5 describes the analysis of a large reflector antenna system, which is circularly symmetric about the reflector’s axis of rotation except for the microstrip feed. The problem geometry is first defined, followed by a description of the application of the Surface Equivalence and Reciprocity Theorems to efficiently compute the radiation pattern. Next, the analysis of the microstrip patch feed antenna is presented, which includes the application of the Surface Equivalence Principle. This renders the original geometry circularly symmetric. The Body of Revolution (BOR) FDTD algorithm is then described, which exploits the symmetry created by the equivalence principle. A description of the Reciprocity approach to pattern computation for this specific case is then outlined, followed by the procedure used to compute both co-polarization and cross-polarization gain from the left-hand circularly polarized (LCP) reflector antenna system. Finally, the resultant pattern is compared to actual test data, and the two patterns are shown to be in good agreement.

Chapter 6 describes the analysis of the same reflector antenna system, except with an inhomogeneous radome covering the entire system. An “equivalent aperture” approach is developed to compute radiation patterns with respect to the tilt angle between the radome and the remainder of the reflector antenna system. A description of the aperture field construction procedure is presented followed by plots of aperture field distributions used in the analysis. Finally, radiation patterns as a function of the tilt angle between the radome and reflector antenna system are presented.

Chapter 7 presents a summary of the thesis research and suggestions for further improvements.

Chapter 2

GENERAL ANALYSIS METHODS

This chapter describes the general numerical methods used to model the problem geometries outlined in Chapter 1. The application of techniques specific to particular problem geometries is described in later chapters concerned with these geometries. The Finite Difference Time Domain (FDTD) and Method of Moments (MoM) techniques are described, followed by the Surface Equivalence and Reciprocity Theorems, which are all employed in the proposed method. The geometries best suited to each method are also discussed. Next, a survey of hybrid techniques previously used, which usually involve a combination of two simulation methods, is presented. Finally, the proposed method is described and a justification for the selection of the particular combination of techniques is provided.

2.1 FDTD Fundamentals

The Finite Difference Time Domain (FDTD) technique is one of the most popular means of analyzing transient and frequency-domain electromagnetic problems. Due to its formulation, it can be used to model combinations of several materials configured in arbitrary structures. In addition, because the results are in the time domain, they can be Fourier-transformed to the frequency domain, yielding information over a wide range of frequencies. Another advantage of this method is the absence of matrices, which are typically found in other techniques, thereby eliminating the need for extensive matrix inversion techniques.

The finite difference method was first suggested by Yee in 1966 [16], but was dismissed as an accurate but impractical numerical method due to the state of computational systems at that time. With the explosive growth of computational power, the method was reconsidered in the early 1990s, and has now become the most popular numerical technique for electromagnetic simulations.

Background information on the FDTD method, sufficient for an understanding of the proposed hybrid technique, is presented in this section. For additional information, references [5] and [17] can be consulted.

2.1.1 Difference Equations

The FDTD technique is based on Maxwell's curl equations (2.1), which describe the behavior of fields at all coordinates and at all times.

$$\begin{aligned} \nabla \times \mathbf{H} &= \mathbf{J} + \frac{\partial \mathbf{D}}{\partial t} \\ \nabla \times \mathbf{E} &= -\frac{\partial \mathbf{B}}{\partial t} \end{aligned} \qquad (\ 2.1\ )$$

where $\boldsymbol{D} = \varepsilon \boldsymbol{E}$ and $\boldsymbol{B} = \mu \boldsymbol{H}$. The terms $\boldsymbol{D}$ and $\boldsymbol{B}$ are the electric and magnetic flux densities, and $\boldsymbol{E}$ and $\boldsymbol{H}$ are the electric and magnetic fields, respectively. Material properties (permittivity and permeability denoted as ε and μ, respectively) in the above relations can be expressed as second-order tensors to accommodate the general case of anisotropic materials and can also be time-varying. However, for the time-varying case, a time convolution technique is required [20] within the conventional FDTD algorithm. The permittivity of a material can be expressed as

$$\varepsilon(r)=\begin{bmatrix}\varepsilon_{xx}(r) & \varepsilon_{xy}(r) & \varepsilon_{xz}(r)\\ \varepsilon_{yx}(r) & \varepsilon_{yy}(r) & \varepsilon_{yz}(r)\\ \varepsilon_{zx}(r) & \varepsilon_{zy}(r) & \varepsilon_{zz}(r)\end{bmatrix} \qquad (\ 2.2\ )$$

Likewise, the permeability μ of a material can be expressed in the same manner. For some materials, the off-diagonal components of (2.2) are zero (*i.e.*, $\varepsilon_{ij} = 0$ for $i \neq j$). For anisotropic materials in which this condition holds, the remaining nonzero diagonal elements are distinct, while for isotropic materials, all three elements are identical and the tensor can be expressed as a scalar. Only isotropic materials are considered in this thesis.

In the FDTD method, these relations are transformed into equivalent difference equations. The curl of the magnetic field ***H*** in Cartesian coordinates is expressed as follows:

$$\nabla\times\mathbf{H}=\hat{x}\left(\frac{\partial H_z}{\partial y}-\frac{\partial H_y}{\partial z}\right)+\hat{y}\left(\frac{\partial H_x}{\partial z}-\frac{\partial H_z}{\partial x}\right)+\hat{z}\left(\frac{\partial H_y}{\partial x}-\frac{\partial H_x}{\partial y}\right) \qquad (\ 2.3\ )$$

Derviatives in (2.3) are converted to difference equations as follows:

$$\frac{\partial H_z}{\partial y}\rightarrow\frac{H_z\left(x,y+\frac{\Delta y}{2},z;t\right)-H_z\left(x,y-\frac{\Delta y}{2},z;t\right)}{\Delta y} \qquad (\ 2.4\ )$$

The right hand side of (2.1) is expressed in difference equation form, in which the material is assumed isotropic, as follows:

$$\mathbf{J}(r,t)+\varepsilon(r)\frac{\partial}{\partial t}\mathbf{E}(r,t)\rightarrow\mathbf{J}(r,t)+\varepsilon(r)\frac{\mathbf{E}\left(r,t+\frac{\Delta t}{2}\right)-\mathbf{E}\left(r,t-\frac{\Delta t}{2}\right)}{\Delta t}$$
$$-\mu(r)\frac{\partial}{\partial t}\mathbf{H}(r,t)\rightarrow-\mu(r)\frac{\mathbf{H}\left(r,t+\frac{\Delta t}{2}\right)-\mathbf{H}\left(r,t-\frac{\Delta t}{2}\right)}{\Delta t} \qquad (\ 2.5\ )$$

The spatial derivatives contained in the curl of the magnetic field shown in equation (2.3) are approximated as in (2.4) for each component, while equation (2.5) shows the time derivatives in difference equation form. The curl of the electric field ***E*** in the second relation of (2.1) is also expanded in the manner shown for the ***H*** field in (2.3).

The difference equations shown in (2.5) are in the form known as central differences, as both the time and spatial derivatives are centered about the coordinates of interest (*i.e.*, the time and spatial derivatives are centered about time *t* and coordinates (*x, y, z)*, respectively). This numerical approximation of the derivative results in second order accuracy: a decrease in the discretization size Δ (time or space) by a factor *k* improves the accuracy of the calculation by the factor k^2 [18], [19]. The FDTD update equations for electric fields located within isotropic materials appear in (2.6)-(2.8).

$$E_x^{n+1}(i,j,k)=E_x^{n}(i,j,k)+\frac{1}{\tilde{\varepsilon}(i,j,k)}\left[\begin{array}{l}\dfrac{H_z^n\left(i,j+1/2,k\right)-H_z^n\left(i,j-1/2,k\right)}{\Delta y}\\ -\dfrac{H_y^n\left(i,j,k+1/2\right)-H_y^n\left(i,j,k-1/2\right)}{\Delta z}\\ -J_x^n(i,j,k)\\ \end{array}\right] \qquad (\ 2.6\ )$$

$$E_y^{n+1}(i,j,k) = E_y^n(i,j,k) + \frac{1}{\tilde{\varepsilon}(i,j,k)}\left[\begin{array}{l} \dfrac{H_x^n\left(i,j,k+\frac{1}{2}\right) - H_x^n\left(i,j,k-\frac{1}{2}\right)}{\Delta z} \\ -\dfrac{H_z^n\left(i+\frac{1}{2},j,k\right) - H_z^n\left(i-\frac{1}{2},j,k\right)}{\Delta x} \\ -J_y^n(i,j,k) \end{array}\right] \qquad (2.7)$$

$$E_z^{n+1}(i,j,k) = E_z^n(i,j,k) + \frac{1}{\tilde{\varepsilon}(i,j,k)}\left[\begin{array}{l} \dfrac{H_y^n\left(i+\frac{1}{2},j,k\right) - H_y^n\left(i-\frac{1}{2},j,k\right)}{\Delta x} \\ -\dfrac{H_x^n\left(i,j+\frac{1}{2},k\right) - H_x^n\left(i,j-\frac{1}{2},k\right)}{\Delta y} \\ -J_z^n(i,j,k) \end{array}\right] \qquad (2.8)$$

in which the subscripts and superscripts represent the polarization direction and time index, respectively. The term $\tilde{\varepsilon}(i,j,k)$ represents the permittivity averaged over the four cells surrounding the electric field of interest since ***E*** fields are defined on cell edges, while isotropic material properties are defined within cell volumes (see *Figure 2–1*).

$$H_x^{n+1}\left(i,j+\frac{1}{2},k+\frac{1}{2}\right) = H_x^n\left(i,j+\frac{1}{2},k+\frac{1}{2}\right) + \frac{1}{\mu\left(i,j+\frac{1}{2},k+\frac{1}{2}\right)} \times \left[\begin{array}{l} \dfrac{E_y^n(i,j,k+1) - E_y^n(i,j,k)}{\Delta z} \\ -\dfrac{E_z^n(i,j+1,k) - E_z^n(i,j,k)}{\Delta y} \end{array}\right] \qquad (2.9)$$

$$H_y^{n+1}\left(i+\tfrac{1}{2},j,k+\tfrac{1}{2}\right)=H_y^{n}\left(i+\tfrac{1}{2},j,k+\tfrac{1}{2}\right)+\frac{1}{\mu\left(i+\tfrac{1}{2},j,k+\tfrac{1}{2}\right)}\times\left[\begin{array}{l}\dfrac{E_z^n(i+1,j,k)-E_z^n(i,j,k)}{\Delta x}\\ -\dfrac{E_x^n(i,j,k+1)-E_x^n(i,j,k)}{\Delta z}\end{array}\right] \qquad (\ 2.10\ )$$

$$H_z^{n+1}\left(i+\tfrac{1}{2},j+\tfrac{1}{2},k\right)=H_z^{n}\left(i+\tfrac{1}{2},j+\tfrac{1}{2},k\right)+\frac{1}{\mu\left(i+\tfrac{1}{2},j+\tfrac{1}{2},k\right)}\times\left[\begin{array}{l}\dfrac{E_x^n(i,j+1,k)-E_x^n(i,j,k)}{\Delta y}\\ -\dfrac{E_y^n(i+1,j,k)-E_y^n(i,j,k)}{\Delta x}\end{array}\right] \qquad (\ 2.11\ )$$

The update equations for magnetic fields located within isotropic materials are presented in (2.9)-(2.11).

2.1.2 Yee Cell

In the conversion from differential to difference equations, both time and space are transformed from a continuum of infinitesimal point coordinates into discrete cells with finite dimensions. The convention adopted by FDTD researchers to define these discrete field locations and polarizations is known as the Yee cell (see *Figure 2–1*), named in honor of the researcher who devised this numerical technique [16]. Arrows with a circle at the base denote ***H*** fields, while all others represent ***E*** fields. Only a few representative fields have been labeled for the sake of clarity. The coordinate indexing scheme denotes cells in the *x*, *y*, and *z* directions as integer indices *i*, *j*, and *k*, respectively.

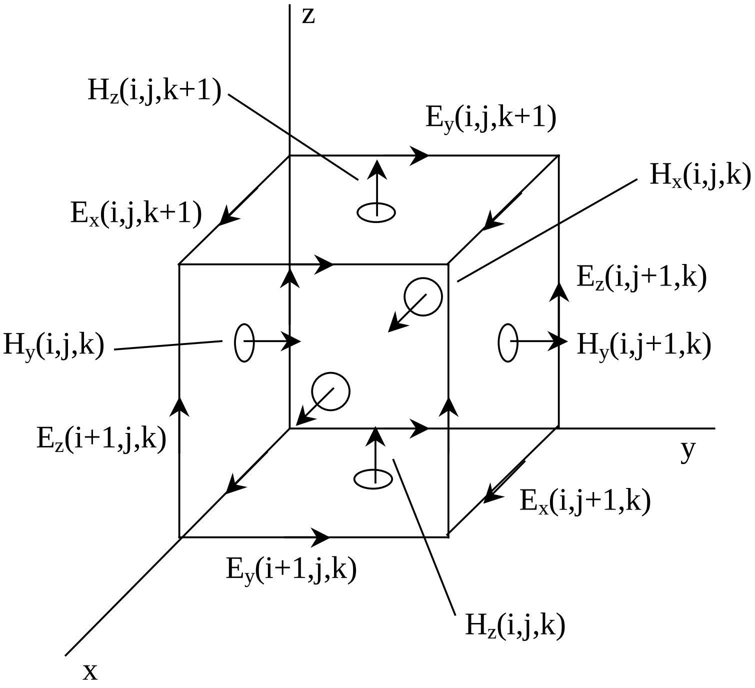

Figure 2–1: 3-D Yee Cell

The cell dimensions are Δx by Δy by Δz, which can vary as a function of x, y, and z to more closely conform to objects with curved edges or surfaces. For accurate simulations, cells with edges of length $\lambda_m/10$ or less is required with $\lambda_m/20$ as the recommended maximum size (λ_m is the wavelength of an isotropic material contained within the cell of interest). This discretization allows a sufficient number of field samples as a function of spatial distance, to yield an accurate representation of the actual field.

In addition, the time increment used for the simulation must be set below a maximum value to ensure numerical stability. The relation that must be satisfied is known as the Courant stability condition [21], [22], and is expressed as

$$\Delta t \leq \frac{1}{v\sqrt{\left(\frac{1}{\Delta x}\right)^2 + \left(\frac{1}{\Delta y}\right)^2 + \left(\frac{1}{\Delta z}\right)^2}} \qquad (2.12)$$

in which v is the minimum propagation velocity for all cells contained within the simulation volume. Thus, all materials in the model must be accounted for when determining the maximum time increment.

2.1.3 Absorbing Boundary Conditions (ABC)

For open boundary radiation problems in which a system is located within an infinite free-space (or dielectric) volume, the simulation model must include all effects on the fields due to the system, but exclude all fields produced by reflections from simulation domain boundaries. Due to limited computational resources, the simulation domain requires truncation, which may introduce spurious fields from the boundaries unless appropriate measures are taken. Recently, this issue has been the subject of extensive research efforts.

The first most widely used ABC was devised by Mur in 1981 [23]. This boundary condition is derived from a one-way wave equation, which allows only outgoing waves as possible solutions. However, the attenuation of waves incident on the Mur ABC degrades as the incident angle (away from the normal) increases until at the grazing angle, the boundary becomes perfectly reflecting.

In 1994, Berenger [24] derived a new boundary condition referred to as a Perfectly Matched Layer (PML) which reduces reflections several orders of magnitude below other techniques. It uses a modified set of Maxwell's equations in which fields at the ABC-simulation space interface are split into two components and an artificial anisotropic material is introduced within the ABC. The result is a PML wave impedance perfectly matched to the simulation space and independent of incident angle. Incident waves are attenuated in the direction normal to the layers as they propagate through the artificial medium. Reflection coefficients as low as –80 dB have been demonstrated [25] for both 2-D and 3-D FDTD simulations. These reflection coefficient figures represent a 40 dB improvement over the Mur and Liao [26] ABCs.

Although the PML technique provides an excellent boundary condition, its split field formulation requires a two-fold increase in computational memory and run-time in the regions containing the PML material relative to the conventional FDTD algorithm. To avoid this additional burden, a PML boundary condition based on a Maxwellian formulation has been derived [27] and shown to be equivalent in effectiveness to the Berenger PML ABC. This alternate algorithm has the advantages of enhanced computational efficiency within the PML regions and elimination of the need for FDTD update equations modified for the split field formulation. The FDTD simulations presented in this thesis are based on this new PML algorithm. The code uses six PML layers with a fourth order spatial variation (normal to the layers) of the conductivity, as suggested in [27].

To conduct a simulation, the problem geometry is first defined by assigning appropriate material values (as in equation 2.2) to all cells in the simulation domain. Next, all cell fields in the simulation domain are initialized to appropriate values: cells in regions containing sources are set to the excitation source values, while all others are set to a desired initial value (usually zero). The fields at subsequent time increments in all cells not containing sources are computed from the difference equations presented in (2.6)-(2.11). Thus, all fields in the simulation domain are updated at each time step by these difference equations, which include a source definition for cells located at source coordinates. Note that the time increment must also be selected below the maximum value defined in equation (2.12) to maintain numerical stability. Absorbing boundary conditions, preferably the PML technique, should be used at the truncation boundaries to obtain accurate results for open radiation problems.

2.1.4 Geometries Best Suited for FDTD Simulations

Due to the FDTD formulation (2.6)-(2.11), and the discrete Yee cells (*Figure 2–1*) used in the method, complicated structures composed of several materials configured in arbitrary patterns can be accurately modeled provided the cells are chosen to be sufficiently small. In addition, since field values at all points in the simulation domain are computed for all time steps, frequency domain information can be obtained through a discrete Fourier transform. This is an advantage over frequency-domain techniques, which require separate simulations for each frequency of interest.

Although geometries with complex material structures can be modeled by the FDTD method, the size of the simulation domain cannot be exceedingly large. Limited computational resources, in terms of both memory and run-time, impose this constraint. Objects with sharp edges or corners further limit the size of the simulation domain, as they require an increased number of cells. Thus, research efforts have been focused at either reducing the number of dimensions in the simulation [10] or developing methods to avoid the use of small cells in regions of curved edges or shapes [12]. These techniques have been utilized in this thesis for enhanced modeling efficiency, and will be discussed in Chapter 6 and the next section.

Due to its inherent strengths in modeling inhomogeneous geometries, the FDTD method is used to model the conformal antenna region of the problem geometry of Chapter 4 and the large reflector antenna system of Chapters 5 and 6.

2.1.5 Improved Conformal FDTD Algorithm

In the FDTD update equations for the magnetic field (2.9)-(2.11), the formulas require the electric fields at coordinates surrounding the position of the magnetic field of interest. This is in accordance with Ampere's Law (with Maxwell's correction) in integral form, which relates the magnetic field to the closed line integral of the electric field. However, if part of a given cell lies within a perfect electrically conducting (PEC) material, that portion of the electric field line integral does not contribute to the magnetic field, as the electric field vanishes at those coordinates. This situation is illustrated in *Figure 2–2*. For a 2-D FDTD grid, this figure displays the cell numbered (*n*, *m*) partially located within a PEC region (darker shaded area). The curved line defines the PEC-free space boundary, while the straight line joining the two intersection points between the cell and this curved line approximates the interface.

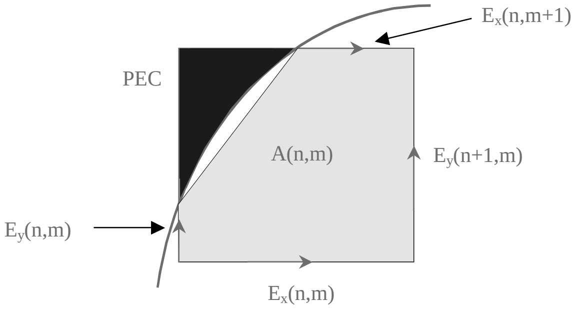

Figure 2–2: 2-D FDTD Cell Partially Located within PEC

Physically, the tangential electric field along the curved line vanishes. However, to simplify the simulation, the field is assumed to be zero along the straight line.

An example of how well a set of these straight intersection lines approximates a curved surface is shown in *Figure 2–3*.

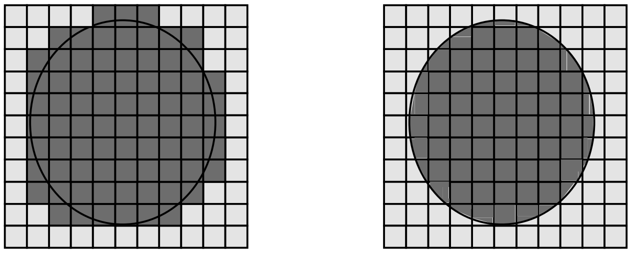

Figure 2–3: Staircased *vs.* Conformal Approximation to a Circular Disk

This figure shows a circular disk approximated by both the straight-line (conformal) approximation (right) and the traditional staircasing (left) methods. It is clear from this figure that the disk edge is approximated much more closely by the conformal method compared to the staircase method. This significantly improves the accuracy of the model, especially when edge effects are dominant.

For the staircasing procedure, the sharp corners introduced by this method produce high frequency artifacts, which further degrade the accuracy of the model. If the grid is made finer, the staircasing procedure conforms more closely to the curved edge, but at the cost of increased computational memory and run-time. In addition, high frequency errors are not reduced.

Previous algorithms based on the conformal technique described above have used the deformed area *A(n, m)* (*Figure 2–2*) in updating the magnetic field [28]; it appears that the magnetic field lines are restricted to this region. This causes stability problems as the area parameter appears in the denominator of the magnetic field update equation. In addition, for numerical stability according to the Courant condition [21], the time increment must also be adjusted. Since the cell size is decreased in the method described in [28], the corresponding time increment must also be reduced, thereby requiring an increased number of time steps to obtain solutions for the same time period.

These stability problems have recently been eliminated through the use of a new algorithm, which takes into account that static magnetic field lines are not restricted between PEC regions [12]-[15]. This new method uses the entire cell area, or volume in the 3-D case, in the updating of magnetic fields. The accuracy of the new technique has been verified against asymptotic methods whose results depend on the accurate modeling of curved edges, which contribute diffracted fields in shadow regions.

2.2 MoM Fundamentals

The Method of Moments (MoM) technique has been used since the 1960s as it is a more computationally efficient method compared to the FDTD algorithm for homogeneous objects. This is because the MoM method used in this thesis discretizes only the surface of objects as opposed to a volumetric cell discretization of the entire simulation domain as in the FDTD method. For this thesis, surface currents generated on arbitrarily-shaped conducting bodies by incident plane waves are needed for the pattern computation. In the MoM technique [29], the Electric Field Integral Equation (EFIE) is typically used to mathematically define the problem and is solved for the surface currents generated on the objects of interest. These currents can then be used in radiation integrals to calculate the fields scattered by the objects.

This section develops the EFIE and describes the MoM technique used to solve it in determining the surface currents generated on an arbitrarily-shaped conducting body by an incident plane wave. The Rao-Wilton-Glisson basis functions [30] are described, as these basis functions are utilized in the MoM code – developed by Michielssen [31] – used in this thesis. A code was written to convert edge currents, computed by the Michielssen code, to equivalent surface currents. The development of this code also required knowledge about the Rao-Wilton-Glisson basis functions. Finally, the surface current distribution produced on a square perfectly conducting plate is presented to illustrate an application of the method.

2.2.1 The Electric Field Integral Equation (EFIE)

The Electric Field Integral Equation (EFIE) is derived from the zero total tangential electric field condition on the surface of a perfectly conducting body *S*. Since the total electric field is composed of the incident and scattered fields ($\boldsymbol{E}^{inc}$ and $\boldsymbol{E}^{scat}$), the incident electric field on the conducting body surface can be expressed as

$$\mathbf{E}^{inc}\Big|_{r=r_s} = -\mathbf{E}^{scat}\Big|_{r=r_s} \qquad (\ 2.13\ )$$

where $r_s \in S$. The scattered electric field can be found by combining Faraday's Law (the first relation of 2.1 with $\boldsymbol{J}=\boldsymbol{0}$) and the following definition of the magnetic vector potential $\boldsymbol{A}$:

$$\mathbf{H} = \frac{1}{\mu}\nabla\times\mathbf{A} \qquad (\ 2.14\ )$$

After solving for the electric field in the first relation of (2.1) with $\boldsymbol{J}=\boldsymbol{0}$ and using the vector identity

$$\nabla\times\nabla\times\mathbf{A} = \nabla(\nabla\cdot\mathbf{A}) - \nabla^2\mathbf{A} \qquad (\ 2.15\ )$$

the scattered electric field can be expressed as

$$\mathbf{E}^{scat}(r) = \frac{1}{j\omega\mu\varepsilon}\left[\nabla(\nabla\cdot\mathbf{A}) - \nabla^2\mathbf{A}\right] \qquad (\ 2.16\ )$$

By combining equations (2.1a), (2.14), and (2.15), and using the Lorentz gauge as shown in [32], the vector wave equation for the magnetic vector potential $\boldsymbol{A}$ can be derived as

$$\nabla^2\mathbf{A} + k^2\mathbf{A} = -\mu\mathbf{J} \qquad (\ 2.17\ )$$

whose solution is

$$\mathbf{A}(r) = \mu \int_S \mathbf{J}(r') \frac{e^{-jkR}}{4\pi R} dV' \qquad (\ 2.18\ )$$

For surface currents, ***J***$_S$, the solution to (2.17) is:

$$\mathbf{A}(r) = \mu \int_S \mathbf{J}_S(r') \frac{e^{-jkR}}{4\pi R} d\mathbf{S}' \qquad (\ 2.19\ )$$

where *R*=|***r-r’***|. Also, ***r*** and ***r’*** represent the vectors from the origin to the observation point (*x, y, z*) and from the source coordinates (*x’*, *y’*, *z’*) to the observation point (*x, y, z*), respectively (see *Figure 2–4*).

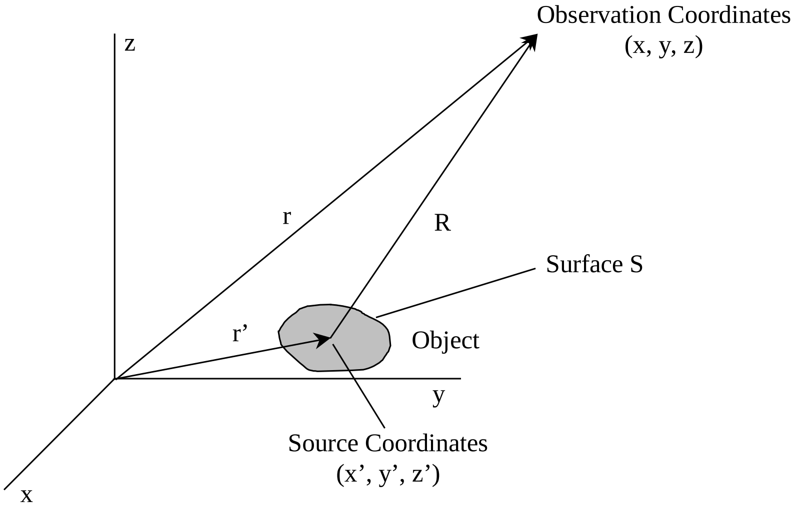

Figure 2–4: Source and Observation Coordinates

In addition, *S* is the surface of the conducting object and $\boldsymbol{J_s}$ is the current density on the surface *S*. Setting ***J=0*** in equation (2.17), (2.16) can be rewritten as

$$\mathbf{E}^{scat}(r) = \frac{1}{\mu}\frac{1}{jk}\left[\nabla\left(\nabla \cdot \mathbf{A} + k^2\mathbf{A}\right)\right] \tag{2.20}$$

Defining the free-space Green's function as

$$\mathbf{G}(r, r') = \frac{e^{-jk|r-r'|}}{4\pi|r-r'|} \tag{2.21}$$

substituting (2.19) into (2.20) and using (2.13), in which the observation point is restricted to the surface of the conducting object ($r=r_S$), yields

$$\mathbf{E}^{inc}(r)\Big|_{r=r_s} = j\frac{\eta}{k}\left[k^2\int_S \mathbf{J}_S(r')\mathbf{G}(r,r')d\mathbf{S}' + \nabla\int_S \nabla'\cdot\mathbf{J}_S(r')\mathbf{G}(r,r')d\mathbf{S}'\right]\Bigg|_{r=r_s} \tag{2.22}$$

where ∇ and ∇'· are the gradient with respect to the observation (*x, y, z*) coordinates and divergence with respect to the source (*x', y', z'*) coordinates, respectively. Equation (2.22) is referred to as the Electric Field Integral Equation (EFIE) as the integral on the right hand side is expressed in terms of the known incident electric field. In order to determine the unknown surface current density $\boldsymbol{J}_s$, a technique known as the moment method will be applied. This is described in the next section.

2.2.2 Moment Method

Equation (2.22) can be expressed in operator form as [33]

$$L[f(r')] = g(r') \tag{2.23}$$

where L is the linear integrodifferential operator appearing in equation (2.22):

$$L = j\frac{\eta}{k}\left[k^2\int_S d\mathbf{S}'\mathbf{G}(r,r') + \nabla\int_S d\mathbf{S}'\mathbf{G}(r,r')\nabla'\cdot\right]\Bigg|_{r=r_s} \quad (2.24)$$

where η and k are the intrinsic impedance and wave number of the medium, respectively. The function *f(r')* represents the unknown function {$\boldsymbol{J_S}(r')$ in equation (2.22)} and *g(r')* represents the known excitation vector (incident electric field), all in terms of the observation point on the surface of the object, *r'*. Solving this problem directly by taking the inverse of the operator (L^{-1}) is usually difficult, if not impossible. Instead, the solution may be found numerically by using the linearity of the *L* operator. This is done by first expanding *f(r')* in *N* terms of a selected basis function $f_n(r')$,

$$L\left[\sum_{n=1}^{N} a_n f_n(r')\right] = g(r') \quad (2.25)$$

Since *L* is a linear operator, it can be brought inside the summation as follows:

$$\sum_{n=1}^{N} a_n L[f_n(r')] = g(r') \quad (2.26)$$

In equation (2.26), the unknown to be determined is the set of expansion coefficients, a_n. In order to find them, an inner product is first defined as follows:

$$\langle f_1(r), f_2(r)\rangle = \int_S f_1(r) f_2(r) dS \quad (2.27)$$

in which *S* is the surface of the geometry under analysis, and a set of *N* weighting functions are selected. Taking the inner product of these weighting functions with both sides of equation (2.26) yields,

$$\left\langle w_m(r'), \sum_{n=1}^{N} a_n L[f_n(r')] \right\rangle = \langle w_m(r'), g(r') \rangle$$
$$\sum_{n=1}^{N} a_n \langle w_m(r'), L[f_n(r')] \rangle = \langle w_m(r'), g(r') \rangle, \ \ m = 1,2,\ldots N \tag{2.28}$$

In the MoM code used for this thesis, the Galerkin method was used in which the weighting functions are chosen to be the same as the basis functions. Thus, (2.28) becomes,

$$\sum_{n=1}^{N} a_n \langle f_m(r'), L[f_n(r')] \rangle = \langle f_m(r'), g(r') \rangle \ \ m = 1\ldots N \tag{2.29}$$

Equation (2.29) can be expressed in matrices as in,

$$\begin{pmatrix} \langle f_1, L(f_1) \rangle & \langle f_1, L(f_2) \rangle & \cdots & \langle f_1, L(f_N) \rangle \\ \langle f_2, L(f_1) \rangle & \langle f_2, L(f_2) \rangle & \cdots & \langle f_2, L(f_N) \rangle \\ \vdots & \vdots & \ddots & \vdots \\ \langle f_N, L(f_1) \rangle & \langle f_N, L(f_2) \rangle & \cdots & \langle f_N, L(f_N) \rangle \end{pmatrix} \begin{pmatrix} a_1 \\ a_2 \\ \vdots \\ a_N \end{pmatrix} = \begin{pmatrix} \langle f_1, g \rangle \\ \langle f_2, g \rangle \\ \vdots \\ \langle f_N, g \rangle \end{pmatrix} \tag{2.30}$$

which can be expressed concisely in matrix form as:

$$[L_{mn}][a_n] = [g_m] \tag{2.31}$$

where $[L_{mn}]$, $[a_n]$, and $[g_m]$ are $N\times N$, $N\times 1$, and $N\times 1$ matrices (or vectors), respectively. The unknown vector $[a_n]$ can then be found by solving equation (2.31).

2.2.3 Rao-Wilton-Glisson Basis Functions

To solve the above relation, the vector basis functions defined by Rao, Wilton, and Glisson in [30] are used. The surface current density $\boldsymbol{J_S}$ appearing in equation (2.22) is expanded along these basis functions as follows

$$\mathbf{J}_S(r)=\sum_{n=1}^{N} I_n \mathbf{f}_n^{RWG}(r) \qquad (2.32)$$

The expansion coefficients I_n of (2.32), referred to as edge currents, are defined for each nonboundary edge of the discretized surface (*i.e.*, triangular patch edges that lie on the surface of interest). These edge currents can be interpreted to be the normal component of the current flowing through the n^{th} edge. This will be described in more detail below. For boundary edges, the edge currents are zero.

The Rao-Wilton-Glisson vector basis functions are defined for a pair of triangular patches about an edge as shown below

$$\mathbf{f}_n^{RWG}(r)=\begin{cases} \dfrac{l_n}{2A_n^+}\boldsymbol{\rho}_n^+(r) & for \quad r\in T_n^+ \\ \dfrac{l_n}{2A_n^-}\boldsymbol{\rho}_n^-(r) & for \quad r\in T_n^- \\ 0 & otherwise \end{cases} \qquad (2.33)$$

in which $\boldsymbol{\rho}_n^{\pm}(r)$ and $A_n^{\pm}$ for edge l_n are defined for two different points (r_1 and r_2) within triangles T_n^+ and T_n^- in *Figure 2–5*, in which the $\boldsymbol{\rho}_n^+(r)$ and $\boldsymbol{\rho}_n^-(r)$ vectors point away and toward the free vertex, and A_n^+ and A_n^- represent the areas of triangles T_n^+ and T_n^-, respectively. The $T_n^{\pm}$ triangles are usually defined by a mesh generator program.

Properties of the vector basis functions include current flow only along boundary edges (no perpendicular component), continuous normal current component across all nonboundary edges, and constant charge density within each triangular patch. The first property can be described by referring to *Figure 2–6*.

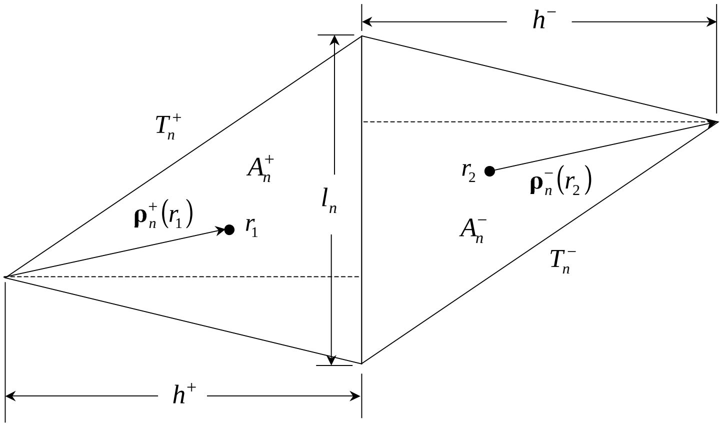

Figure 2–5: T_n^+ and T_n^- Triangular Patch Definitions, n^{th} edge

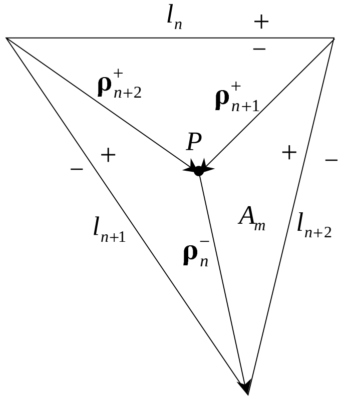

Figure 2–6: Surface Current Calculation at Point *P* Inside Patch *m*

The diagram in *Figure 2–6* shows an example vector configuration for the surface current at a point *P* within patch *m* with a particular $T_n^{\pm}$ configuration (denoted by the "+" and "– " signs around each edge). Note that the adjacent triangular patches have been omitted. The patch being considered is assumed to be completely interior (no boundary edges) to the discretized surface. The surface current at the point P is the sum of the three edge current I_n - basis function $\mathbf{f}_n^{RWG}(r)$ products for the three edges (l_n, l_{n+1}, and l_{n+2}) surrounding this patch. Note that the $\boldsymbol{\rho}_n^{\pm}(r)$ vectors, along with the length to area ratio in equation (2.33), define the direction of the current. To show how these basis functions allow only current flow along boundary edges, suppose edge l_{n+1} is now a boundary edge (thus, $I_{n+1} = 0$) and the point P is located on edge l_{n+1}. Because I_{n+1} is zero, $\boldsymbol{\rho}_{n+1}^{+}(r)$ has no effect on the resultant current. Thus, current can only flow along edge l_{n+1} as the vectors $\boldsymbol{\rho}_n^{-}(r)$ and $\boldsymbol{\rho}_{n+2}^{+}(r)$ are directed along the edge. The resultant direction depends on the relative magnitudes of I_n and I_{n+2} and the length of the two edges l_n and l_{n+2}.

Continuity of the normal component of the current across nonboundary edges is enforced by the vector basis functions through the factor appearing before $\boldsymbol{\rho}_n^{\pm}(r)$ in equation (2.33). At a point on edge l_n of *Figure 2–5*, the normal component of either $\boldsymbol{\rho}_n^{+}(r)$ or $\boldsymbol{\rho}_n^{-}(r)$ is the height $h_n^{\pm}$ of triangle T_n^{+} or T_n^{-}, respectively. Noting that the areas $A_n^{\pm}$ of triangles $T_n^{\pm}$ are $0.5\,h_n^{\pm}\,l_n$, the heights and therefore the normal components of the vectors $\boldsymbol{\rho}_n^{\pm}(r)$ are $\frac{2A_n^{\pm}}{l_n}$. Multiplied by the factors appearing in equation (2.33), this component of the current becomes equal to the n^{th} edge current I_n in (2.32). Therefore, the normal component of the current through all nonboundary edges is continuous. Also, as stated above, edge currents I_n are equivalent to the normal component of the current flowing through the n^{th} edge. Note that there exists a current component along edge l_n for all $\boldsymbol{\rho}_n^{\pm}(r)$ which are not perpendicular to the edge.

Constant charge density in all triangular patches is maintained by the divergence of the vector basis functions being constant within all triangular patches [34]. The divergence is proportional to the surface charge density through the continuity equation

$$\nabla \cdot \mathbf{J}_S = -j\omega\rho_S \qquad (2.34)$$

Taking the divergence of equation (2.32) is equivalent to taking the divergence of the basis functions on all triangular patches defined on the discretized surface. Considering one patch and assuming that the free vertex is the origin, the divergence for the patch is taken in the cylindrical coordinate system. Thus, for each edge l_n,

$$\nabla \cdot \vec{f}_n^{\,RWG} = \frac{1}{\rho_n^{\pm}} \frac{\partial}{\partial \rho_n^{\pm}} \left[\rho_n^{\pm} \left(\vec{f}_n^{\,RWG} \right)_{\rho_n^{\pm}} \right] = \frac{1}{\rho_n^{\pm}} \frac{\partial}{\partial \rho_n^{\pm}} \left(\rho_n^{\pm} \frac{l_n}{2A_n^{\pm}} \rho_n^{\pm} \right) = \pm \frac{l_n}{A_n^{\pm}} \qquad (2.35)$$

where $\rho_n^{\pm}$ is the length of vector $\boldsymbol{\rho}_n^{\pm}$. Therefore, the surface charge density is constant within each patch and, in addition, the total charge in each triangle pair is zero, as the charge within each triangle of each pair is equal and opposite in polarity.

2.2.4 Geometries Best Suited for MoM Simulations

Because the MoM technique used for this thesis discretizes the surface of a given object by triangular elements, it is well suited to the analysis of arbitrarily-shaped structures. The surface discretization represents substantial savings in memory requirements over the volume cells used in the FDTD method. In addition, triangular elements conform more closely to irregular surfaces than rectangular prisms do to irregularly shaped objects. However, the arrangement of the material regions comprising the object of interest is limited to relatively simple structures as the Green’s function (in equation 2.22) for complicated arrangements of material regions is difficult to derive. Also, for large objects, enhanced matrix inversion techniques must be applied in order to achieve reasonable computer run-times.

To address the material region arrangement issue, an MoM code developed by Michielssen [31] was used to simulate arbitrarily-shaped objects composed entirely of perfectly conducting material. Since it is also desired to analyze relatively large structures, the MoM code was modified to include optimized matrix inversion subroutines on the IBM RS/6000 machine used to perform the simulations [35], [36]. The latter set of subroutines (ESSL) [36] reduced the computer run-time on a problem with 7,774 unknowns from 70.0 hours to 1.8 hours.

Due to its inherent strengths in modeling large homogeneous – composed of one type of material – objects and enhanced computational capabilities afforded by the ESSL subroutines, the MoM technique was used to model the mounting structure of the problem geometry of Chapter 4 and the microstrip feed antenna of Chapters 5 and 6.

2.2.5 Example MoM Surface Current Distribution

The MoM code developed by Michielssen [31], enhanced by ESSL subroutines [36], and the edge to surface current conversion code were used to compute surface currents generated on a 1 wavelength square perfect electrically conducting (PEC) plate in the *xy*-plane illuminated by a normally incident, *x*-polarized plane wave. The surface was divided into 20 by 20 squares each containing two triangular MoM elements. The observation grid – used by the current conversion code – was chosen to be finer (101 by 101 points) in order to display the MoM element structure.

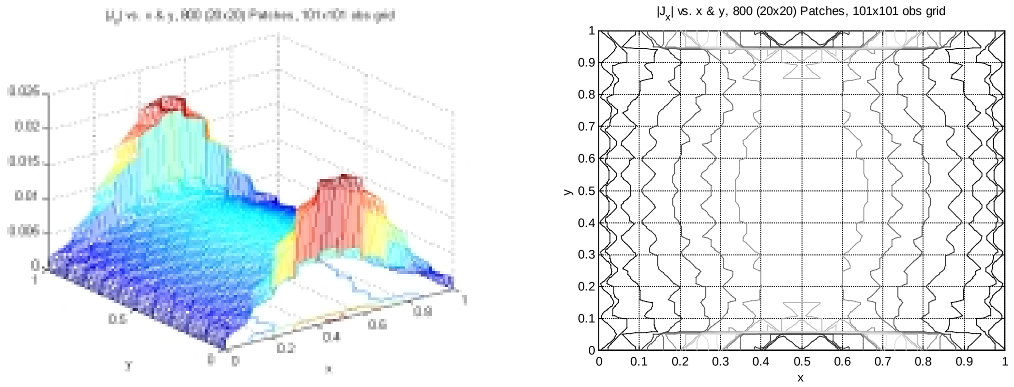

Figure 2–7: 1λ x 1λ Square PEC Plate Illuminated by E_x Plane Wave

Mesh and Contour Plots

Figure 2–7 shows a 3D mesh and 2D contour plot of the current distribution on the plate, while *Figure 2–8* shows *x* and *y* cuts through the center of the plate. Since the incident plane wave is *x*-polarized, J_x at *x=0* and *x=L* must be zero, as current cannot flow perpendicular to the edge. However, since the *y=0* and *y=L* edges are parallel to the polarization direction, currents can flow along these edges. These two conditions can be observed in *Figure 2–7* at the y = 0 and y = 1λ coordinates for all *x*. Also, the continuous normal current component property of the vector basis functions described in Sec. 2.2.3 can be observed in both the mesh and contour plots of *Figure 2–7* in that no contour lines appear in the *y* direction. Only diagonal and horizontal contour lines (triangular element edges) are present as they are not perpendicular to the direction of current flow (*x*).

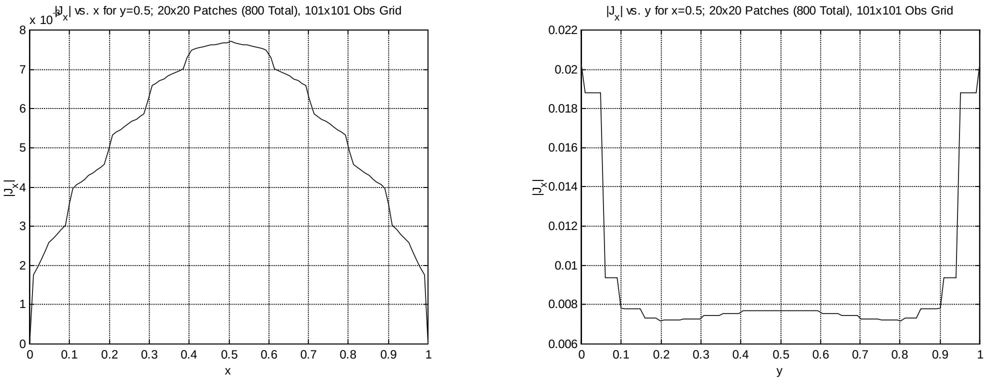
|J_x| vs. x for y=0.5; 20x20 Patches (800 Total), 101x101 Obs Grid

|J_x| vs. y for x=0.5; 20x20 Patches (800 Total), 101x101 Obs Grid

Figure 2–8: 1λ x 1λ Square PEC Plate Illuminated by E_x Plane Wave, x & y Cuts

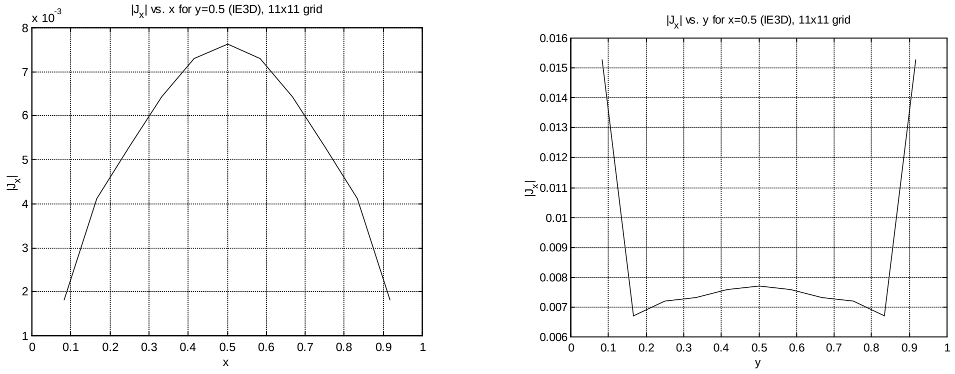
|J_x| vs. x for y=0.5 (IE3D), 11x11 grid

|J_x| vs. y for x=0.5 (IE3D), 11x11 grid

Figure 2–9: 1λ x 1λ Square PEC Plate Illuminated by E_x Plane Wave, x & y Cuts (IE3D)

The general shape of the current distribution agrees with the results presented in [34] and also compares closely with simulation results from the commercial code IE3D [37], shown in *Figure 2–9*.

2.3 Surface Equivalence Principle

The Surface Equivalence Principle allows the replacement of sources inside a closed volume with equivalent currents flowing on the surface of the closed volume. It is based on Huygens' principle which states that "each point on a primary wavefront can be considered to be a new source of a secondary spherical wave" [33], [38]. The more rigorous formulation of this principle was defined by Schelkunoff in 1936 [39]. This principle is based on the existence of currents at field discontinuities, which can be derived from the application of Stokes' theorem to Maxwell's curl equations,

$$\begin{aligned} \nabla \times \mathbf{H} &= \mathbf{J} + \frac{\partial \mathbf{D}}{\partial t} \\ \nabla \times \mathbf{E} &= -\mathbf{M} - \frac{\partial \mathbf{B}}{\partial t} \end{aligned} \qquad (2.36)$$

which yields,

$$\begin{aligned} \oint_L \mathbf{H} \cdot d\mathbf{l} &= \int_S \mathbf{J} \cdot d\mathbf{S} + \frac{\partial}{\partial t} \int_S \mathbf{D} \cdot d\mathbf{S} \\ \oint_L \mathbf{E} \cdot d\mathbf{l} &= -\int_S \mathbf{M} \cdot d\mathbf{S} - \frac{\partial}{\partial t} \int_S \mathbf{B} \cdot d\mathbf{S} \end{aligned} \qquad (2.37)$$

in which $\boldsymbol{J}$ and $\boldsymbol{M}$ are the volume electric and magnetic current densities, respectively. Applying equation (2.37) at an interface between two materials and taking the limit as $\Delta \to 0$ yields (see *Figure 2–10*),

$$\begin{aligned} \mathbf{J}_S &= \hat{n} \times (\mathbf{H}_2 - \mathbf{H}_1) \\ \mathbf{M}_S &= -\hat{n} \times (\mathbf{E}_2 - \mathbf{E}_1) \end{aligned} \qquad (2.38)$$

in which $\boldsymbol{J}_S$ and $\boldsymbol{M}_S$ are the surface electric and magnetic current densities, respectively.

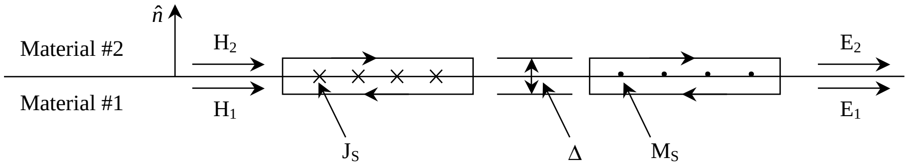

Figure 2–10: Currents at Field Discontinuities

To derive the Surface Equivalence Principle, consider *Figure 2–11*:

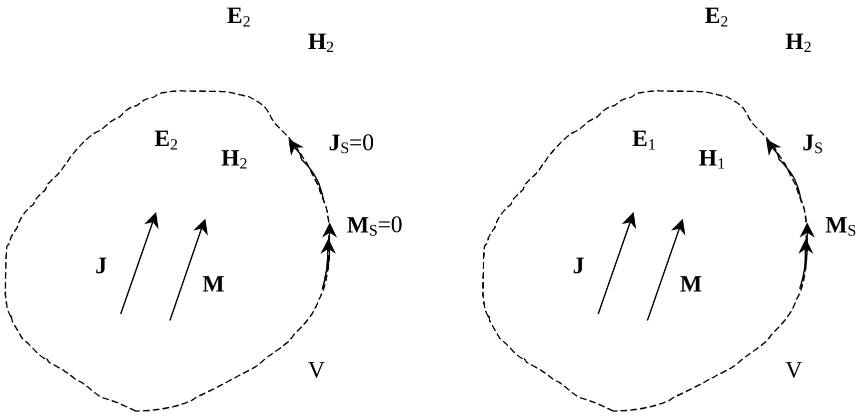

Figure 2–11: Surface Equivalence Principle

In the left hand diagram of *Figure 2–11*, two sources $\boldsymbol{J}$ and $\boldsymbol{M}$ contained in a volume V (artificial boundary) are radiating in a free space environment. Since the fields are continuous at the interface ($\boldsymbol{E}_2$ and $\boldsymbol{H}_2$ exist both inside and outside the volume) defined by V, equation (2.38) requires the currents on the surface of V to be zero as denoted in the figure. However, if the fields inside volume V are chosen to be different functions of spatial coordinates ($\boldsymbol{E}_1$ and $\boldsymbol{H}_1$) as shown in the right hand side of *Figure 2–11*, a discontinuity in the fields is created at the interface defined by *V*. Thus, equivalent surface magnetic and/or electric currents must flow on the surface of *V* to account for discontinuities in the electric and/or magnetic fields, respectively.

The fields internal to volume *V* ($\boldsymbol{E}_1$ and $\boldsymbol{H}_1$) can be set to any arbitrary value since the equivalent currents account for any discontinuity. If they are set to zero, the equivalent currents become

$$\begin{aligned} \mathbf{J}_S &= \hat{n}\times\left(\mathbf{H}_2-\mathbf{H}_1\right)\Big|_{\mathbf{H}_1=0} = \hat{n}\times\mathbf{H}_2 \\ \mathbf{M}_S &= -\hat{n}\times\left(\mathbf{E}_2-\mathbf{E}_1\right)\Big|_{\mathbf{E}_1=0} = -\hat{n}\times\mathbf{E}_2 \end{aligned} \qquad (2.39)$$

This is known as Love’s Equivalence Principle [40]. The relations in (2.39) state that the equivalent surface current densities are found from the fields radiated by the sources in free space at the surface of volume *V*. Setting the fields within volume *V* to zero allows the introduction of any material within the volume; zero-valued fields cannot be altered by the presence of any material.

For the geometry of Chapter 4, a perfect electrical conductor is selected for the material placed inside the volume. This shorts out any $\boldsymbol{J}_S$ created on the surface, resulting in the existence of only $\boldsymbol{M}_S$. For the configurations of Chapters 5 and 6, the Surface Equivalence Principle is used to replace the microstrip patch antennas by the electric currents flowing on them, as the discontinuity in the fields required by equation (2.39) is created by the fields resulting from the solution of (2.19), (2.14), and the bottom relation of (2.1).

2.4 Reciprocity Theorem

The Reciprocity Theorem relates the currents and fields of two systems. It is derived from Maxwell's curl equations written for two systems,

$$\begin{aligned}
\nabla\times\mathbf{E}_1 &= -\mathbf{M}_1 - j\omega\mu\mathbf{H}_1\\
\nabla\times\mathbf{H}_1 &= \mathbf{J}_1 + j\omega\varepsilon\mathbf{E}_1\\
\nabla\times\mathbf{E}_2 &= -\mathbf{M}_2 - j\omega\mu\mathbf{H}_2\\
\nabla\times\mathbf{H}_2 &= \mathbf{J}_2 + j\omega\varepsilon\mathbf{E}_2
\end{aligned} \qquad (2.40)$$

Note that the subscripts in (2.40) represent the system number (1 or 2) and not inside or outside the volume *V* as shown in *Figure 2–11*. Through mathematical manipulations, the application of a vector identity, and the Divergence Theorem, as shown in [32], the following relation results,

$$\int_{V_2}\left(\mathbf{E}_1\cdot\mathbf{J}_2-\mathbf{H}_1\cdot\mathbf{M}_2\right)dV=\int_{V_1}\left(\mathbf{E}_2\cdot\mathbf{J}_1-\mathbf{H}_2\cdot\mathbf{M}_1\right)dV \qquad (2.41)$$

in which V_1 and V_2 represent the volumes containing sources $\boldsymbol{J_1}/\boldsymbol{M_1}$ and $\boldsymbol{J_2}/\boldsymbol{M_2}$, respectively The above relation is applied in two ways to the problem geometries presented in later chapters. In all cases, the integral on the left side of (2.41) will simplify to a simple vector product between the desired far-zone electric field $\boldsymbol{E_1}$ and an assumed point dipole source $\boldsymbol{J_2}$ since the point source exists at only one point in space It is assumed that the source is composed of only electric current; thus, $\boldsymbol{M_2}$ is zero.

The right hand side of (2.41) will depend on the geometry being analyzed, but the volume integral will always simplify to one taken over the surface of the radiating aperture. For the geometry of Chapter 3, the aperture is a slot, while for Chapter 4, it is the superstrate located above the radiating patch antenna cavity. For both Chapters 5 and 6, the aperture is the feed antenna for the reflector antenna system. Specific applications of the Reciprocity Theorem are described in subsequent chapters.

2.5 Hybrid Techniques

Two or more modeling techniques can be combined to take advantage of the strengths of each method, while at the same time overcoming each technique's weaknesses. The overall hybrid method thus becomes more effective than the use of the individual techniques applied separately. This section will describe hybrid methods previously used by researchers, followed by a justification for the selection of techniques used in the proposed hybrid method.

2.5.1 Previously Used Hybrid Techniques

Researchers have used a combination of the Finite Element Method (FEM) and MoM techniques to analyze cavity-backed patch antennas [41] and an interior region composed of an inhomogeneous medium with an arbitrarily-shaped dielectric in the exterior region [42]. This hybrid technique employs the MoM method in regions where the Green's function is known (outside of the cavity containing the patch antenna) and the FEM technique to the cavity region, which is inhomogeneously filled and not amenable to an application of the hybrid approach. The overall approach was verified in [41] through FDTD simulations in two dimensions [42], the volume integral/moment method solution [43], and the unimoment solution [44], [45]. The last aforementioned method incorporates the radiation condition (that the fields tend to zero as the distance from the scatterer tends to infinity) into either the finite difference or finite element method with less computer storage and run time requirements.

The FEM/MoM hybrid technique has also been applied to inhomogeneous bodies of revolution [46]. The use of both the Electric Field Integral Equation (EFIE) and the Magnetic Field Integral Equation (MFIE) to enforce the Sommerfeld radiation condition, yields a symmetric system matrix. This allows the use of more computationally efficient matrix solvers.

The Edge-Element Method / MoM (EEM/MoM) hybrid technique has been applied to dielectric bodies of arbitrary shape in two dimensions (*i.e.*, cylinders of arbitrary shape), but of constant shape in the third (*z*) dimension [47]. In the EEM technique, Maxwell’s equations are discretized using an edge element expansion. The edge element technique has the advantages of eliminating spurious modes often introduced by the FEM method [47] and transforming Maxwell’s equations into an equivalent circuit, which creates a frequency independent formulation. The latter advantage enhances computational efficiency when analyses are required at several frequencies.

The FEM technique has also been combined with the Boundary Integral method for the simulation of cavity-backed patch antennas [49]-[51]. In this hybrid (FE-BI) method, the elements of the FEM matrix are defined by boundary integrals which describe the geometry of the system. The FEM matrix is used to compute the amplitudes of the electric field expansion coefficients that are combined with selected basis functions to yield the electric field. The boundary integrals describe such structures as conducting patches, impedance loads, and coaxial feeds. This set of papers also uses the BiConjugate Gradient (BiCG) method to avoid generating and storing the FEM matrix, thereby enhancing computational efficiency. In [49], only rectangular patches are modeled.

Arbitrarily shaped cavity-backed patch antennas were modeled also using the FE-BI method [50]. In this paper, the cavity is discretized into tetrahedral volume elements, which can conform to any patch shape. The BiCG method, along with the Fast Fourier Transform (FFT), is used to reduce matrix generation and storage requirements.

Cavity-backed patch antennas mounted on a cylinder were also modeled using the FE-BI hybrid method [51]. The introduction of a cylinder creates a Green’s function that is an infinite series, which requires excessive computational resources. The paper thus uses an asymptotic formula for large-radii cylinders to yield a more reasonably dimensioned Green’s function. The BiCG method is again used in conjunction with the FFT to solve for the scattered fields.

Another set of hybrid techniques includes the combination of FEM with the high-frequency methods of the Uniform Theory of Diffraction (UTD), Physical Optics (PO), and Shooting and Bouncing Rays (SBR) [52]. These methods were used to predict radiation patterns for antennas mounted on aircraft structures. The FEM code was used to first compute the antenna’s radiation pattern in the absence of the aircraft. The high-frequency methods then used the resultant pattern (converted into equivalent currents) as sources to radiate the propagating fields in the presence of the aircraft to produce the overall pattern.

The codes using UTD matched measured data more closely than did the codes using PO and SBR, especially in the shadow regions of the antenna.

Hybrid techniques combining the MoM technique with high-frequency techniques such as the Geometrical Theory of Diffraction (GTD) have also been used to predict scattering properties [53]. The hybrid MoM-GTD method extends the capabilities of MoM and has been used to model small details on larger structures.

Another hybrid approach used to reduce computational resource requirements is the hybrid Physical Optics (PO) and MoM technique [54]. This approach allows the modeling of objects at higher frequencies where the MoM method alone would require excessive computer storage and run-time. A reduction in the size of the MoM matrix is accomplished by using PO basis functions in conjunction with the MoM basis functions. These two sets of basis functions overlap, which allows for a continuous current flow over the surface of the scattering object.

The FDTD technique has also been combined with high-frequency techniques such as Physical Optics (PO) [55], to model cavities with complex terminations, such as that found in jet aircraft engines. In this approach, the FDTD method is used to model the complex termination region (jet engine fan blades), while the high-frequency approach is used to model the cavity that includes the region up to the termination (jet engine inlet region). Verification is done by examination of the individual methods for accuracy prior to hybrid simulations. The fan blades were approximated in the FDTD analysis by the staircased meshing method. Improvements to this procedure could be obtained by using the conformal method described in [12].

The FDTD technique has been combined with a time-domain version of MoM to effectively model simple antennas radiating in the presence of complex inhomogeneous dielectric bodies [56]. The time-domain MoM technique is referred to as “marching on in time.” The MoM method is used to compute the radiating fields from the antenna at the position of a closed surface. The surface equivalence theorem is used to transform these fields into equivalent currents. Subsequently, the FDTD method is used to propagate these equivalent currents onto and into the complex dielectric object.

2.5.2 Proposed Method

The FDTD and MoM techniques combined through both the Surface Equivalence and Reciprocity Theorems have been applied to all of the problem geometries analyzed in this thesis. For the cavity-backed patch antenna and reflector antenna problem geometries analyzed in Chapters 4 through 6, the FDTD method has been selected over alternate techniques such as FEM or MoM due to greater computational efficiency and suitability to the problem geometry. With respect to the FEM technique, FDTD does not require matrix inversion to calculate the fields at various points in space, nor does it require a re-meshing of the problem geometry for different frequencies. Since the FDTD method computes time-domain information, this information can be Fourier-transformed to the frequency domain at any frequency within the bandwidth of the excitation signal. In addition, more effective absorbing boundary conditions [24], [27] are presently available for the FDTD method as compared to those available for the FEM.

With respect to the MoM technique, the FDTD method is better suited for solving problem geometries that contain inhomogeneous bodies, as it does not require knowledge of the Green’s function for the computation of currents or fields. Therefore, the FDTD method appears to be an optimal choice for the simulation of these particular geometries.

For the mounting structure used in the conformal antenna geometry of Chapters 3 and 4, the MoM technique has been used. For this structure, the Surface Equivalence Principle (Sec. 2.3) is applied – PEC is substituted into the volume – reducing the complexity of the material structure arrangement to one composed entirely of perfectly conducting material. This structure is well-suited for analysis by the MoM technique used in this thesis as only the object’s surface is discretized – as opposed to the volume discretization procedure used for FDTD simulations – and only the free-space Green’s function is required. The advantages of a decreased number of required elements and the closer approximation of the surface by 2D triangular – as compared to 3D rectangular - elements are realized by applying the MoM technique.

For the feed antenna of Chapters 5 and 6, a commercial MoM code – Ensemble [57] – was used to determine the currents flowing on the radiating patches of the antenna. The code analyzes conducting patches mounted on a stratified structure: stacked infinite planes of dielectric and conducting material. Since the feed antenna is finite in extent, this model represents an approximation to the actual configuration. The accuracy of the overall method has been verified against actual test data [9], which suggests that the approximation introduces negligible errors into the calculation. Thus, the MoM procedure appears to be the best choice for analysis of this particular geometry.

The Reciprocity Approach offers improved efficiency over asymptotic methods by using stored surface fields determined by the FDTD method and the impedance matrix describing the problem geometry for the MoM portion of the overall code. The stored fields and matrix elements are used in conjunction with an excitation vector (input into the MoM algorithm), which varies the incidence angle to produce the radiation pattern. This is significantly more efficient than computing ray-tracings for each coordinate in the radiation pattern as is required for the asymptotic methods. The Reciprocity Approach requires a re-simulation of a small portion – modifications to the excitation vector – of the overall procedure as opposed to the complete re-simulation required in the asymptotic method for each radiation pattern coordinate.

The Reciprocity Approach also offers greater computational efficiency compared to using FDTD alone, which would require an excessive number of simulation cells to accurately compute the fields. The proposed approach is also better suited to the problem geometry when compared to the MoM technique used alone. The problem geometry contains inhomogeneous bodies, which cannot be easily solved by MoM due to the unavailability of Green’s functions at many locations within the problem geometry. Therefore, the proposed hybrid approach is ideal for analysis of the aforementioned problem geometries.

Chapter 3

RADIATION PATTERNS FROM SLOTS MOUNTED ON CYLINDRICAL STRUCTURES

This chapter validates the Reciprocity Approach described earlier in this thesis as an accurate method for pattern computation. The canonical problem of a radiating slot mounted on an infinite length perfectly conducting cylinder is used for this purpose. The chapter begins with a description of the problem geometry and the Reciprocity Approach to pattern computation. Next, slots oriented in two directions: axial (along the cylinder axis) and azimuthal (along the circumference of the cylinder) are analyzed and the resultant patterns are compared to analytical calculations. Finally, the same slots mounted on finite length conducting cylinders are analyzed and the resulting patterns are also compared to analytical results.

The Reciprocity Approach allows the modeling of finite length cylinders, in addition to ideal infinite cylinders, which is an important tool for the simulation of actual systems. It is shown that cylinder length has a strong effect on radiation patterns, especially for lengths that are an odd versus an even number of wavelengths. Also, convergence of the finite length cylinder patterns as a function of increasing length to the infinite-length case is demonstrated.

3.1 Problem Geometry

Radiation patterns produced by narrow radiating slots oriented in both the axial and azimuthal directions have been computed. These slots are mounted on infinite-length conducting cylinders of radius $0.2\lambda_o$. This particular radius was selected based on memory constraints for the analysis of finite-length cylinders considered later in this chapter. However, it is noted that the proposed technique is applicable to structures of any size. A diagram of the slot configurations appears in *Figure 3–1*:

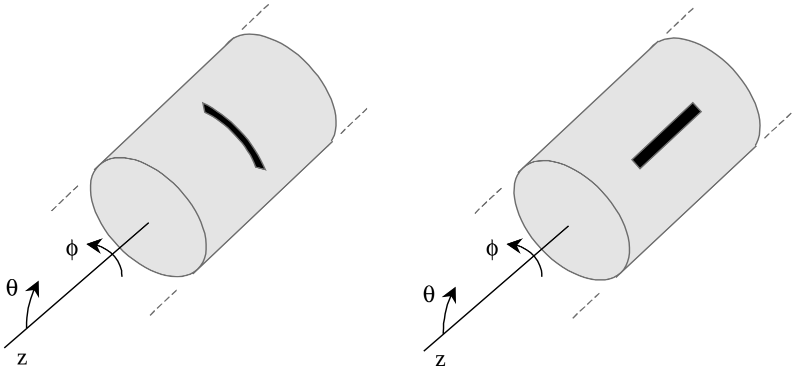

Figure 3–1: Narrow Azimuthal and Axial Radiating Slots on Infinite Length Conducting Cylinders

Since it is assumed that the aperture field along the width of both slots is uniform, a small slot width is required ($<0.1\lambda_o$). The angle subtended in the ϕ direction by the azimuthal slot, was chosen to be 24.8^o to match the example analyzed in [7]. The length of the axial slot can be short; the field distribution along the z direction can be either cosinusoidal or uniform. It can also span the entire length of the cylinder. The radiation pattern, as a function of ϕ ($\theta = 90^o$), for this orientation is taken at the center of the slot.

For both orientations, the narrow slots are assumed to be excited by a rectangular waveguide operating in the dominant TE mode – the electric fields vary cosinusoidally along the length of the slot (half-period) and are uniform across the width. The polarization is directed across the width of the slot.

3.2 Reciprocity Method for Pattern Computation

To compute the pattern produced by a slot mounted on a conducting cylinder, the Surface Equivalence and Reciprocity Theorems are applied. The fields in the slot – referred to as the aperture fields – are first converted to magnetic currents by the Surface Equivalence Principle described in Sec. 2.3. The slot is then replaced with conducting material, yielding a homogeneous cylinder with magnetic currents flowing at the position of the slot. To compute the radiation pattern, the problem is analyzed in two modes of operation: transmitting and receiving.

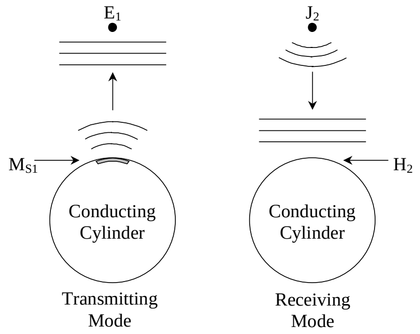

Figure 3–2: Reciprocity Approach for Radiating Slot Pattern Computation

In the transmitting mode, the surface magnetic currents $\boldsymbol{M}_{S1}$ radiate from the slot coordinates on the conducting cylinder to a far-zone coordinate. It is desired to compute the electric field $\boldsymbol{E}_1$ at the far-zone coordinate. The cylindrical waves emitted by the slot become plane waves in the far-zone as shown in *Figure 3–2*.

Instead of computing the far-zone field directly, the operation of the antenna is reversed to the receiving mode. In this mode, an infinitesimal dipole source $\boldsymbol{J}_2$, oriented in the direction of the desired polarization, is placed at the exact location where the far-zone field is desired. Note that the spherical waves emitted by the dipole source also become plane waves due to the location of the source in the far-zone of the cylinder. The source is specified as an electric current source; thus, $\boldsymbol{M}_2$ in equation (2.34) and (3.1) below is zero. The Reciprocity relation is repeated here for convenience.

$$\int_{V_2} \left(\mathbf{E}_1 \cdot \mathbf{J}_2 - \mathbf{H}_1 \cdot \mathbf{M}_2\right) dV = \int_{V_1} \left(\mathbf{E}_2 \cdot \mathbf{J}_1 - \mathbf{H}_2 \cdot \mathbf{M}_1\right) dV \qquad (\ 3.1\ )$$

where V_1 and V_2 are the volumes containing the source currents $\boldsymbol{J}_1/\boldsymbol{M}_1$ and $\boldsymbol{J}_2/\boldsymbol{M}_2$, respectively. The electric fields tangential to the surface of the conducting cylinder, including the location where the slot has been replaced by a perfect conductor – via the Surface Equivalence Principle – are zero. Therefore, $\boldsymbol{E}_2$ in the above equation also vanishes. The only remaining undefined term is $\boldsymbol{H}_2$. This can be derived from the electric currents generated on the cylinder by the incident plane waves produced by the far-zone dipole source $\boldsymbol{J}_2$. Through the simplifications stated above, the Reciprocity relation for this particular configuration becomes

$$\int_{V_2} \mathbf{E}_1 \cdot \mathbf{J}_2 \, dV = -\int_{V_1} \mathbf{H}_2 \cdot \mathbf{M}_1 \, dV \qquad (\ 3.2\ )$$

The dipole source can be expressed as

$$\mathbf{J}_2 = Il\delta^3(r_o)\hat{u} \tag{3.3}$$

where *I*, *l*, and $\hat{u}$ represent the amplitude, length, and unit vector in the direction of the dipole source, respectively. The term $\delta^3(r_o)$ represents the 3-D Dirac delta function. The coordinate r_o is the position of the desired far-zone electric field. Since the dipole source exists at only one point in space – at the exact position of the desired far-zone field – the left side of (3.2) simplifies to a vector product of $\boldsymbol{E_1}$ and $\hat{u}$. In the receive mode, the equivalent magnetic fields exist at all points on the cylinder; however, the equivalent surface magnetic current density exists only at the position of the slot. Therefore, the right side of (3.2) simplifies to an integral taken over the surface area of the slot. The far-zone field $\boldsymbol{E_1}$ is thus proportional to this quantity.

To compute the radiation pattern, it is noted that the right side of (3.2) can be expressed as

$$\begin{aligned} -\int_V \mathbf{H}_2 \cdot \mathbf{M}_1 dV &= -\int_S \mathbf{H}_2 \cdot \mathbf{M}_{S1} dS \\ &= -\int_S \mathbf{E}_{1(slot)} \cdot \mathbf{J}_{S_{2(cyl)}}\, dS \end{aligned} \tag{3.4}$$

where *S* is the surface area containing the slot, and $\boldsymbol{E}_{1(slot)}$ and $\boldsymbol{J}_{S2(cyl)}$ are the slot aperture fields and surface currents generated on the cylinder by a plane wave of appropriate polarization, respectively. This identity is proven in Appendix A. Therefore, conversion to equivalent currents is not necessary for the pattern computation:

$$\mathbf{E}_1 \cdot \hat{u} = \frac{1}{Il}\int_S \mathbf{E}_{1(slot)} \cdot \mathbf{J}_{S_{2(cyl)}} dS \tag{3.5}$$

If the polarization of the desired electric field $\boldsymbol{E_1}$ and the source dipole are parallel, the above relation becomes

$$\left|\mathbf{E}_1\right| = \frac{1}{Il}\int_S \mathbf{E}_{1(slot)} \cdot \mathbf{J}_{S_{2(cyl)}} dS \qquad (\ 3.6\ )$$

3.3 Infinite-Length Cylinder

Slots mounted on infinite-length perfectly conducting cylinders are analyzed in this section. Both axially and azimuthally oriented slots are considered. Each case is described in the following subsections, which include the assumed aperture fields, analytically derived currents generated by normally incident plane waves polarized in the appropriate direction, and a comparison of the patterns produced by the Reciprocity Approach versus those computed by the analytical relations shown in [7].

The aperture fields in the slot, which are converted to $\boldsymbol{M_{S1}}$, are assumed to be cosinusoidal along the length and uniform across the narrow width.

3.3.1 Azimuthal Slot

The azimuthal slot considered subtends an angle of 24.8^{o} in the ϕ-direction. Due to the orientation of the slot (see *Figure 3–1)* the E_θ *vs.* ϕ pattern is computed for $\theta = 90^{o}$. This requires knowledge of the currents generated by a *z*-polarized plane wave normally incident on the infinite length cylinder [7]:

$$J_z = -\frac{2E_o}{\omega\mu\pi a}\sum_{n=-\infty}^{\infty}\frac{j^n e^{jn\phi}}{H_n^{(2)}(ka)} \qquad (3.7)$$

where $H_n^{(2)}$ is the cylindrical Hankel function of the second kind of order n, E_o is the amplitude of the incident plane wave, and a is the radius of the cylinder. Equation (3.7) defines the surface current density generated on the cylinder by a z-polarized plane wave traveling in the $-x$ direction. For the selected radius of $0.2\lambda_o$, the current distribution as a function of ϕ for all z is shown in *Figure 3–3*.

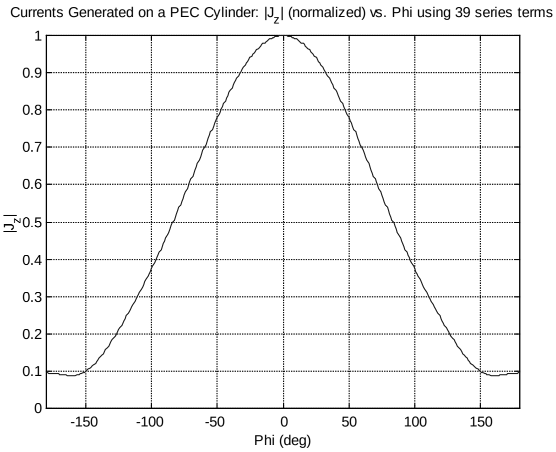

Figure 3–3: J_z *vs*. ϕ Produced by E_z Plane Wave on $r = 0.2\lambda_o$ Infinite Length Cylinder

The aperture field [7] is assumed cosinusoidal as described by the following equation

$$E_z = \frac{V}{W}\cos\left(\frac{\pi\phi}{\alpha}\right)\begin{cases} -\frac{W}{2} < z < \frac{W}{2} \\ -\frac{\alpha}{2} < \phi < \frac{\alpha}{2} \end{cases} \qquad (3.8)$$

where α, W, and V are the angle subtended (radians) by and width of the slot (meters), and the amplitude of the applied field (Volts), respectively.

To compute the $\phi = 0^{o}$ point in the pattern, the dot product between each sample point in the cosinusoidally distributed aperture field in the slot and the current distribution between the angular coordinates -12.4^{o} and $+12.4^{o}$ is taken and summed together. Other ϕ-points in the pattern are found by centering the angular range about the ϕ-point of interest. In effect, the above current distribution is sequentially rotated to produce the pattern. The resultant pattern is then normalized to its maximum value. The relatively high values (10% of the peak value) at the shadow side of the cylinder ($\phi = 0^{o}$) contributes to a back lobe, as shown in *Figure 3–4*:

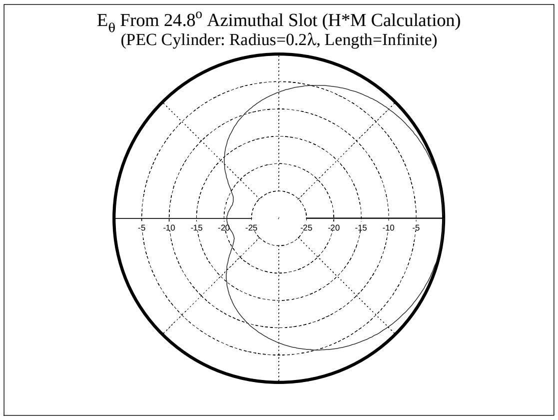

Figure 3–4: E_θ *vs*. ϕ Pattern for Azimuthal Slot (Reciprocity Method)

This pattern may also be computed analytically, as the mounting cylinder is infinite in length. For the E_θ pattern, the far-zone value is [7]

$$\lim_{r\to\infty} E_\theta = \lim_{r\to\infty} j\omega\mu \frac{e^{-jkr}}{\pi r}\sin\theta \sum_{n=-\infty}^{\infty} e^{jn\phi} j^{n+1} f_n(-k\cos\theta) \qquad (3.9)$$

where the function f_n is given by

$$f_n(\xi) = \frac{j\omega\varepsilon \overline{E}_z(n,\xi)}{\left(k^2-\xi^2\right) H_n^{(2)}\left(a\sqrt{k^2-\xi^2}\right)} \qquad (3.10)$$

in which a is the radius of the cylinder, $H_n^{(2)}$ is the cylindrical Hankel function of the second kind of order n and $\overline{E}_z$ is defined by a spatial Fourier transform of the aperture field E_z:

$$\overline{E}_z(n,\xi) = \frac{1}{2\pi}\int_0^{2\pi}\int_{-\infty}^{\infty} E_z(a,\phi,z) e^{-jn\phi} e^{-j\xi z}\, dz\, d\phi \qquad (3.11)$$

Substituting E_z as defined in equation (3.8) into (3.11) above results in:

$$\overline{E}_z(n,\xi) = \frac{V\alpha}{\pi^2-(n\alpha)^2}\cos\left(\frac{n\alpha}{2}\right)\frac{\sin\left(\frac{\xi W}{2}\right)}{\frac{\xi W}{2}} \qquad (3.12)$$

Substituting equation (3.12) into (3.10) and the resulting relation into (3.9) yields the radiation pattern shown in *Figure 3–5*. The two methods of pattern computation for the azimuthal slot produce identical results. This serves to validate the Reciprocity Approach as an accurate means for pattern computation for this slot configuration. The axially oriented slot will now be investigated.

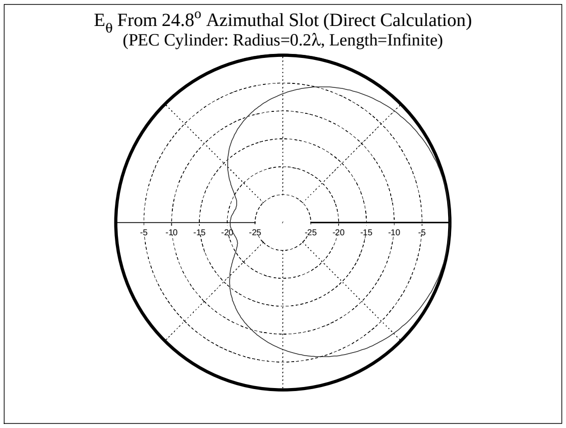

Figure 3–5: E_θ *vs*. ϕ Pattern for Azimuthal Slot (Direct Method)

3.3.2 Axial Slot

The axial slot is assumed to have a cosinusoidally varying aperture field along its length (z direction of cylinder) and a uniform field along its width (ϕ direction). The polarization is across the width, which corresponds to the ϕ direction for the cylinder. Thus, the currents generated on an infinite length cylinder by a normally incident ϕ-polarized plane wave are needed for the Reciprocity calculation. These are given by [7]

$$J_\phi = j\frac{2H_o}{\pi ka}\sum_{n=-\infty}^{\infty}\frac{j^n e^{-jn\phi}}{H_n^{(2)\prime}(ka)} \qquad (\ 3.13\ )$$

where H_o is the amplitude of the incident magnetic field plane wave and is related to the electric field amplitude by $H_o = E_o/\eta$. The prime in the above relation denotes the derivative taken with respect to the entire argument. The surface current density distribution as a function of ϕ for all z at the selected radius of 0.2 λ_o is shown in *Figure 3–6* below:

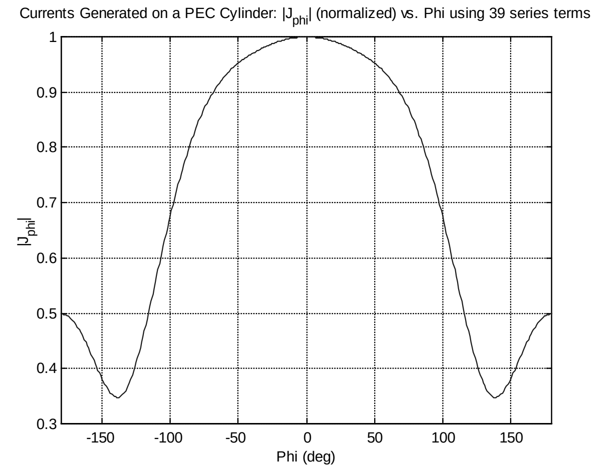

Figure 3–6: J_ϕ *vs*. ϕ Produced by E_ϕ Plane Wave on Cylinder with $r = 0.2\lambda_o$ and Infinite Length

The aperture field is assumed to be cosinusoidal along the length of the slot as defined in the following equation

$$E_\phi = \frac{V}{\alpha a}\cos\left(\frac{\pi z}{L}\right)\begin{cases} -\frac{L}{2} < z < \frac{L}{2} \\ -\frac{\alpha}{2} < \phi < \frac{\alpha}{2} \end{cases} \tag{3.14}$$

where L and V are the length of the slot (meters) and amplitude (Volts) of the aperture electric field, respectively. In this case, the slot length is sufficiently long to allow for the cosinusoidal distribution of the field, but in general can be as long as the length of the cylinder. The pattern is computed for all ϕ at $\theta = 90^o$: the xy-plane (z = 0) is defined at the center of the slot.

For this slot orientation, the only ϕ-dependent term on the right side of equation (3.5) is the current J_ϕ (the E_ϕ aperture field is uniform in the ϕ direction). It is not necessary to evaluate the integral since the pattern is normalized to the maximum field value. Hence, the relative pattern can be plotted directly from J_ϕ. The resulting pattern is shown below:

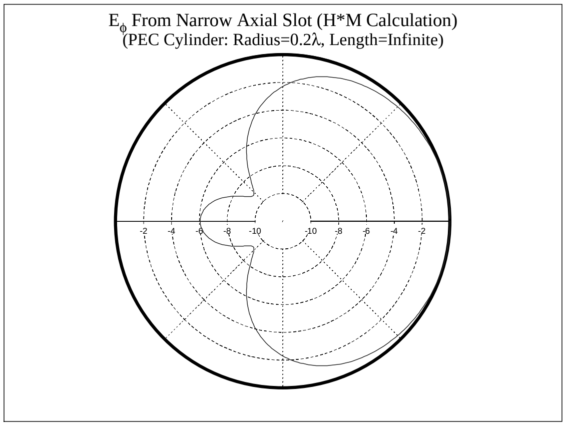

Figure 3–7: E_ϕ *vs*. ϕ Pattern for Axial Slot (Reciprocity Method)

As for the azimuthal slot, the pattern for the axial slot can be computed by analytical methods. This is done through the equation

$$\lim_{r\to\infty} E_\phi = -jk \lim_{r\to\infty} \frac{e^{-jkr}}{\pi r} \sin\theta \sum_{n=-\infty}^{\infty} e^{jn\phi} j^{n+1} g_n(-k\cos\theta) \qquad (3.15)$$

where the function g_n is defined as

$$g_n(\xi) = \frac{1}{\sqrt{k^2-\xi^2}\, H_n^{(2)\prime}\left(a\sqrt{k^2-\xi^2}\right)} \left[\overline{E}_\phi(n,\xi) + \frac{n\xi}{a\left(k^2-\xi^2\right)} \overline{E}_z(n,\xi) \right] \qquad (3.16)$$

in which $\overline{E}_\phi$ is defined in the same manner as $\overline{E}_z$ is in (3.11)

$$\overline{E}_\phi(n,\xi)=\frac{1}{2\pi}\int_0^{2\pi}\int_{-\infty}^{\infty}E_\phi(a,\phi,z)e^{-jn\phi}e^{-j\xi z}dz\,d\phi \qquad (\ 3.17\ )$$

Since the slot aperture field E_ϕ (defined from $-\alpha/2$ to $+\alpha/2$) is constant in the ϕ-direction, the ϕ integration in (3.17) produces a sinc function. However, this term is independent of ϕ and thus has no effect on the pattern. In addition, the pattern of interest is in the azimuthal plane; thus, $\theta = 90^{o}$. This renders all terms in (3.16) constant except the complex exponential $e^{jn\phi}$ and the derivative of the cylindrical Hankel function $H_n^{(2)\prime}$, which carries an n-dependence. Therefore, the far-zone E_ϕ field is computed from

$$\lim_{r\to\infty}E_\phi=-jk\lim_{r\to\infty}\frac{e^{-jkr}}{\pi r}A\sum_{n=-\infty}^{\infty}\frac{e^{jn\phi}j^{n+1}}{H_n^{(2)\prime}(ka)} \qquad (\ 3.18\ )$$

where the constant A represents the combination of all terms which are constant with respect to ϕ for this slot orientation and radiation pattern specifications. Using (3.18), the E_ϕ pattern is computed and shown in *Figure 3–8*. The plot is identical to the pattern computed by the Reciprocity Method shown in *Figure 3–7*. Therefore, the Reciprocity Approach for pattern computation has been validated for slots oriented in both directions. The next section will explore patterns produced by these same slots, but mounted on finite length conducting cylinders.

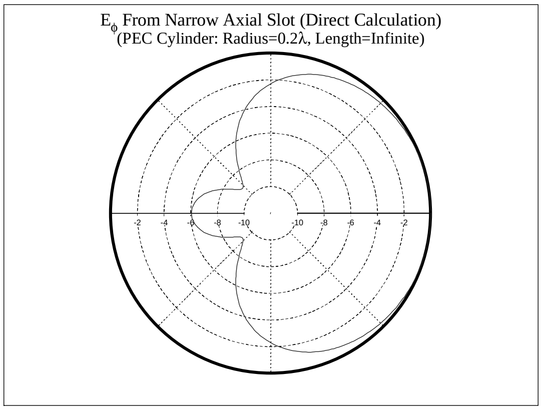

Figure 3–8: E_ϕ *vs*. ϕ Pattern for Axial Slot (Direct Method)

3.4 Finite-Length Cylinder

This section describes patterns produced by the same slots as discussed in the previous section, but mounted on finite-length conducting cylinders. The same slot aperture fields are used in these calculations; however, to compute the currents generated on finite length cylinders, a numerical technique is required. An MoM code [31] in conjunction with an edge to surface current conversion program is used to obtain the required surface currents. The following subsections present the generated surface currents, the resultant radiation patterns, and a comparison to the infinite-length cylinder patterns.

3.4.1 Azimuthal Slot

The azimuthal slot analyzed in this subsection has the same angular displacement and aperture field distribution as the slot described in Sec. 3.3.1 above. The plane wave generated surface currents, however, are computed using a numerical technique (MoM), as the length of the mounting cylinder is now finite. For the azimuthal slot orientation, the surface currents generated by a $\theta = 90^o$ (normal) incident *z*-polarized plane wave are required. An example distribution, for a 5λ long open-ended cylinder composed of perfect electrically conducting (PEC) material, is shown in *Figure 3–9*:

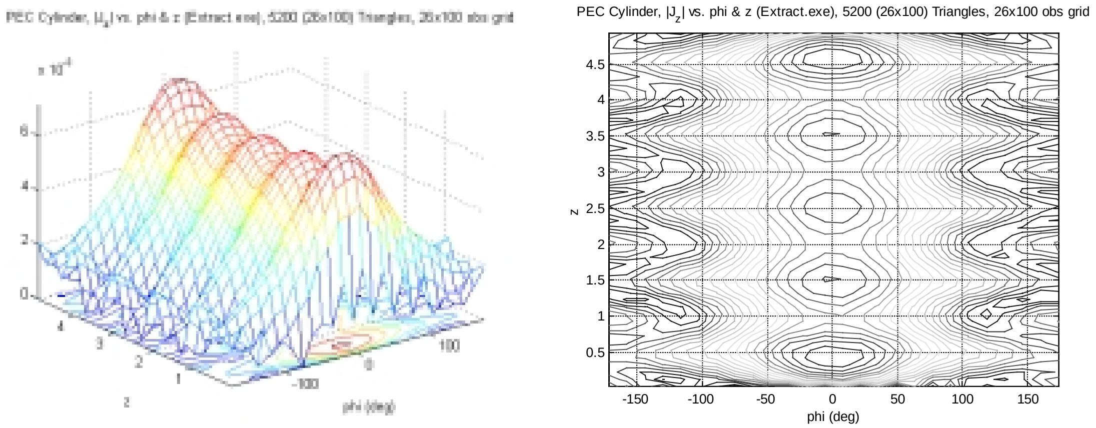

Figure 3–9: J_z Produced by E_z Plane Wave Incident on 5λ Long PEC Cylinder

The left and right sides of *Figure 3–9* are 3D mesh and 2D contour plots, respectively, of the J_z current distribution as a function of ϕ and z. Due to the truncation of the cylinder and the polarization of the incident plane wave being in the same direction (z), standing waves are formed with five magnitude peaks along the length of the cylinder. In constructing the patterns for the azimuthal slots, the location of the slots was chosen to be at the *z*-midpoint of the cylinder. This has a significant effect on the pattern as a function of the length of the cylinder.

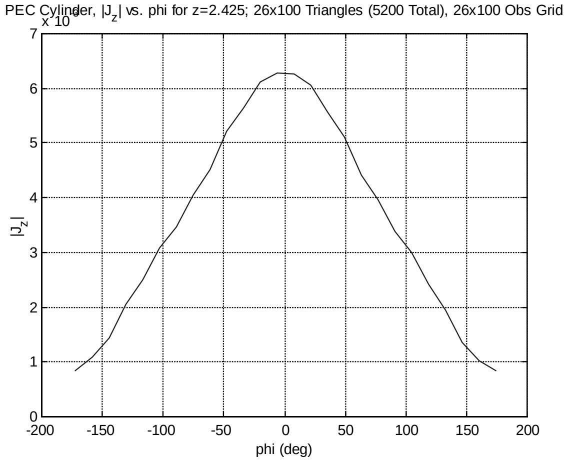

Figure 3–10: J_z *vs*. ϕ @ z-midpoint plane on 5λ PEC Cylinder

For an odd number of wavelengths (see *Figure 3–9* above), the slot intersects the current distribution at a peak on the lit side ($\phi = 0^o$) and a valley on the shadow side ($\phi = 180^o$).

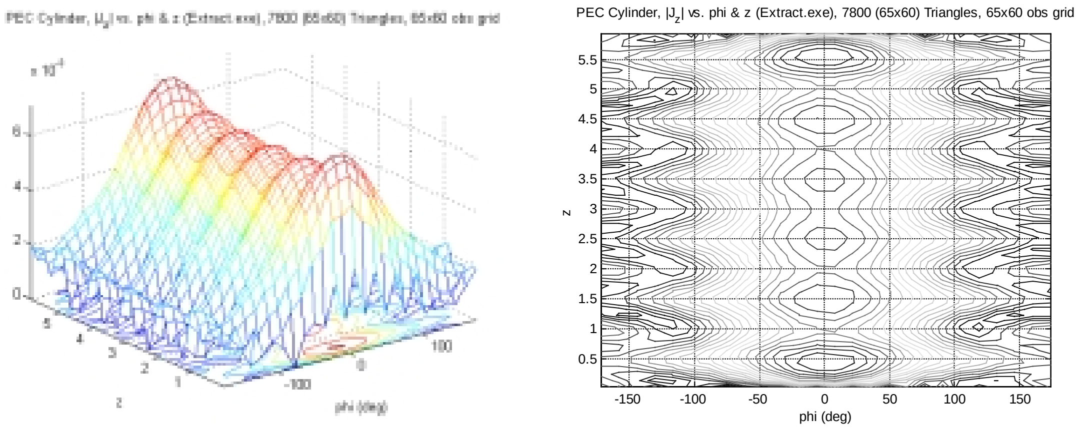

Figure 3–11: J_z Produced by E_z Plane Wave Incident on 6λ Long PEC Cylinder

This can be seen more clearly in the ϕ-cut plot at the z-midpoint plane of the cylinder, shown in *Figure 3–10*. For an even number of wavelengths, see *Figure 3–11*.

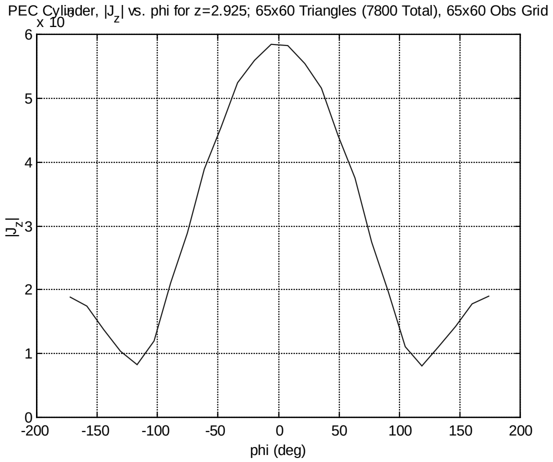

Figure 3–12: J_z *vs*. ϕ @ z-midpoint plane on 6λ PEC Cylinder

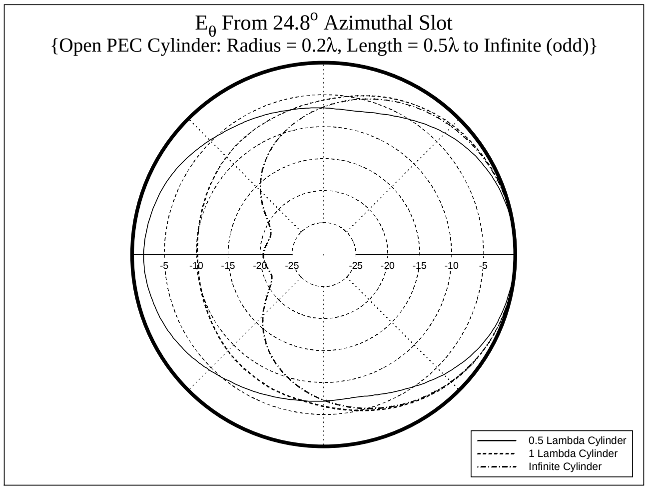

Figure 3–13: E_θ From 24.8^o Azimuthal Slot on Odd Wavelength Long PEC Cylinder {0.5λ to Infinite Length}

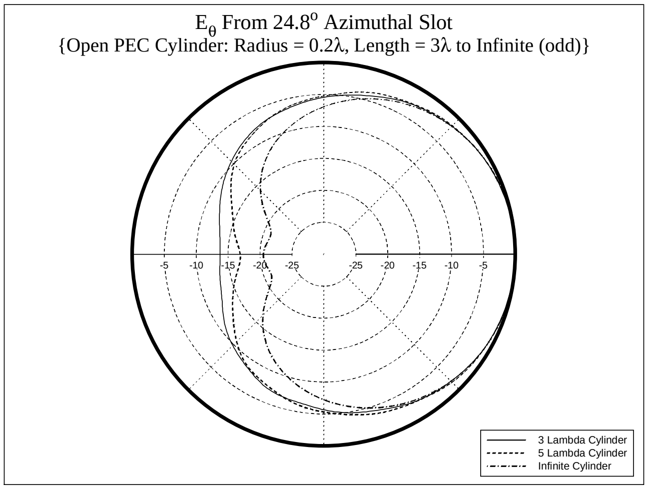

Figure 3–14: E_θ From 24.8^o Azimuthal Slot on Odd Wavelength Long PEC Cylinder{3λ to Infinite Length}

The slot intersects a “pass” – a lower magnitude peak between two higher peaks – of the current distribution on the lit side (ϕ = 0^o), while on the shadow side, it passes through a smaller peak. A ϕ-cut of the surface current at the *z*-midpoint plane of the cylinder, is shown in *Figure 3–12*. The small *z*-midpoint peak at $\phi = \underline{+}180^o$ creates a larger back lobe when the cylinder length is an even number of wavelengths as compared to the odd case.

Resultant patterns for the odd wavelength case are shown in two parts. *Figure 3–13* presents the patterns for the 0.5λ, 1λ, and infinite length cases, while *Figure 3–14* shows the 3λ, 5λ, and infinite length cases. The trend of the patterns is toward the infinite length case. All patterns, except the 0.5λ case, have a significantly lower magnitude on the shadow side due to the valley in the current distribution (see *Figure 3–9*).

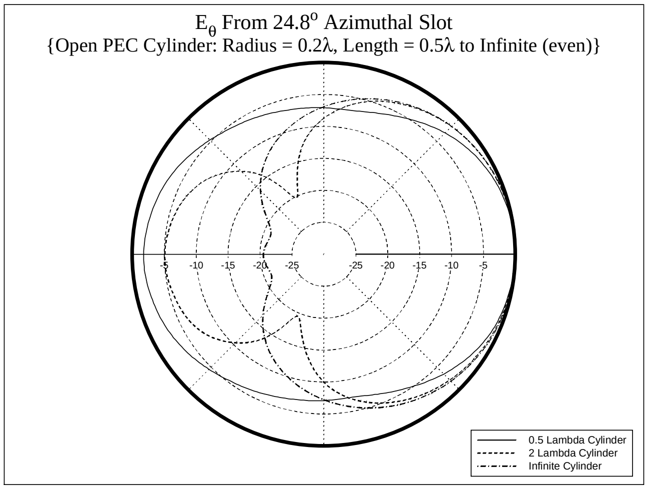

Figure 3–15: E_θ From 24.8^o Azimuthal Slot on Even Wavelength Long PEC Cylinder {0.5λ to Infinite Length}

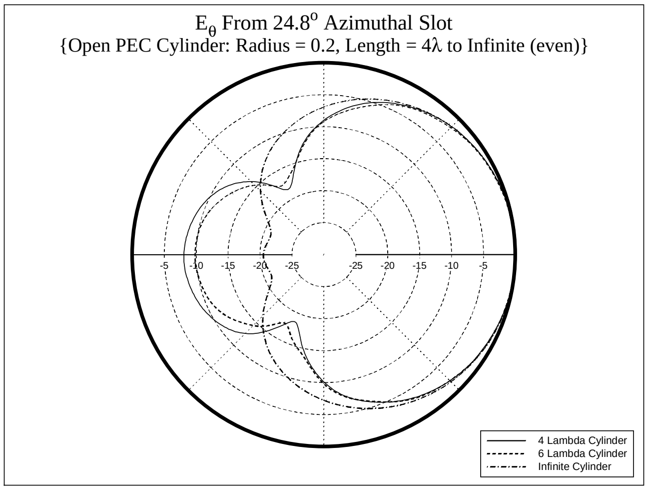

Figure 3–16: E_θ From 24.8^o Azimuthal Slot on Even Wavelength Long PEC Cylinder {4λ to Infinite Length}

For the shorter 0.5λ case, the cylinder length is insufficient to sustain standing waves; thus, the current tends toward a uniform distribution in the *z* direction.

The patterns produced by azimuthal slots mounted on cylinders with a length equal to an even number of wavelengths are presented, again in two parts. *Figure 3–15* presents patterns for slots mounted on cylinders of length 0.5λ, 2λ, and infinite. Patterns from slots mounted on cylinders of length 4λ, 6λ, and infinite are presented in *Figure 3–16*. Due to the small peak on the shadow side ($\phi = 180^o$) of the current distribution, a relatively large back lobe appears in the even-wavelength case. However, the trend is still toward the infinite-length case.

All patterns shown above demonstrate a trend from the finite-length patterns toward the infinite-length case as the length is increased. In addition, they emphasize the dependence of the pattern on cylinder length: in particular, whether the length is an odd or even number of wavelengths.

3.4.2 Axial Slot

An axial slot mounted on a finite-length conducting cylinder will now be addressed. The aperture field in the slot is as defined in Sec. 3.3.2. Since the polarization is in the ϕ direction, the surface electric currents on the conducting cylinder produced by a ϕ-polarized plane wave are needed for the Reciprocity Approach pattern computation. As the cylinder is finite in length, a numerical solution is necessary. An MoM code [31] along with an edge to surface current conversion code was used to compute the required currents. The distribution for a 1λ long, 0.2λ radius cylinder is given in *Figure 3–17*. The distribution is analogous to that produced by a plane wave incident on a flat conducting plate (see *Figure* 2-7).

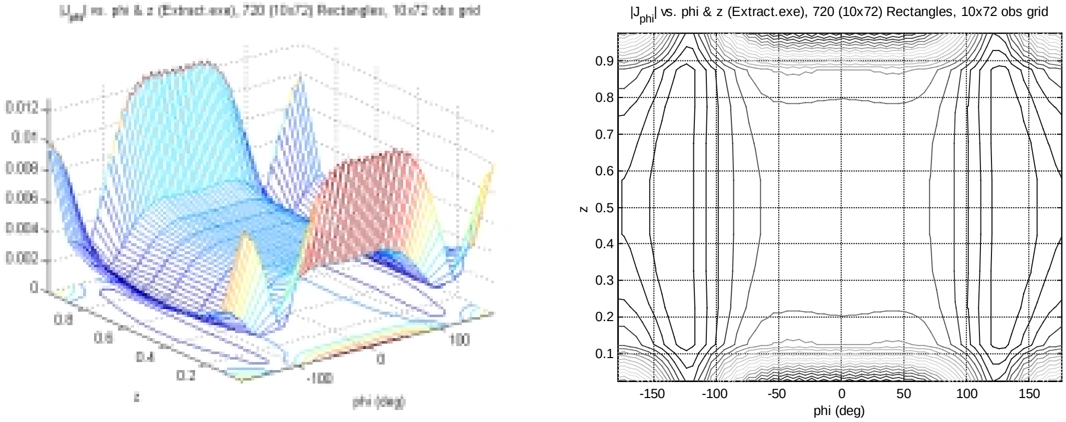

Figure 3–17: J_ϕ Produced by E_ϕ Plane Wave Incident on

1λ Long, 0.2λ radius PEC Cylinder

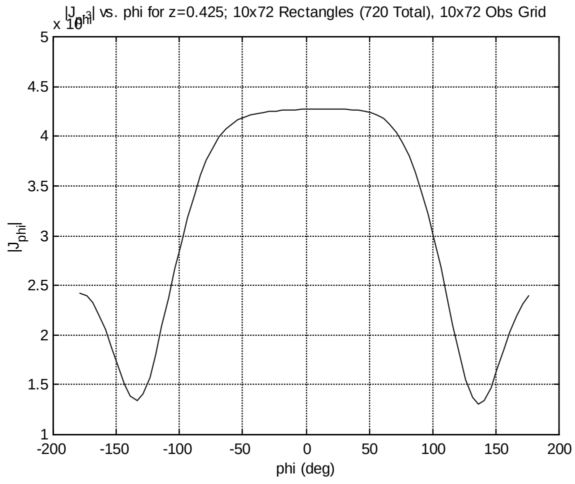

Figure 3–18: J_ϕ *vs*. ϕ @ z-midpoint plane on 1λ Long, 0.2λ radius PEC Cylinder

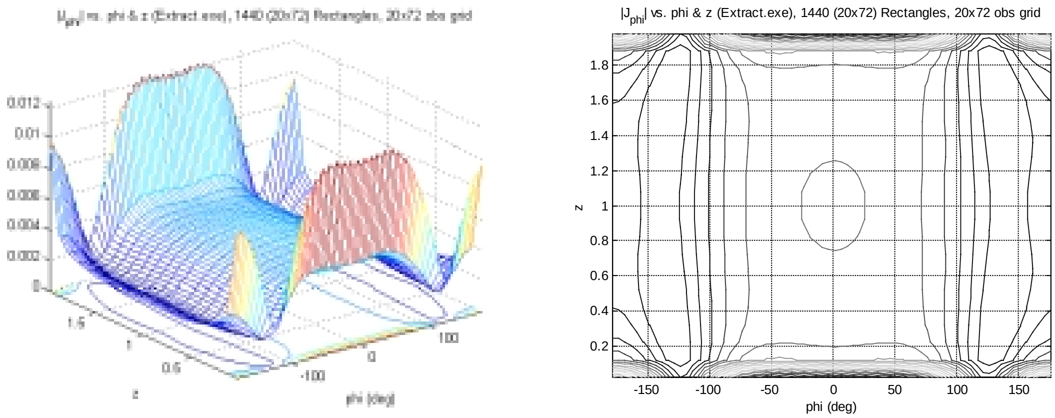

Figure 3–19: J_ϕ Produced by E_ϕ Plane Wave Incident on

2λ Long, 0.2λ radius PEC Cylinder

The current peaks occur on the edges parallel to the polarization direction (ϕ) on the lit side ($\phi = 0^o$). However, in contrast to the plate, the current along the cylinder edge varies due to curvature. A ϕ-cut of the current at the *z*-midpoint plane of the cylinder is shown in *Figure 3–18*.

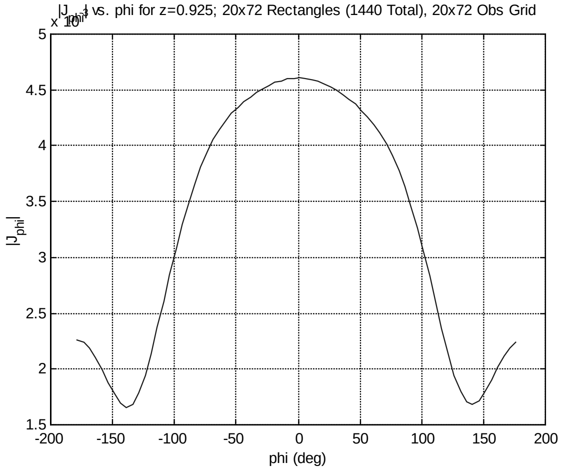

Figure 3–20: J_ϕ *vs.* ϕ @ z-midpoint plane on 2λ Long, 0.2λ radius PEC Cylinder

The current distribution on a 2λ long perfectly conducting cylinder is shown in *Figure 3–19* for comparison to the 1λ case. The distribution along the *z*-midpoint plane of the cylinder is shown in *Figure 3–20*. This plot shows a lower relative shadow side peak as compared to *Figure 3–18*.

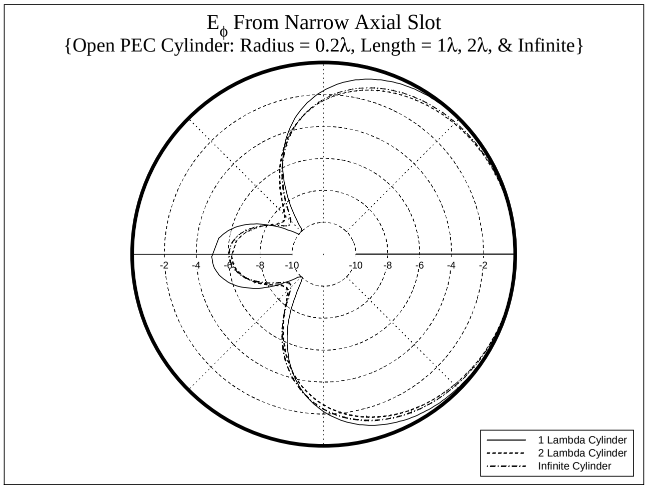

Figure 3–21: E_ϕ From Axial Slot on
1λ, 2λ, and Infinite Length, 0.2λ radius PEC Cylinder

This causes the pattern for the 2λ case to converge closely to the infinite-length case, as can be observed in the pattern plots in *Figure 3–21*. Since the polarization of the aperture field (ϕ) is not interrupted by the truncation of the cylinder in the *z* direction, the patterns for this configuration converge to the infinite-length case more quickly as compared to the azimuthal slot. For the axial slot, a mounting cylinder length of 2λ is sufficient to approximate the behavior of an infinite-length cylinder.

3.5 Summary

This chapter validated the Reciprocity Approach as an accurate means for the computation of radiation patterns produced by conformal antennas. Narrow slots, oriented in both the axial and azimuthal directions, mounted on infinite-length conducting cylinders have been used for the validation. Due to the infinite length, direct analytical formulas exist for pattern computation. These patterns were compared to those produced by the Reciprocity Approach and were found to be in exact agreement.

The chapter then proceeded to an analysis of the same slots, but mounted on finite-length conducting cylinders. The Reciprocity Approach allows efficient modeling of such realistic structures, as opposed to infinite-length objects, which is important for the simulation of actual systems. A trend toward the infinite-length case as the cylinder length is increased is demonstrated and the effect of cylinder length on the radiation pattern is noted. Specifically, significant differences in the pattern occur for the azimuthal slot when the cylinder length is an even as opposed to an odd number of wavelengths. This was caused by the spatial characteristics of the surface current generated on the cylinder by an incident TM^z plane wave. The truncation of the finite cylinder in the z-direction creates standing waves, which in turn cause variations in the pattern with respect to changes in cylinder length. For the axial slot, the patterns converge much more quickly as the cylinder truncation is perpendicular to the polarization of the incident TE^z plane wave. A 2λ length is sufficient to approximate the pattern for the infinite-length cylinder.

Chapter 4

ANALYSIS OF CONFORMAL ANTENNAS MOUNTED ON LARGE STRUCTURES

This chapter describes the modeling of a cavity-backed microstrip patch antenna mounted on a cylindrical conducting object. The antenna is also coated with a surface dielectric for protection from the elements, which is customary in the manufacture of conformal microstrip antennas. The patch antenna was chosen to be elliptical in shape to illustrate the utility and generality of the conformal FDTD technique used in the proposed method: a shape with a curved edge can be modeled more efficiently and accurately using this method compared to the conventional FDTD algorithm. The problem geometry is first introduced, followed by a description of the Reciprocity Approach for computation of the radiation pattern for this particular geometry and a closely related one. Next, fields produced by the conformal antenna on the dielectric superstrate are presented, along with a description of the surface electric currents produced by incident plane waves, which are required components in the pattern calculation. Finally, the resultant radiation patterns are presented and compared to patterns generated by alternate methods on the associated geometry.

4.1 Problem Geometry

The microstrip patch antenna modeled in this chapter is elliptical in shape and is mounted in a rectangular dielectric cavity. This cavity is mounted on an infinite length conducting cylinder to allow comparison of the resulting pattern to other methods. A diagram of the antenna, along with the coordinate systems used in the remainder of this chapter, is presented in *Figure 4–1*:

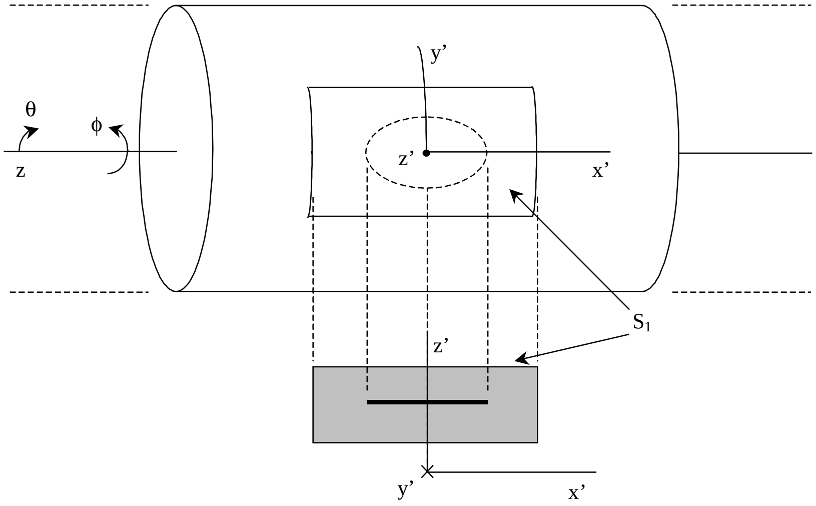

Figure 4–1: Elliptical Patch Antenna Mounted on Infinite Length Conducting Cylinder

The radius of the infinite-length conducting cylinder is $0.631\lambda_o$ ($0.5\lambda_o + 0.2\lambda_d$), where λ_o and λ_d are the wavelengths in free-space and the dielectric cavity, respectively. The relative permittivity of the dielectric cavity is 2.33 (Duroid), while its dimensions are $1\lambda_d$ (*x'*-direction) by $0.8\lambda_d$ (*y'*-direction), with a thickness of $0.2\lambda_d$ ($0.131\lambda_o$). The microstrip patch is an ellipse with major and minor axes of length $0.25\lambda_d$ and $0.20\lambda_d$, respectively. The major axis is aligned with the axis of the cylinder. The patch is probe fed at the optimized coordinate computed by a commercial code (IE3D) for best impedance matching: on the *x'* axis halfway between the left edge and the center of the ellipse. A diagram of the microstrip patch antenna configuration, indicating all dimensions, is shown in *Figure 4–2*:

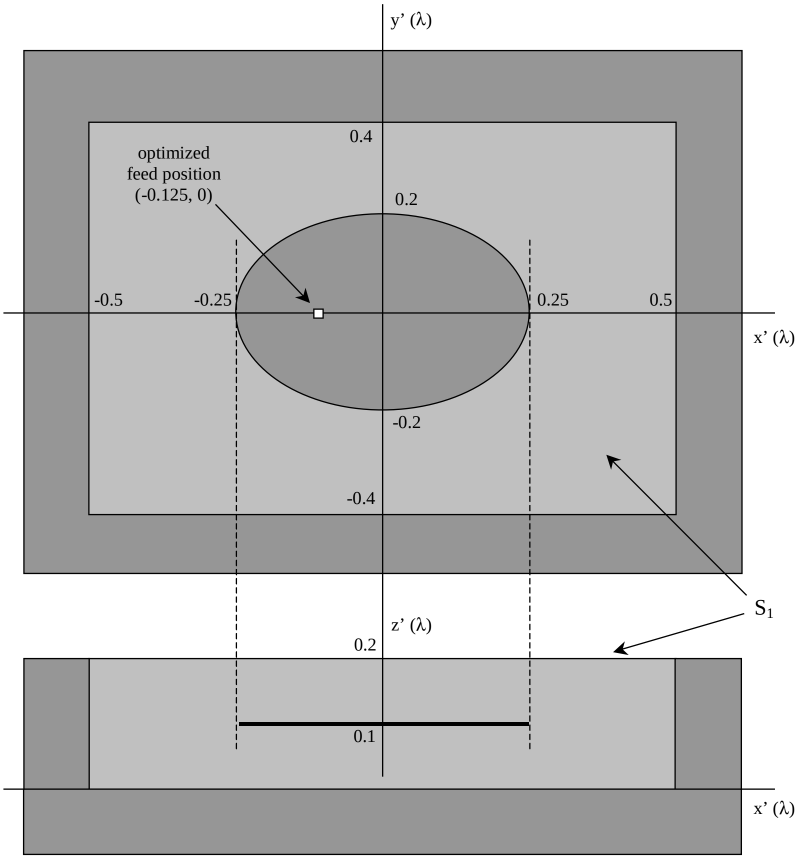

Figure 4–2: Microstrip Patch Antenna Geometry

Thus, the radiated field – for $\theta = 90^o$ – is linearly polarized in the θ (*x'* direction on the patch) direction. This is defined as the co-polarization direction, while the ϕ (*y'* direction on the patch) direction is denoted as the cross-polarization direction. Radiation patterns are computed for both polarizations. The Reciprocity Approach to the pattern computation applied to this specific geometry will be described in the next section.

4.2 Reciprocity Approach to Pattern Computation

The Reciprocity and Surface Equivalence Principles are used to divide the original problem into two parts [58]-[60], as illustrated in Chapter 3, Sec. 3.2. A Reciprocity Approach was also applied in [61], but the Finite Element Method (FEM) was used to compute the equivalent magnetic currents on the radiating surface S_1 (see *Figures 4–1* and *4–2)* instead of the FDTD technique. The only difference between the slot radiation and the microstrip patch analyses is the computation of the equivalent magnetic surface currents $\boldsymbol{M}_1$. For the patch analysis, the FDTD technique is used to compute the electric fields $\boldsymbol{E}_{1(apert)}$ on the surface of the superstrate S_1, while analytical formulas (3.7) and (3.13) are used to compute the surface electric currents $\boldsymbol{J}_{2(cyl)}$ produced by plane waves. The Reciprocity relation for this case, using the identity established in Appendix A and the relation in (3.6), is therefore

$$\left|\mathbf{E}_1\right| = -\frac{1}{Il}\int_V \mathbf{H}_2 \cdot \mathbf{M}_1 \, dV = -\frac{1}{Il}\int_{S_1} \mathbf{E}_{1(apert)} \cdot \mathbf{J}_{S_{2(cyl)}} \, dS \qquad (\ 4.1\ )$$

Two alternate methods, which also utilize the Reciprocity Principle, are employed to compute the radiation pattern emitted by the microstrip patch antenna. Both methods analyze an associated geometry, which is related to the original one described above. Instead of a cavity, the dielectric material in this associated geometry extends to include the surface of the entire cylinder, as shown in *Figure 4–3*:

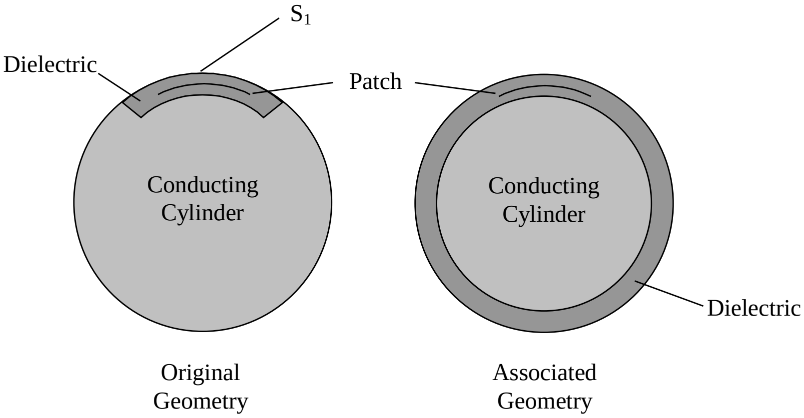

Figure 4–3: Modified Microstrip Patch Antenna Geometry

In this figure, the *z*-axis is directed out of the page and the diagram shows the *xy*-plane cut through the *z*-midpoint of the microstrip patch antenna (refer to *Figure 4–1* for a 3-D view). This geometry was selected to provide a means of comparison to the first method and to quantify the effects of a cavity on the radiation pattern.

In the first of the two alternate methods, a commercial MoM code (IE3D) is used to compute the electric fields at the top surface of the dielectric produced by the patch antenna. The dielectric material is approximated by a flat dielectric slab of infinite extent to allow modeling by the MoM technique. The fields on the surface of the superstrate S_1 (see left side of *Figure 4–3*) in the original geometry are used to compute the pattern. Although fields exist outside this region (at all points on the surface of the dielectric), they are not considered in the calculation. The radiation patterns are computed using the Reciprocity relation applied in the same manner as in the proposed method. This is defined in (4.1). The $\boldsymbol{J}_{S2(cyl)}$ and $\boldsymbol{E}_{1(apert)}$ terms in (4.1) are defined by the analytical formulas in

(3.7) and (3.13), and the surface electric fields computed by IE3D, respectively. The term E_1 is the desired far-zone electric field.

In the second alternate method, the surface electric currents produced on the patch by the probe feed $\boldsymbol{J}_1$, are first determined (by IE3D), using the locally flat dielectric slab approximation. Since the patch is assumed to be perfectly conducting, the tangential electric fields vanish at all points on the patch. Thus, the equivalent magnetic currents, $\boldsymbol{M}_1$ in the Reciprocity Theorem of equation (4.2) below, are zero. The general Reciprocity Theorem is repeated here from Chapter 3 for convenience:

$$\int_{V_2} (\mathbf{E}_1 \cdot \mathbf{J}_2 - \mathbf{H}_1 \cdot \mathbf{M}_2)\, dV = \int_{V_1} (\mathbf{E}_2 \cdot \mathbf{J}_1 - \mathbf{H}_2 \cdot \mathbf{M}_1)\, dV \qquad (4.2)$$

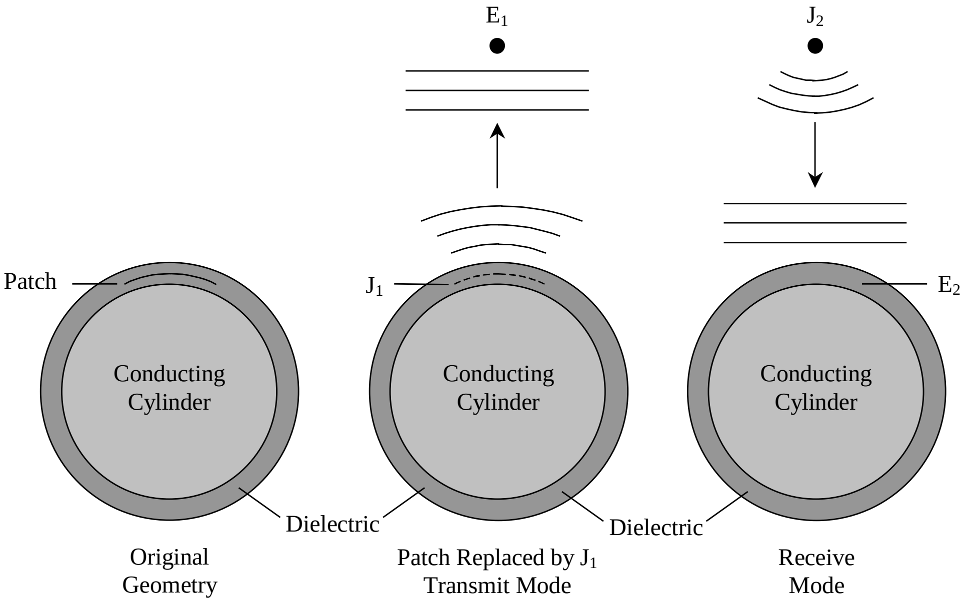

Figure 4–4: E*J Pattern Computation

Using the Surface Equivalence Principle, the patch is then replaced with these currents, yielding a dielectric-coated infinite-length conducting cylinder.

A diagram illustrating the application of both the Surface Equivalence and Reciprocity Principles for this specific geometry is shown in *Figure 4–4*. Instead of solving for the far-zone field directly, the antenna is analyzed in the receive mode as described in Sec. 3.2. A dipole source $\boldsymbol{J_2}$ is positioned at the exact coordinates where the far-zone electric fields are desired. Again, the source is assumed to be an electric current source; thus, $\boldsymbol{M_2}$ is zero. The Reciprocity relation for this geometry (denoted as the ***E*J*** method) is therefore

$$\left|\mathbf{E}_1\right| = \frac{1}{Il}\int_{S_1} \mathbf{E}_2 \cdot \mathbf{J}_1 \, dS \qquad (4.3)$$

The spherical waves emitted by the dipole source become plane waves, which strike the dielectric-coated cylinder. The electric fields $\boldsymbol{E_2}$ produced inside the dielectric by a normally incident plane wave of the appropriate polarization are computed analytically [62]. The volume integral on the right side of (4.2) reduces to one over the surface S_1 of the patch, as $\boldsymbol{J_1}$ is zero everywhere else. The left side reduces to a vector dot product since the point coordinates of the desired far-zone electric field $\boldsymbol{E_1}$ and those of the dipole source $\boldsymbol{J_2}$ are identical. With the surface electric currents $\boldsymbol{J_1}$ obtained from the MoM code and the magnitude of the dipole source $\boldsymbol{J_2}$ being an assumed value, the far-zone electric field $\boldsymbol{E_1}$ can be determined using equation (4.3).

4.3 Conformal FDTD Simulated Aperture Fields

The microstrip patch antenna was simulated using the conformal FDTD method [12], which includes a model of the coaxial line used to feed the patch antenna. A plot of the mesh generator output for the antenna is shown in *Figure 4–5*:

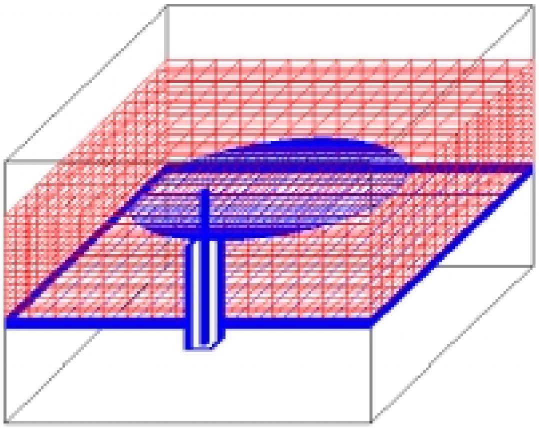

Figure 4–5: FDTD Mesh Discretization of Microstrip Patch Antenna

This diagram shows the elliptical patch inside a dielectric block fed by a coaxial line. A ground plane is placed below the dielectric and the four vertical planes defining the simulation boundary are terminated with a perfect electrical conductor (PEC) in order to model the cavity. A free-space layer of five cells is defined above the dielectric block, followed by a Perfectly Matched Layer (PML) absorbing boundary located above the free-space region. The boundary at the bottom of the simulation domain is also PML, which isolates the inner and outer conductors at the base of the coaxial cable that provides excitation to the patch antenna.

The center conductor of the coaxial feed line is connected to the patch, while the outer conductor is connected to the ground plane beneath the dielectric block. The coaxial line is excited by voltage sources placed between the center and the outer conductors. Eight sources are placed symmetrically about the center conductor to provide excitation to the antenna.

The electric field distribution produced by the patch antenna on the surface of the superstrate is shown in the contour plots of *Figure 4–6*:

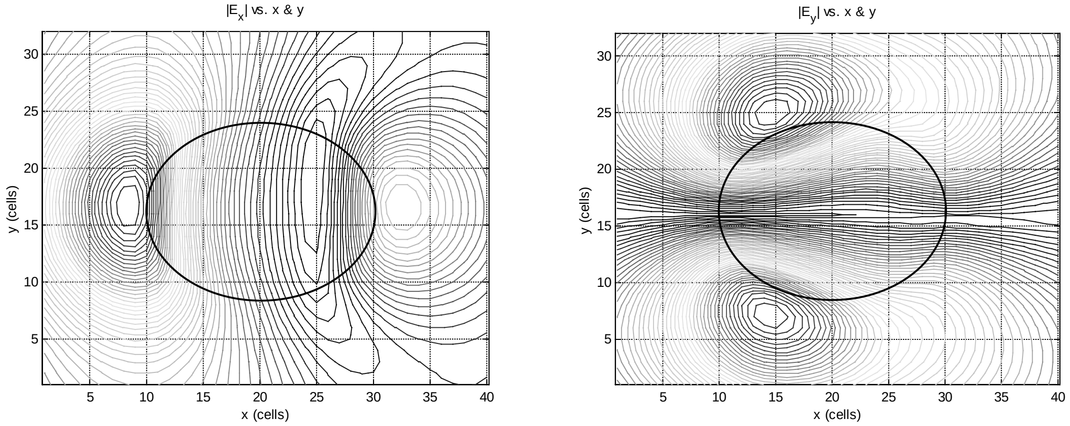

Figure 4–6: Aperture Distributions, $|E_x|$ and $|E_y|$

The above distributions are plotted on a grid of *x* and *y* cells defined by the mesh generator. The elliptical patch (outlines shown in *Figure 4–6*) has *x* and *y* coordinates between 10 and 30, and 8 and 24, respectively. The probe feed is located at $x = 15$, $y = 16$. The distribution resembles that which would be found at the *z'*-level of the patch: zero tangential fields on the patch, and peak intensity fields at the edges of the patch at the *x* and *y* coordinates of the probe. The fields tangential to the surface of the superstrate are not zero, as the field lines diverge from the patch and are no longer vertical as required by boundary conditions at the patch level.

The *x*-polarized fields show a maximum on the left side at the *y'*-midpoint of the patch because the probe is closer to this side. This is due to the field lines having maximum alignment with the *x'*-axis at the *y'*-midpoint and higher intensity on the side where the source is closest to the edge. The maxima for the *y*-polarized fields occur at the edges of the patch at the *x'* coordinates of the probe. This is due to the same reasons cited for the *x'*-polarized field lines. However, the two maxima are 180^{o} out of phase as can be seen in the right-hand plot of *Figure 4–7*:

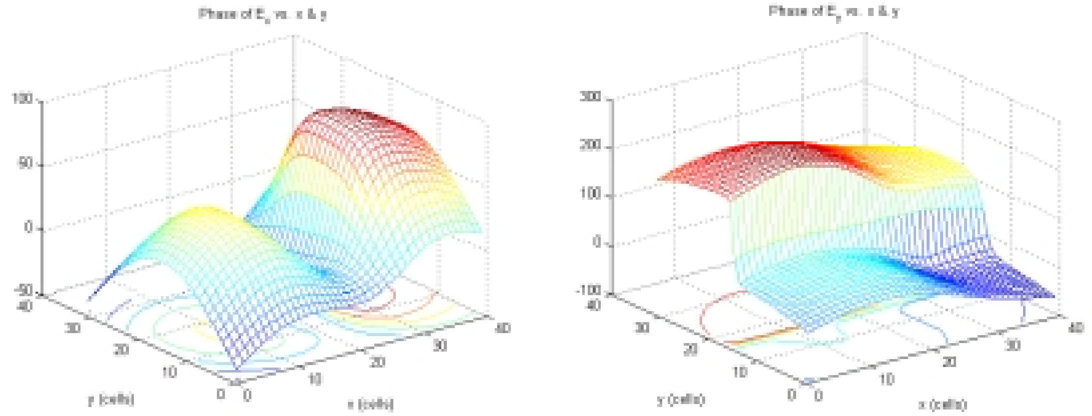

Figure 4–7: Aperture Distributions, Phase of E_x and E_y

A 180^{o} phase shift can be observed in the above figure for the phase of E_y on opposite sides of the $y = 16$ (*y*-midpoint) line. This gives rise to the null at boresight in the cross-polarization (E_y) radiation pattern for the patch antenna (see *Figure 4–13*).

For comparison purposes, the field distributions on the superstrate surface computed by IE3D are presented below. These distributions (both magnitude and phase) are shown in *Figures 4–8* and *4–9*:

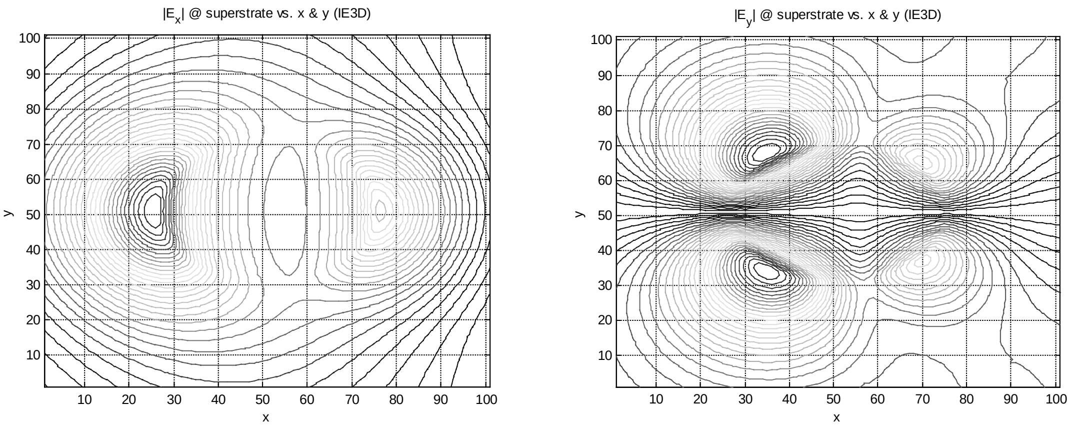

Figure 4–8: Superstrate Field Distributions, |E$_x$| and |E$_y$| (IE3D)

Both distributions computed by IE3D closely resemble those calculated by the conformal FDTD algorithm.

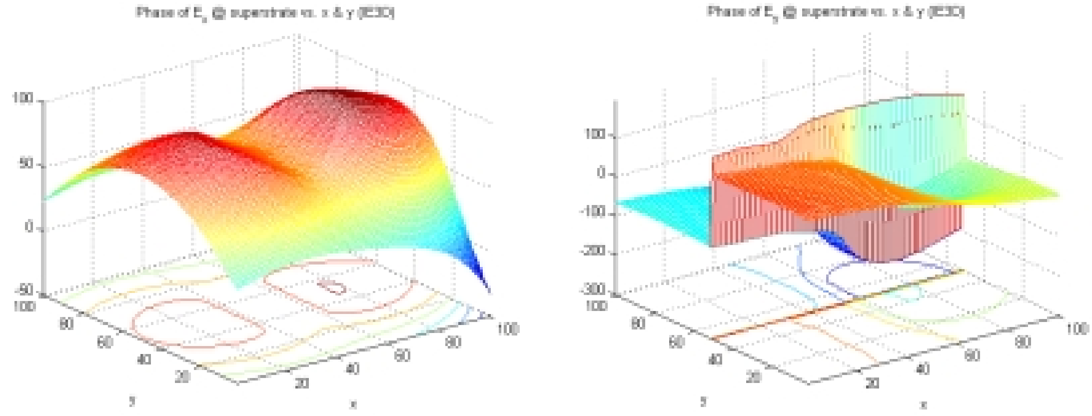

Figure 4–9: Superstrate Field Distributions, Phase of E$_x$ and E$_y$ (IE3D)

It is noted that the IE3D-calculated E_y phase distribution has the same characteristic as the FDTD distribution does: phase differences of 180^o exist on opposite sides of the *y*-midpoint line. These distributions and resultant patterns (*Figure 4–10*) suggest that the radiation characteristics of the microstrip antenna in this case are not affected significantly by the presence of the cavity.

The other required component in the pattern computation is the surface electric currents generated by a normally incident plane wave of first θ then ϕ polarization. Since the mounting cylinder is infinite in length, analytical formulas for these currents have been derived. Plots of these currents are shown in *Figures* 3-3 and 3-6 of Chapter 3 for the θ and ϕ polarized plane waves, respectively.

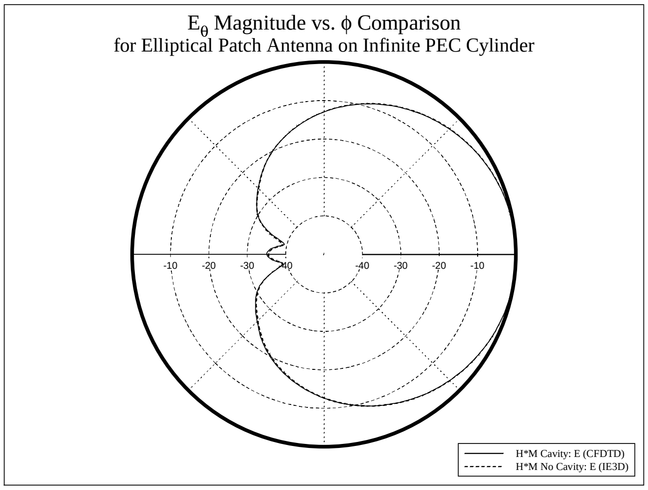

Figure 4–10: E_θ H*M Patterns: Cavity *vs*. No-Cavity

4.4 Reciprocity Based Pattern Computations

Radiation patterns for the cavity backed patch antenna mounted on an infinite-length conducting cylinder and the associated geometry are computed using the proposed method and two alternate techniques, respectively. The patterns are compared and the effect of the cavity on both aperture polarizations is noted. Both the co- *(θ)* and cross- *(ϕ)* polarizations of the radiated field are computed.

4.4.1 Co-Polarization Patterns

The patterns for the co-polarization (E_θ) radiated fields for the proposed method (***H*M***) computation on the original geometry (with cavity) and the ***H*M*** calculation on the associated geometry (no cavity) are shown in *Figure 4–10*.

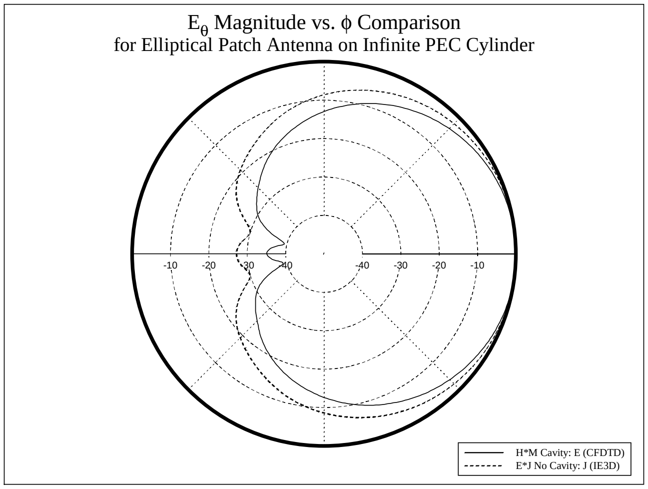

Figure 4–11: E_θ: H*M vs. E*J Patterns

The ***H*M*** notation signifies pattern computation by combination of the source ***M*** currents and the plane wave generated surface ***H*** fields. Even without the cavity, use of the surface electric fields at the position of the cavity (computed by IE3D) yields patterns that are identical with the computation for the original geometry (conformal FDTD computed fields).

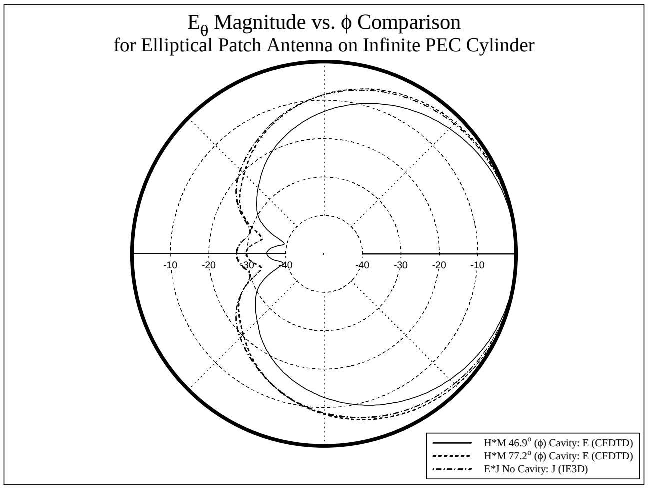

Figure 4–12: E_θ: H*M Original & Widened Aperture *vs*. E*J Patterns

Next, the ***E*J*** method defined in equation (4.3) for the associated geometry is compared to the ***H*M*** generated pattern on the original geometry. The two patterns appear in *Figure 4–11*. In this comparison, the cavity backed patch antenna (***H*M*** computation) has a significantly lower back lobe level compared to the patch mounted within the dielectric coated cylinder (***E*J*** calculation). This can be attributed to the cavity providing directivity to the radiated field, thereby reducing the amount of backside radiation. To support this supposition, the aperture in the conformal FDTD model was widened in the ϕ direction, and the resulting pattern was compared to the ***E*J*** pattern in addition to the original ***H*M*** pattern. This comparison is shown in *Figure 4–12*.

The aperture in the conformal FDTD model was increased from an original ϕ angle of 46.9^{o} to 77.2^{o}. This caused the back lobe to increase in magnitude. These results show that the ***E*J*** pattern will be approached if the aperture is widened to the complete 360^{o}. The aperture could be widened further (beyond 77.2^{o}); however, the flat patch approximation would then be violated. The results also indicate the sensitivity of the patterns for the co-polarized radiated fields to cavity effects.

4.4.2 Cross-Polarization Patterns

This subsection addresses the cross-polarization radiation patterns (E_{ϕ}). For this polarization, the patterns computed by all three methods compare well.

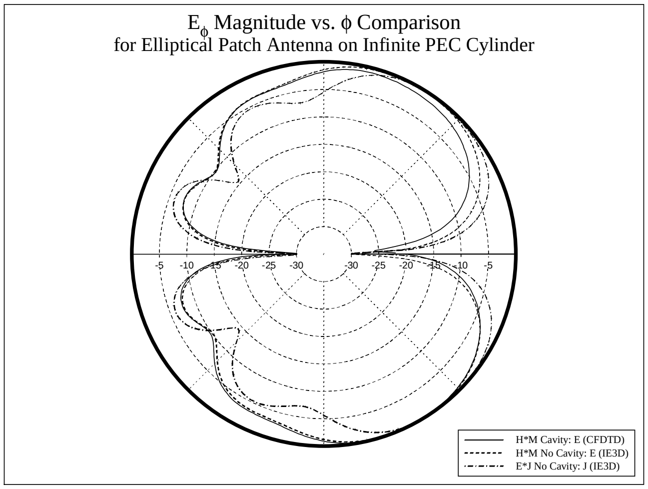

Figure 4–13: E_{ϕ}: H*M (CFDTD) *vs*. H*M (IE3D) & E*J (IE3D) Patterns

The plots appear in *Figure 4–13*. The creeping waves launched from the cavity into the shadow region are less attenuated as compared to the E_θ case. In addition, the $\boldsymbol{E*J}$ pattern contains deeper nulls: these are caused by the higher magnitude creeping waves, which in turn create a stronger standing wave effect. The nulls at $\phi = 0^o$ and 180^o are caused by the two peaks in the $E_{y'}$ aperture distribution (see *Figure 4–6*) being equal in magnitude, but 180^o out of phase (see *Figure 4–7*).

To determine the effect of the cavity on the two aperture polarizations, patterns for slots narrow in the ϕ-direction are plotted for a conducting cylinder infinite in length and with a radius of $0.631\lambda_o$.

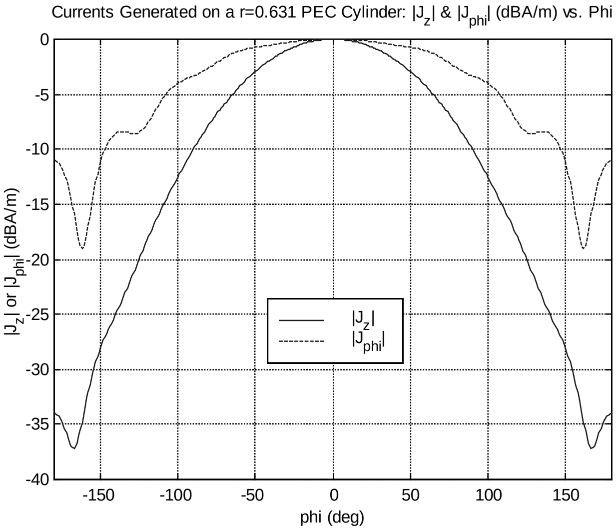

Figure 4–14: $|J_z|$ and $|J_\phi|$ (dBA/m) *vs.* ϕ for r = $0.631\lambda_o$,

Infinite Length Conducting Cylinder

The above plot depicts surface electric currents J_z and J_ϕ produced by E_θ and E_ϕ ($\theta = 90^o$) polarized, normally incident plane waves, respectively. The plots are normalized to their respective maximums and plotted in *dBA/m*. If an azimuthal slot is narrow in the ϕ-direction, its pattern can be plotted directly from the J_z currents, as described in Sec. 3.3.2 for the axial slot narrow in the ϕ-direction. Therefore, the plots of $|J_z|$ and $|J_\phi|$ in *Figure 4–14* also represent the radiation patterns for slots narrow in the ϕ-direction with aperture fields polarized in the z and ϕ directions, respectively.

The radiation patterns of *Figure 4–14* show that E_ϕ polarized creeping waves launched from an axial slot onto the conducting cylinder surface are attenuated less by the slot edges compared to E_θ polarized waves. This explains why the E_ϕ pattern for the cavity-backed elliptical patch antenna compares well with the E_ϕ patterns for the associated geometry: the creeping waves originating from the cavity are of the same approximate magnitude as those propagating on the surface of the dielectric in the associated geometry. In contrast, the E_θ creeping waves emitted by the cavity in the original geometry are significantly attenuated by the cavity edge compared to those free to propagate through and on the dielectric surface in the associated geometry. This can be seen in the current plots of *Figure 4–14* above, where the difference in current magnitudes at $\phi = 180^o$ is approximately 22 dB.

4.5 Summary

This chapter has presented an analysis of an elliptical microstrip patch antenna located within a dielectric cavity and mounted on an infinite-length conducting cylinder. Aperture field distributions produced by the conformal antenna on the dielectric superstrate have been presented and discussed. Patterns computed using the proposed method have been compared to those generated by alternate techniques applied to closely related geometries. It has been demonstrated that aperture fields polarized normal to the cavity edge (in the ϕ direction) produce a larger amount of back radiation compared to tangentially oriented fields. Slots oriented in both the axial and azimuthal directions and narrow in the ϕ direction are used to illustrate this characteristic. Thus, patterns for the E_ϕ aperture fields for the cavity- *vs*. the no-cavity cases compare well, while those for the E_θ polarization do not. However, when only the aperture fields for the no-cavity case are used in the pattern computation, the resulting response compares well to that produced by the proposed method applied to the cavity case.

This chapter has shown that the Reciprocity Approach is an accurate means to pattern computation. In addition, the conformal FDTD portion of the hybrid method allows the modeling of patch antennas with curved shapes, while the MoM technique enables the simulation of mounting structures defined by the CAD program interfaced to the MoM code: PATRAN [63]. Due to its extensive capabilities – entire aircraft and large ocean vessels have been drawn in PATRAN – the mounting structure can essentially have a general shape.

The proposed technique can also be used within an optimization loop to define the best patch antenna shape and location on a given mounting structure in the attainment of a desired radiation pattern. For most design problems, the mounting structure cannot be altered: only the patch antenna shape and location on the structure can be modified to approximate the desired pattern. Due to this constraint, only the FDTD portion of the simulation requires re-calculation within the loop. The MoM-computed currents can be used repeatedly for all subsequent pattern calculations. This significantly enhances the computational efficiency of the proposed hybrid technique, as other methods generally require a re-execution of the entire code. Thus, the time required for convergence to an optimal solution in such optimization schemes as the genetic algorithm, would be reduced substantially by use of the Reciprocity Approach described in this chapter.

Chapter 5

ANALYSIS OF A LARGE REFLECTOR ANTENNA SYSTEM WITH AN ASYMMETRIC FEED

This chapter describes a technique for the analysis of a large reflector antenna system, which is circularly symmetric about its axis of rotation, except for the feed system. The method effectively reduces the computational domain from three to two dimensions by using both the Surface Equivalence and Reciprocity Theorems. The Surface Equivalence Principle is used to transform the original problem into a circularly symmetric geometry, but with an asymmetric source. The resulting system is then analyzed while operating in the reverse mode (receiving instead of transmitting). The Reciprocity Theorem is used to combine the results from the two modes of operation (transmitting and receiving) to construct the radiation pattern, avoiding both the non-symmetric geometry and excitation source.

A Method of Moments (MoM) code is employed for the non-symmetric geometry, while an FDTD algorithm is used to analyze the circularly symmetric 3-D structure. The Equivalence Principle is applied to the results of the MoM analysis to allow modeling of a symmetric geometry by the FDTD technique. The Reciprocity Theorem is then used to combine these results to construct the radiation pattern. The advantage of this method is that it achieves significant savings in computer memory and run time by performing an equivalent 2-D as opposed to a full 3-D FDTD simulation.

The chapter begins with a definition of the problem geometry, followed by a discussion on the application of the Reciprocity and Surface Equivalence Theorems. Since the Surface Equivalence Principle renders a circularly symmetric geometry, an effective 2-D model – which eliminates the azimuthal axis (ϕ) from the 3-D model – can be applied. The approach, called the body of revolution (BOR) – azimuthal harmonics technique, is described next in the chapter. This is followed by a discussion on fields located directly on the axis of symmetry (z-axis). The algorithm also features three improvements over conventional FDTD methods: (i) a conformal approach for improved accuracy in modeling curved dielectric and conductive surfaces; (ii) a tapered excitation source to reduce the error introduced by a truncated plane wave source; and, (iii) non-uniform meshing techniques to maximize computer run-time efficiency. The accuracy of the method is validated via a comparison of simulated and measured results.

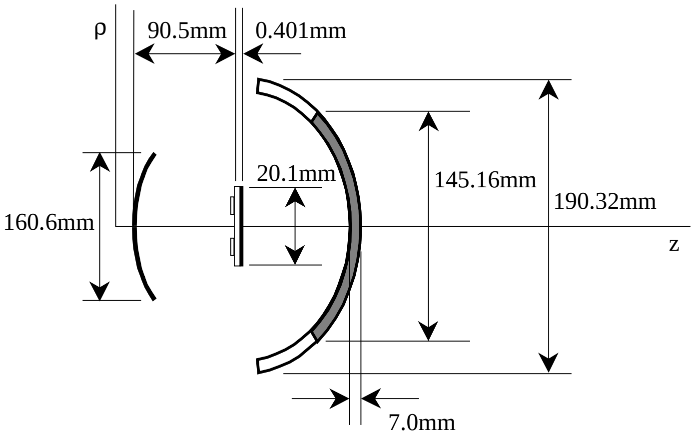

Figure 5–1: Reflector Antenna System

5.1 Problem Geometry

The reflector antenna system, shown in *Figure 5–1*, is considered to outline the procedure. In this figure, the structures to the left, middle, and right are the main reflector (paraboloid), microstrip feed array, and radome structure (composed of two dissimilar dielectric materials), respectively. The antenna has an aperture diameter of 160.6 *mm* (24.09λ), a focal length of 90.5 *mm* (13.58λ), and an operating frequency of 45 GHz. The radome has an outer diameter (including the skirt) of 190.32 *mm* (28.55λ), an inner diameter of 145.16 *mm* (21.77λ), and a thickness of 7.0 *mm* (1.05λ). The inner radome and outer skirt are composed of low-loss (loss tangent less than 0.001) dielectric materials with relative permittivities of 8.5 and 4.2, respectively. The feed antenna dielectric material has a relative permittivity of 4.6. The feed antenna structure, when looking from the reflector, has the geometry shown in *Figure 5–2*:

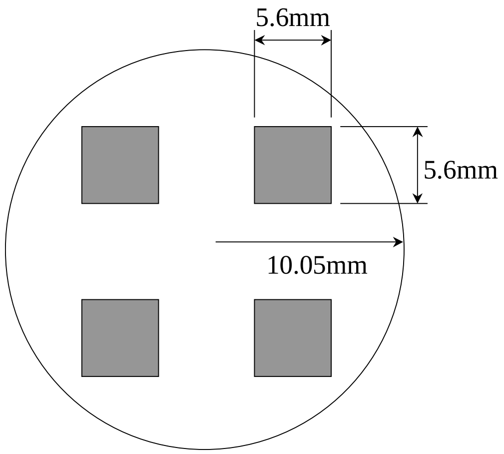

Figure 5–2: Microstrip Patch Antenna Geometry

The feed network for the microstrip patch array of *Figure 5–2* is designed to produce a left-hand circularly polarized (LCP) wave. Thus, for this system, the co-polarization and cross-polarization directions are LCP and RCP (right-hand circularly polarized), respectively. In addition, the system is operated as a monopulse radar. Through its feed network, the system forms nulls (for the difference patterns) along either the elevation or azimuthal plane, or forms a peak at boresight (directly above the center of the antenna) for the sum pattern. *Figure 5–3* defines the null planes:

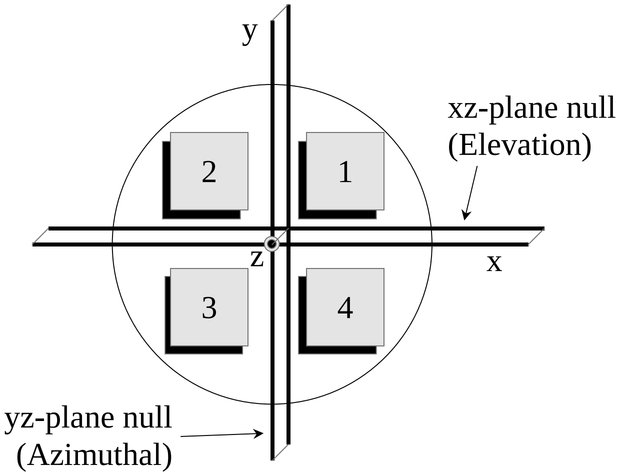

Figure 5–3: Monopulse Radar Operation

When the reflector antenna – together with its feed system – points at boresight (*Figure 5–1*), the reflector and radome structures are both circularly symmetric with respect to the *z*-axis, but the feed array perturbs this symmetry. Application of both the Equivalence and Reciprocity Theorems is used to overcome this asymmetry and reduce the 3-D problem to an effective 2-D one.

5.2 Application of the Equivalence and Reciprocity Theorems

To reduce the number of dimensions in the analysis from three to two, the feed structure is first analyzed using an MoM code to determine the electric currents flowing on the surface of the four microstrip patches. Through application of the Surface Equivalence Principle, the radiating patches in the feed antenna are replaced by the computed currents. This yields a circularly symmetric geometry, but with a non-symmetric excitation source. Instead of analyzing the system in the transmitting mode, the mode of operation is reversed (see *Figure 5–4* below). A dipole source $\boldsymbol{J_2}$ is placed where the far-zone electric field $\boldsymbol{E_1}$ is desired. The fields produced on the surface of the feed dielectric by $\boldsymbol{J_2}$ are then computed.

Transmit Mode: Non-Symmetric (J_1, MoM; need E_1)

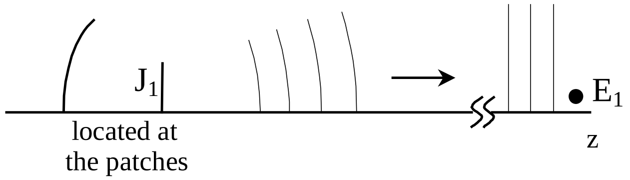

Receive Mode: Circularly-Symmetric (FDTD)

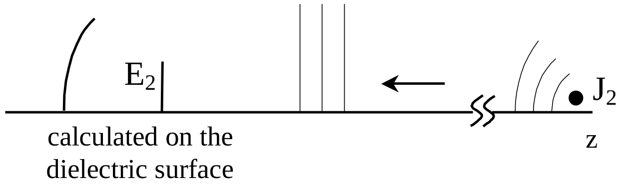

Figure 5–4: Application of Equivalence and Reciprocity Theorems to Original System

Since the geometry is now circularly symmetric, a 2½-D FDTD algorithm for bodies of revolution is employed. The notation 2½-D denotes a 2-D simulation with the availability of all 3-D fields. The Reciprocity Theorem, which relates the fields and currents of two systems, is applied to combine the currents obtained from the MoM code and the fields determined by the FDTD code to yield the far-zone electric field. For the system described above, the Reciprocity Theorem of equation (2.34) reduces to

$$\int_{V_2} \mathbf{E}_1 \cdot \mathbf{J}_2 \, dV = \int_{V_1} \mathbf{E}_2 \cdot \mathbf{J}_1 \, dV \qquad (\ 5.1\ )$$

in which ***E**$_1$* and ***J**$_2$* are the desired far-zone electric field (transmit mode) and the dipole source (receive mode) placed where ***E**$_1$* is desired, respectively. On the right-hand side, ***E**$_2$* and ***J**$_1$* are the fields produced on the surface of the circularly symmetric feed dielectric (receive mode) and the electric currents produced on the surface of the microstrip patches by the excitation sources (transmit mode), respectively. Note that the left-hand side reduces to a simple vector dot-product as the point coordinates of ***E**$_1$* and ***J**$_2$* are identical, while the right-hand side reduces to a surface integral over the area of the four radiating patches since the electric currents (***J**$_1$*) are zero everywhere else. Also, since the value of the far-zone field relative to the maximum is required for the pattern, ***J**$_2$* is arbitrarily set to unity. Since the right-hand side of equation (5.1) is known from the results of the MoM (***J**$_1$*) and FDTD (***E**$_2$*) computations, the far-zone electric field (***E**$_1$*) can be determined.

5.3 Azimuthal Harmonics

This section describes the method used to model the problem geometry in an equivalent 2-D simulation. The Equivalence Principle renders the geometry circularly symmetric about the *z*-axis, thus allowing a 2-D simulation. Due to this circular symmetry, all fields are required to be cyclical in the ϕ-direction; thus, they can be expanded as follows [17], [64]

$$\begin{aligned}\mathbf{E} &= \sum_{m=0}^{\infty} \mathbf{E}_{e_m} \cos(m\phi) + \mathbf{E}_{o_m} \sin(m\phi) \\ \mathbf{H} &= \sum_{m=0}^{\infty} \mathbf{H}_{e_m} \cos(m\phi) + \mathbf{H}_{o_m} \sin(m\phi)\end{aligned} \qquad (\ 5.2\ )$$

where E_e and H_e, and E_o and H_o represent even and odd harmonics of the electric and magnetic fields, respectively. Using Faraday's Law

$$\nabla \times \mathbf{E} = -\mu \frac{\partial \mathbf{H}}{\partial t} \qquad (\ 5.3\ )$$

and expanding the curl of the electric field in cylindrical coordinates

$$\begin{aligned}\nabla \times \mathbf{E} = \hat{\rho}\left(\frac{1}{\rho}\frac{\partial E_z}{\partial \phi} - \frac{\partial E_\phi}{\partial z}\right) + \hat{\phi}\left(\frac{\partial E_\rho}{\partial z} - \frac{\partial E_z}{\partial \rho}\right) \\ + \hat{z}\left(\frac{1}{\rho}\frac{\partial}{\partial \rho}\left(\rho E_\phi\right) - \frac{1}{\rho}\frac{\partial E_\rho}{\partial \phi}\right)\end{aligned} \qquad (\ 5.4\ )$$

yields the following relations for the ρ, ϕ, and *z* directions, respectively

$$\frac{1}{\rho}\frac{\partial E_z}{\partial \phi} - \frac{\partial E_\phi}{\partial z} = -\mu \frac{\partial H_\rho}{\partial t} \qquad (\ 5.5\ )$$

$$\frac{\partial E_\rho}{\partial z} - \frac{\partial E_z}{\partial \rho} = -\mu \frac{\partial H_\phi}{\partial t} \tag{5.6}$$

$$\frac{1}{\rho}\frac{\partial}{\partial \rho}\left(\rho E_\phi\right) - \frac{1}{\rho}\frac{\partial E_\rho}{\partial \phi} = -\mu \frac{\partial H_z}{\partial t} \tag{5.7}$$

Substituting equation (5.2) into (5.5)-(5.7) above and solving for the coefficients of *sin(mϕ)* and *cos(mϕ)* yields

$$\frac{m}{\rho} E_{z_{e,m}} + \frac{\partial E_{\phi_{o,m}}}{\partial z} = \mu \frac{\partial H_{\rho_{o,m}}}{\partial t} \tag{5.8}$$

$$\frac{m}{\rho} E_{z_{o,m}} - \frac{\partial E_{\phi_{e,m}}}{\partial z} = -\mu \frac{\partial H_{\rho_{e,m}}}{\partial t} \tag{5.9}$$

$$\frac{\partial E_{\rho_{o,m}}}{\partial z} - \frac{\partial E_{z_{o,m}}}{\partial \rho} = -\mu \frac{\partial H_{\phi_{o,m}}}{\partial t} \tag{5.10}$$

$$\frac{\partial E_{\rho_{e,m}}}{\partial z} - \frac{\partial E_{z_{e,m}}}{\partial \rho} = -\mu \frac{\partial H_{\phi_{e,m}}}{\partial t} \tag{5.11}$$

$$\frac{1}{\rho}\frac{\partial}{\partial \rho}\left(\rho E_{\phi_{o,m}}\right) + \frac{m}{\rho} E_{\rho_{e,m}} = -\mu \frac{\partial H_{z_{o,m}}}{\partial t} \tag{5.12}$$

$$\frac{1}{\rho}\frac{\partial}{\partial \rho}\left(\rho E_{\phi_{e,m}}\right) - \frac{m}{\rho} E_{\rho_{o,m}} = -\mu \frac{\partial H_{z_{e,m}}}{\partial t} \tag{5.13}$$

in which no ϕ-derivatives appear, as all expansion terms are independent of ϕ. These relations are converted to difference equations as described in Sec. 2.1.1. The time-advanced term in each resulting difference equation is determined as a function of all variable values at the previous time increment. The time derivatives appear on the right-hand sides of equations (5.8)-(5.13).

To add the source to the model, Ampere's Law with Maxwell's correction is used

$$\nabla \times \mathbf{H} = \varepsilon \frac{\partial \mathbf{E}}{\partial t} + \sigma \mathbf{E} + \mathbf{J}_S \qquad (5.14)$$

in which $\boldsymbol{J}_S$ is the source electric current. Since the source is located in the far-zone, it becomes a plane wave source in the vicinity of the antenna system. Therefore, this source will be considered as an electric field plane wave source, omitting the factor $-j\frac{\omega\varepsilon}{4\pi r}$ associated with radiating dipole sources in the far-zone. This factor is common for all incidence angles and will not affect the pattern computation relative to the maximum value. The following rotation matrix is used to convert Cartesian coordinate source electric fields to the cylindrical coordinate system

$$\begin{pmatrix} E_\rho \\ E_\phi \end{pmatrix} = \begin{pmatrix} \cos\phi & \sin\phi \\ -\sin\phi & \cos\phi \end{pmatrix} \begin{pmatrix} E_x \\ E_y \end{pmatrix} \qquad (5.15)$$

If an E_x^i magnitude (x polarized) incident plane wave is desired, then

$$\begin{aligned} E_\rho &= E_x^i \cos\phi \\ E_\phi &= -E_x^i \sin\phi \end{aligned} \qquad (5.16)$$

An incident E_x^i plane wave propagating towards the origin (see *Figure 5–5*) at a polar angle θ_i away from the z-axis can be written in terms of a θ-polarized electric field E_o as in (5.17) [32]:

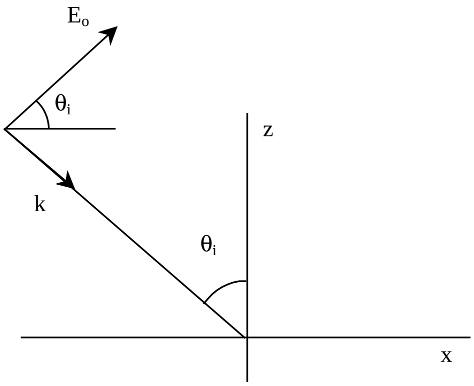

Figure 5–5: Incident E$_\theta$ Plane Wave

$$E_x^i = E_o \cos\theta_i e^{jkz\cos\theta_i} e^{-jkx\sin\theta_i} \tag{5.17}$$

Expanding the $e^{-jkx\sin\theta_i}$ factor in terms of Bessel functions [32] yields

$$\begin{aligned} E_x^i &= E_o \cos\theta_i e^{jkz\cos\theta_i}\left[J_0(k\rho\sin\theta_i) + 2\sum_{n=1}^{\infty} j^{-n} J_n(k\rho\sin\theta_i)\cos(n\phi)\right] \\ &= E_o \cos\theta_i e^{jkz\cos\theta_i}\sum_{n=0}^{\infty} a_n \cos(n\phi) \end{aligned} \tag{5.18}$$

where $a_n = 2j^{-n}J_n(k\rho\sin\theta_i)$ for $n > 0$, $a_o = J_0(k\rho\sin\theta_i)$. Solving for E_ρ and E_ϕ by combining (5.16) and (5.18), and using the following trigonometric identities

$$\begin{aligned} \cos\alpha\cos\beta &= \frac{1}{2}[\cos(\alpha+\beta) + \cos(\alpha-\beta)] \\ \sin\alpha\cos\beta &= \frac{1}{2}[\sin(\alpha+\beta) - \sin(\beta-\alpha)] \end{aligned} \tag{5.19}$$

the following relations for E_ρ and E_ϕ result

$$
\begin{aligned}
E_\rho &= \frac{1}{2}E_o\cos\theta_i e^{jkz\cos\theta_i}\sum_{n=0}^{\infty}a_n\left\{\cos[(n+1)\phi]+\cos[(n-1)\phi]\right\}\\
E_\phi &= -\frac{1}{2}E_o\cos\theta_i e^{jkz\cos\theta_i}\sum_{n=0}^{\infty}a_n\left\{\sin[(n+1)\phi]-\sin[(n-1)\phi]\right\}
\end{aligned}
\qquad (\ 5.20\ )
$$

Equation (5.20) is substituted into (5.14) for the two respective electric field components. Due to the *n+1* and *n-1* indices in (5.20) above, the *m* index in (5.2) must be set to these two values in order to solve for the *sin(mφ)* and *cos(mφ)* coefficients. For *m = n+1*, solving for the *cos(mφ)* coefficients yields the following relation

$$
\frac{n+1}{\rho}H_{z_{o,n+1}}-\frac{\partial H_{\phi_{e,n+1}}}{\partial z}=\varepsilon\frac{\partial E_{\rho_{e,n+1}}}{\partial t}+\frac{\sigma}{2}E_o\cos\theta_i e^{jkz\cos\theta_i}a_n \qquad (\ 5.21\ )
$$

Solving for the *sin(mφ)* coefficients,

$$
\frac{\partial H_{\rho_{o,n+1}}}{\partial z}-\frac{\partial H_{z_{o,n+1}}}{\partial \rho}=\varepsilon\frac{\partial E_{\phi_{o,n+1}}}{\partial t}-\frac{\sigma}{2}E_o\cos\theta_i e^{jkz\cos\theta_i}a_n \qquad (\ 5.22\ )
$$

For *m = n-1*, the *cos(mφ)* coefficients are related by

$$
\frac{n-1}{\rho}H_{z_{o,n-1}}-\frac{\partial H_{\phi_{e,n-1}}}{\partial z}=\varepsilon\frac{\partial E_{\rho_{e,n-1}}}{\partial t}+\frac{\sigma}{2}E_o\cos\theta_i e^{jkz\cos\theta_i}a_n \qquad (\ 5.23\ )
$$

Finally, for the *sin(mφ)* coefficients, the following relation results

$$
\frac{\partial H_{\rho_{o,n-1}}}{\partial z}-\frac{\partial H_{z_{o,n-1}}}{\partial \rho}=\varepsilon\frac{\partial E_{\phi_{o,n-1}}}{\partial t}+\frac{\sigma}{2}E_o\cos\theta_i e^{jkz\cos\theta_i}a_n \qquad (\ 5.24\ )
$$

The update equation for E_z is derived from the source-free relation [coefficients of *cos(mφ)*]

$$\frac{1}{\rho}\frac{\partial}{\partial\rho}\left(\rho H_{\phi_{e,m}}\right)-\frac{m}{\rho}H_{\rho_{o,m}}=\varepsilon\frac{\partial E_{z_{e,m}}}{\partial t} \qquad (5.25)$$

Since the total fields in (5.2) can be expressed in terms of either the odd or even expansion coefficients, and (5.21)-(5.24) have specified $E_{\rho e}$ and $E_{\phi o}$ (due to the coefficient relations), only these and E_{ze}, $H_{\rho o}$, $H_{\phi e}$, and H_{zo} are determined. The other six terms from (5.2) are set to zero. Hence, only the coefficients of $\cos(m\phi)$ are considered in (5.25) above. Setting the six terms to zero eliminates (5.9), (5.10), and (5.13); therefore, only (5.8), (5.11), and (5.12) in addition to (5.21) through (5.25) are used to compute the required expansion coefficients. This set of equations is converted to difference equations as described in Sec. 2.1.1, and the time-advanced term in each relation is determined.

5.4 Fields Located at the Z-Axis

The cell structure used in this Body of Revolution (BOR) simulation is illustrated in *Figure 5–6*. For the field $E_n(i, j)$, n, i, and j represent the field magnitude, polarization direction, and the ρ and z cell numbers, respectively. The fields located on the z-axis include E_ρ, H_ϕ, and H_z. These quantities must be shown to be finite to successfully model the problem geometry. In this model, the first cell in the ρ direction is a half-cell. The H_z field can be determined by using Faraday's Law in integral form,

$$\oint_L \mathbf{E}\cdot d\mathbf{l}=-\mu\int_S\frac{\partial\mathbf{H}}{\partial t}\cdot d\mathbf{S} \qquad (5.26)$$

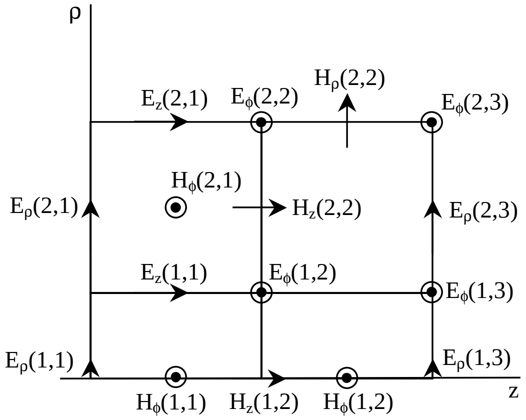

Figure 5–6: 2-D BOR Cell Structure

in which the electric field is ϕ-polarized and the line integral is taken around the z-axis in the ϕ direction. Since

$$\oint_L E_{\phi_o} \sin(m\phi) d\phi = 0 \qquad (5.27)$$

for all m, H_z at the z-axis is zero. Regarding $H_{\phi e}$, (5.25) is converted into finite difference form as

$$\begin{aligned} E_z^{n+1}(i,j) &= E_z^n(i,j) \\ &\quad + \frac{\Delta t}{\varepsilon}\left[\frac{\rho_{i+\frac{1}{2}} H_\phi^n(i,j) - \rho_{i-\frac{1}{2}} H_\phi^n(i-1,j)}{\rho_i \Delta\rho} - \frac{m H_\rho^n(i,j)}{\rho_i}\right] \end{aligned} \qquad (5.28)$$

in which the superscripts represent the time index and ρ_i represents the ρ-coordinate for the i^{th} cell relative to the z-axis. In (5.25), the derivative of the entire product is taken as opposed to using the chain rule. For $i = 1$, $\rho_{i-½} = 0$ as this ρ coordinate is exactly on the z-

axis. Therefore, the value for $H_\phi^n(0, j)$ is not needed. The field $E_z^{n+1}(1, j)$ is found from the off-axis magnetic fields $H_\phi^n(1, j)$ and $H_\rho^n(1, j)$, in addition to the previous value $E_z^n(1, j)$.

Regarding the last on-axis field, E_ρ, we examine the update equation for H_ϕ converted to finite difference form from (5.11),

$$\begin{aligned} H_\phi^{n+1}(i, j) &= H_\phi^n(i, j) \\ &+ \frac{\Delta t}{\mu}\left[\frac{E_z^n(i, j) - E_z^n(i-1, j)}{\Delta\rho} - \frac{E_\rho^n(i, j) - E_\rho^n(i, j-1)}{\Delta z}\right] \end{aligned} \qquad (\ 5.29\ )$$

For $i = 1$, $E_z^n(0, j)$ does not exist (it is beyond the *z*-axis), and since the value for $H_\phi^{n+1}(0, j)$ is not needed, the values for $E_\rho^n(1, j)$ and $E_\rho^n(1, j-1)$ are also unnecessary. Therefore, all of the fields located on the *z*-axis can be set to zero without affecting the accuracy of the simulation.

5.5 Conformal Method for Modeling Perfect Conductors

The method used to model the curved conducting surface of the main parabolic reflector is described in [28]. However, a 2-D equivalent of the 3-D technique employed in [28] is used here. In this method, if a curved conducting surface intersects a cell, it is approximated by a straight line connecting the two intersection points (see *Figure 5–7*). Only magnetic field update equations are affected by this technique as electric fields are zero within PEC regions and these fields are used in the computation of the magnetic fields.

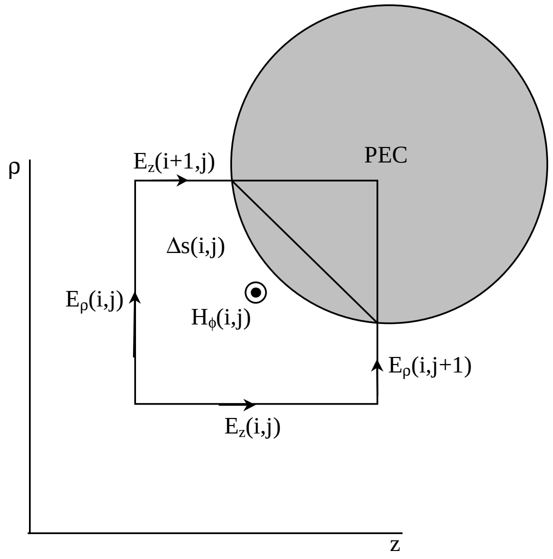

Figure 5–7: Conformal Method for Perfect Conductors

Electric fields are computed from these resultant magnetic fields. For H_ϕ, equation (5.26) is converted to the finite difference form

$$H_\phi^{n+1}(i,j) = H_\phi^n(i,j) - \frac{\Delta t}{\mu \Delta s(i,j)} \begin{bmatrix} \Delta\rho(i,j)E_\rho^n(i,j) + \Delta z(i+1,j)E_z^n(i+1,j) \\ -\Delta\rho(i,j+1)E_\rho^n(i,j+1) - \Delta z(i,j)E_z^n(i,j) \end{bmatrix} \qquad (5.30)$$

where $\Delta\rho(i,j)$ and $\Delta z(i,j)$ represent the length of the cell edges located outside the PEC material in the ρ and z directions, respectively, for the i^{th} and j^{th} cell with respect to the ρ and z axes. The $\Delta s(i,j)$ term denotes the area of the distorted cell bounded by the straight line approximation to the curve and the remaining cell edges. The cell size is chosen to be sufficiently small to allow only one intersection between a conducting surface and any cell (*i.e.*: there is only one closed line integral per cell). Using a similar procedure, the update equation for H_ρ – derived from (5.8) – is expressed as

$$\begin{aligned} H_\rho^{n+1}(i,j) &= H_\rho^{n}(i,j) \\ &+ \frac{\Delta t}{\mu}\left[\frac{m}{\rho}\frac{\Delta z(i,j)}{\Delta z_o(i,j)}E_z^n(i,j) + \frac{E_\phi^n(i,j) - E_\phi^n(i,j-1)}{\Delta z_o(i,j)}\right] \end{aligned} \tag{5.31}$$

where $\Delta z_o(i, j)$ is the full cell length in the z direction for cell (i, j). Note that the factor $\Delta z(i, j)/\Delta z_o(i, j)$ has been added since E_z is zero along the part of the cell within the PEC material. Converted to finite difference form from (5.12), the update equation for H_z is written as

$$H_z^{n+1}(i,j) = H_z^{n}(i,j) - \frac{\Delta t}{\mu}\left[\begin{array}{l} \dfrac{m}{\rho_{i+\frac{1}{2}}}\dfrac{\Delta\rho(i,j)}{\Delta\rho_o(i,j)}E_\rho^n(i,j) \\ + \dfrac{\rho_{i+1}E_\phi^n(i,j) - \rho_i E_\phi^n(i-1,j)}{\rho_{i+\frac{1}{2}}\Delta\rho_o(i,j)} \end{array}\right] \tag{5.32}$$

where $\Delta\rho_o(i, j)$ is the full cell length in the ρ direction for cell (i, j). As done previously, the derivative of the first term of (5.12) has been taken for the entire product rather than by the chain rule. As was done for (5.31) above, the factor $\Delta\rho(i, j)/\Delta\rho_o(i, j)$ has been added since E_ρ is zero along the part of the cell within the PEC material. The remaining fields, E_ρ and E_ϕ, are computed by finite difference relations derived from (5.21) through (5.24).

5.6 Modeling of Curved Dielectric Surfaces

Curved dielectric surfaces in the simulation domain are modeled using a technique described in [65]. Effective permittivities and conductivities are computed from weighted averages as follows

$$X_{eff}(i,j) = \frac{1}{\Delta s_o(i,j)} \int_S X(r)\,dS \qquad (\ 5.33\ )$$

where X_{eff}, $X(r)$, and $\Delta s_o(i, j)$ represent the effective and actual (at coordinate r) permittivity or conductivity, and the area of cell (i, j), respectively. The integral is taken over the area of cell (i, j) (S). Using (5.33), the effective permittivity and conductivity can be expressed as

$$\varepsilon_{eff}(i,j) = \frac{\varepsilon_o}{\Delta s_o(i,j)} \left[\varepsilon_r \Delta s_d(i,j) + \Delta s_f(i,j)\right] \qquad (\ 5.34\ )$$

$$\sigma_{eff}(i,j) = \sigma_d \frac{\Delta s_d(i,j)}{\Delta s_o(i,j)} \qquad (\ 5.35\ )$$

since ε_r and σ are 1 and 0, respectively, for free space. In the above equations, $\Delta s_d(i, j)$ and $\Delta s_f(i, j)$ are the area enclosed by the dielectric and free space, respectively, for cell (i, j).

5.7 Tapered Excitation Source and Non-Uniform Mesh

To prevent reflections from the first Mur absorbing boundary [23] used in this algorithm, a tapered plane wave excitation source was used. Due to the high reflectivity of the Mur boundary condition at the glancing angle, the plane wave source was tapered from full intensity at 40 cells from the maximum ρ boundary to zero at the boundary. All objects within the simulation domain were contained inside this 40-cell border to obtain plane wave effects.

To further limit boundary effects and to enhance computational efficiency, a coarse grid was used between the maximum ρ boundary and the objects in the simulation domain. The grid was made finer in regions where the fields have relatively large rates of spatial variation.

5.8 Numerical Results

To compute the far-zone fields for the left-hand circularly polarized antenna system, first an x-polarized source is applied, followed by a y-polarized source. These sources produce both x and y polarized fields on the surface of the feed dielectric. To compute both the co- and cross-polarization x and y directed fields, a combination of these resultant surface fields with quadrature phasing, is computed as follows:

$$E_x^{copol} = E_{xx} - jE_{xy} \ , \ E_y^{copol} = E_{yx} - jE_{yy} \tag{5.36}$$

$$E_x^{crosspol} = E_{xx} + jE_{xy} \ , \ E_y^{crosspol} = E_{yx} + jE_{yy} \tag{5.37}$$

in which the general field E_{nm} represents an *n*-polarized field produced by an *m*-polarized source. To calculate the far-zone fields using the Reciprocity Approach, the following relations are used

$$E_{far-zone}^{copol} \propto \int_S \left(E_x^{copol} \cdot J_x + E_y^{copol} \cdot J_y \right) dS \qquad (5.38)$$

$$E_{far-zone}^{crosspol} \propto \int_S \left(E_x^{crosspol} \cdot J_x + E_y^{crosspol} \cdot J_y \right) dS \qquad (5.39)$$

where *S* is the surface of the radiating patches. The gain of the system is calculated from the ratio of this field intensity to that produced by an isotropic radiator, for different configurations or excitations.

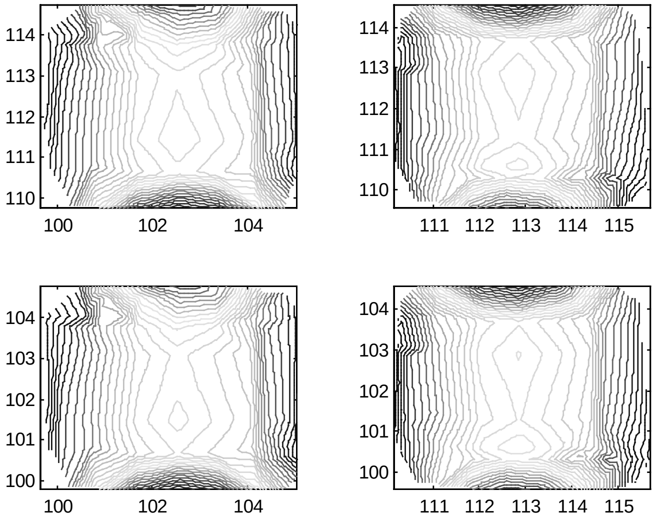

Figure 5–8: |J$_x$| Current Distribution, Azimuthal Difference Patterns

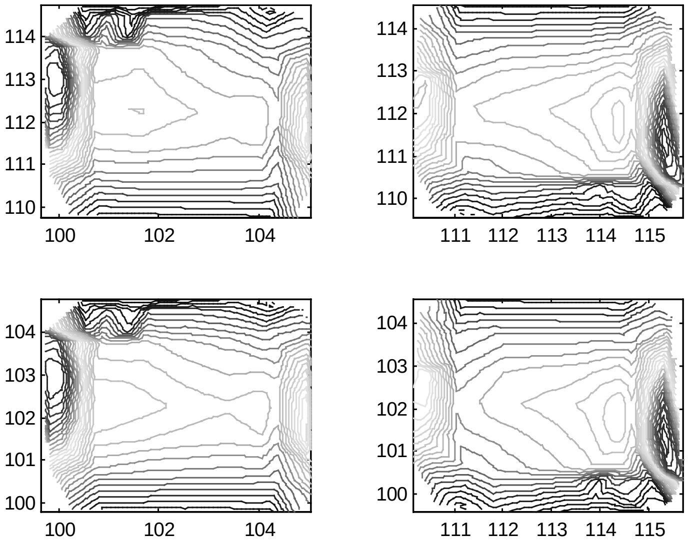

Figure 5–9: $|J_y|$ Current Distribution, Azimuthal Difference Pattern

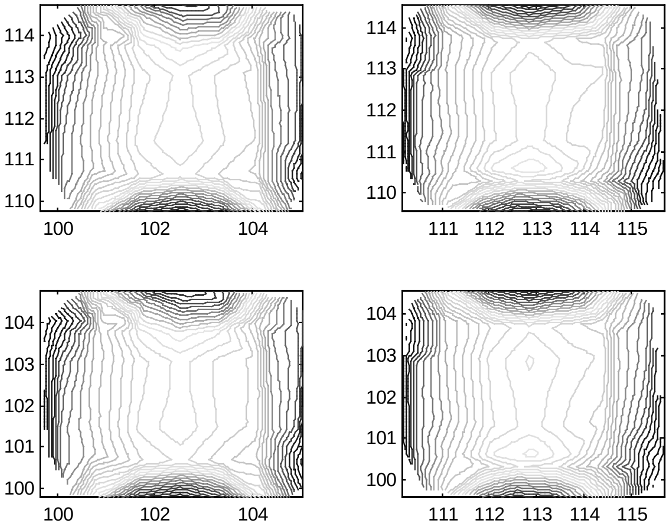

Figure 5–10: $|J_x|$ Current Distribution, Elevation Difference Pattern

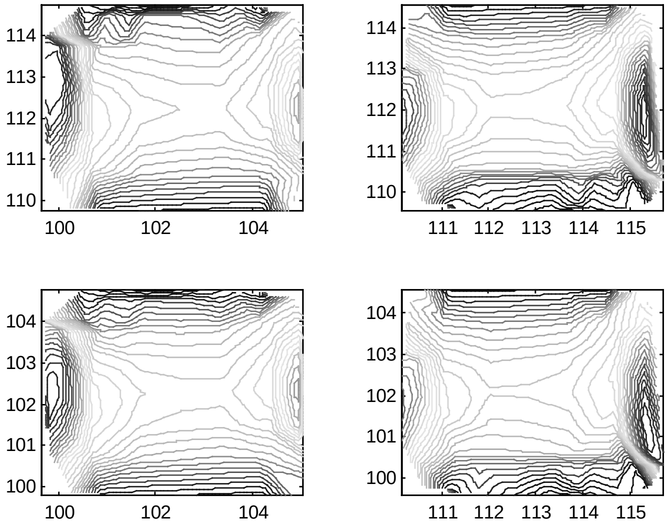

Figure 5–11: $|J_y|$ Current Distribution, Elevation Difference Pattern

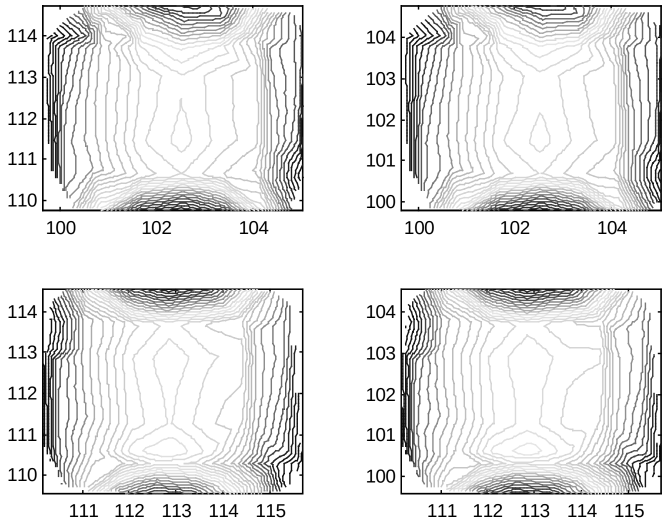

Figure 5–12: $|J_x|$ Current Distribution, Sum Pattern

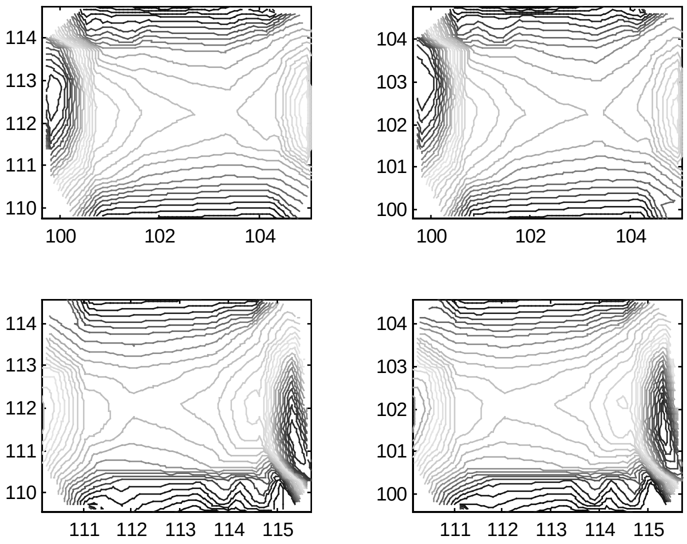

Figure 5–13: |J$_y$| Current Distribution, Sum Pattern

The current distributions on the four microstrip patch antennas, for the different monopulse excitations, are shown in *Figures 5–8* through *5–13*. The *x* and *y* coordinates in all plots are in *mm*. The peaks in the |J_x| distributions occur on the minimum and maximum *y*-boundaries of each patch, and at the center *x*-coordinate of each patch for all pattern excitations. For the |J_y| distributions, the peaks occur at either the minimum or maximum *x*-coordinates and the center *y*-coordinate of each patch. The exact location of the peaks, however, is a function of the excitation. For the azimuthal difference pattern, since the null is in the *yz*-plane (see *Figure 5–3*), the peaks occurred at opposite sides of this plane. Thus, for the microstrip patches on the left-hand side, the peaks are on the left-hand side of the patches. The opposite is true for the right-hand side patches. While the magnitude of the peaks is comparable, they are 180^{o} out of phase, creating the null in the azimuthal plane.

For the elevation plane, in addition to the peaks noted for the azimuthal difference case, smaller peaks occurred on the inner edges of the patches. This serves to diminish the symmetry of the radiated fields about the *yz*-plane, thereby eliminating the azimuthal null. The phase difference between the *x*-directed peaks produce the null in the elevation plane (*xz*).

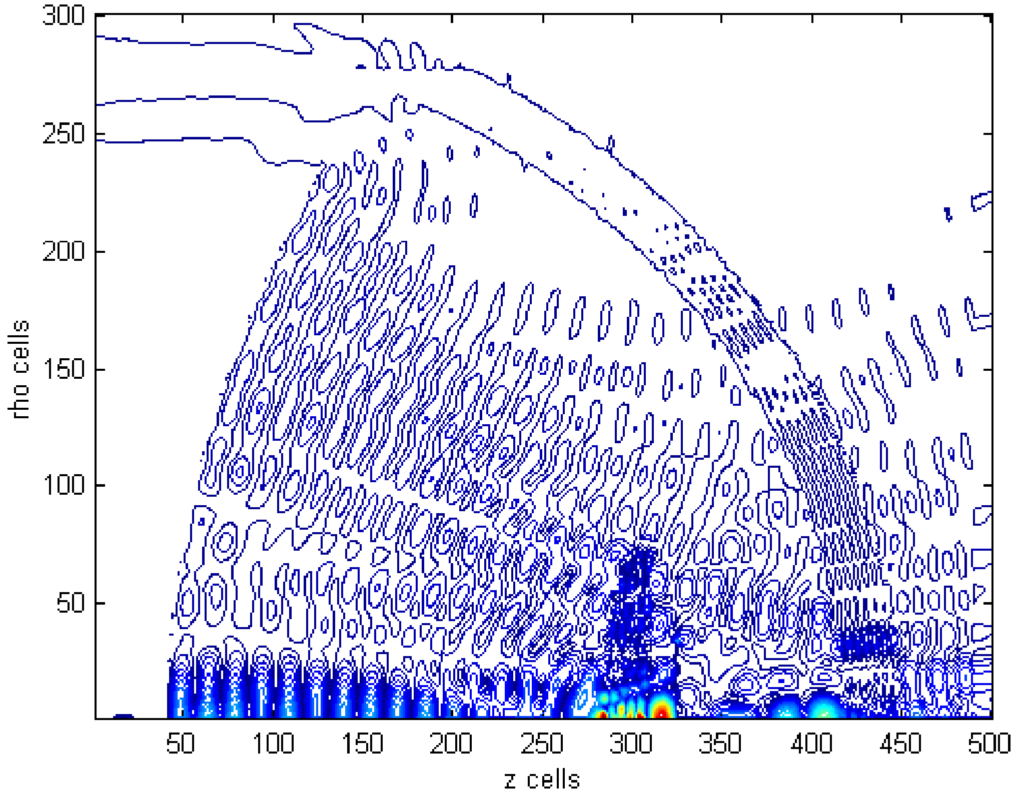

Figure 5–14: E_ρ *vs*. ρ & z cells, Reflector Antenna System

Finally, in the sum pattern current distributions, the current peaks in the *y* direction occur on the left-hand side of the upper patches, while they occur on the right-hand side of the lower patches. This serves to eliminate symmetry in both planes and still produce an LCP radiated wave.

A plot of the ρ-polarized electric fields being focused by the main reflector of the antenna system is shown in *Figure 5–14*. This plot shows the ρ-polarized field distribution with a radome surrounding the entire system. Also visible is a dielectric secondary reflector installed between the main reflector and the feed.

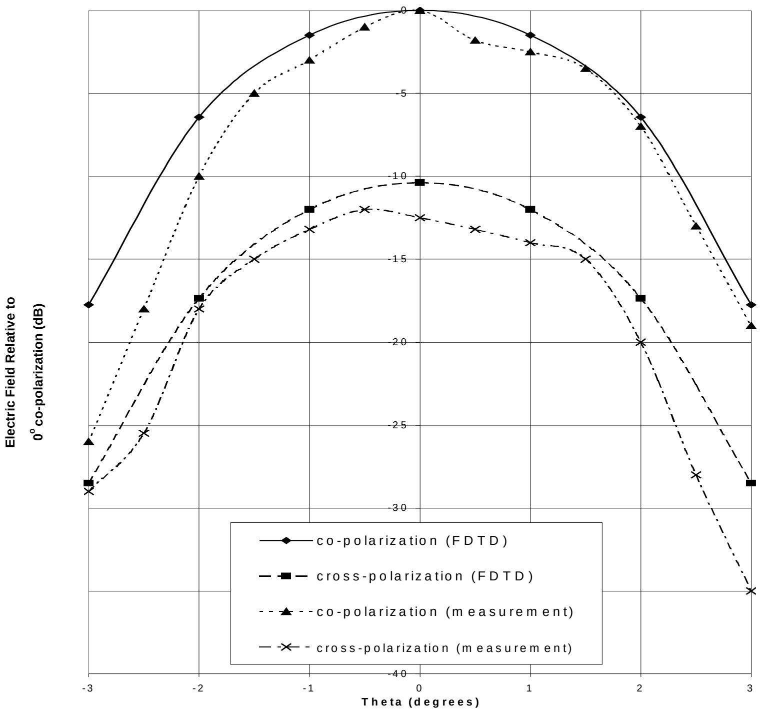

Figure 5–15: Comparison Between Simulated and Measured Data

The surface of the feed dielectric is located at *z*-cell 325. The secondary reflector serves to focus the fields onto the feed, which is not positioned at the focal point of the main reflector; hence, the sharp field peak at the feed position.

Finally, the gain of the system – using the above reported data combined through equations (5.36) to (5.39) – is computed. The curves in *Figure 5–15* are ratios *(dB)* of the far-zone electric fields, for various incidence angles, to the co-polarized far-zone electric field at 0^{o} incidence. The figure compares the simulated and measured results and the two are seen to be in fairly good agreement. The asymmetry in the measured results can be attributed to either measurement error or slight asymmetrical characteristics of the actual antenna system.

5.9 Summary

This chapter has presented a technique for the analysis of a large reflector antenna system with partial symmetry about its axis of rotation. Through application of the Surface Equivalence Principle, the geometry is made circularly symmetric, but with an asymmetric source. Use of the Reciprocity Theorem eliminates the asymmetric source, thus creating a completely circularly symmetric problem. This allows the simulation of the resulting geometry in an equivalent 2-D model, thereby substantially reducing computational resource requirements. Only 0.33% of the total number of cells required in the full 3-D model is simulated (see *Figure 5–14*).

The chapter describes the Reciprocity Approach to pattern computation for this particular geometry. Plots of the current distribution on the source microstrip patches and the electric field distribution on the dielectric feed of the reflector antenna system in response to plane wave excitation are also presented. Finally, radiation patterns generated by the proposed method are compared to actual test data and are found to be in good agreement. Thus, substantial computational savings are realized without sacrificing calculation accuracy.

Chapter 6

ANALYSIS OF A LARGE REFLECTOR ANTENNA SYSTEM - TILTED RADOME CONFIGURATION

This chapter describes an analysis of the same reflector antenna system considered in Chapter 5, however, for an inhomogeneous radome, which is tilted with respect to the remainder of the antenna system. This chapter presents an efficient method to solve this large body scattering problem *viz*., a paraboloid reflector antenna system, with only partial circular symmetry. The asymmetry in the system is introduced by two factors, *viz.*, the microstrip feed and an inhomogeneous radome. The chapter presents a novel approach, based on the Equivalence and Reciprocity Principles, and the “equivalent” aperture theory, to overcome the asymmetry problem and still take advantage of the circular symmetry of the large paraboloid of revolution. The technique thereby enables substantial computational efficiencies by analyzing the majority of the 3-D computational domain in an effective 2-D simulation, with the remainder being analyzed using a 3-D algorithm.

6.1 Problem Geometry

As mentioned above, the problem geometry is closely related to that considered in Chapter 5. The additional asymmetry considered here is due to the tilt of the radome structure relative to the remainder of the antenna system as shown in *Figure 6–1*:

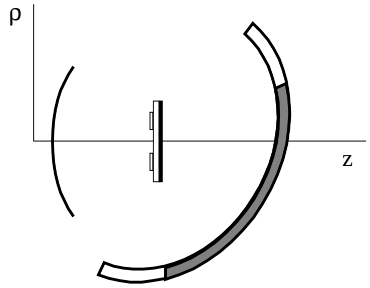

Figure 6–1: Tilted Radome Configuration

6.2 Method

The purpose of the proposed technique is to efficiently compute the radiation pattern of a large antenna system with partial circular symmetry. To avoid a 3-D simulation of the entire structure, the chapter presents two techniques which exploit the circular symmetry of the problem geometry to reduce the number of dimensions required by the simulation from three to two for a majority of the problem space. The Equivalence and Reciprocity Principles are used as in [9] and as described in Sec. 5.2 to overcome the first asymmetry caused by the feed structure. The second asymmetry, introduced by the inhomogeneous radome, is handled by applying the "equivalent aperture" theory to divide the problem into 2-D (majority of the simulation domain) and 3-D analyses prior to use of the aforementioned principles for the computation of the radiation pattern. The Finite Difference Time Domain (FDTD) [16] method is used to both construct the "equivalent aperture" (2-D FDTD) and propagate these aperture fields in a 3-D FDTD simulation whose results are then used by the Reciprocity Theorem to construct the pattern (see Sec. 5.2).

The 2½-D and 3-D FDTD simulation regions were truncated by a first-order Mür [23] and a 6-layer Perfectly Matched Layer (PML) [24] absorbing boundary condition, respectively.

6.2.1 Aperture Field Construction

When the radome is tilted at an angle with respect to the axis of the reflector system, as in *Figure 6–1*, an additional asymmetry is introduced into the geometry. To address this problem, the hybrid field pattern is first projected onto a plane perpendicular to the reflector structure (‘p’ in *Figure 6–2*).

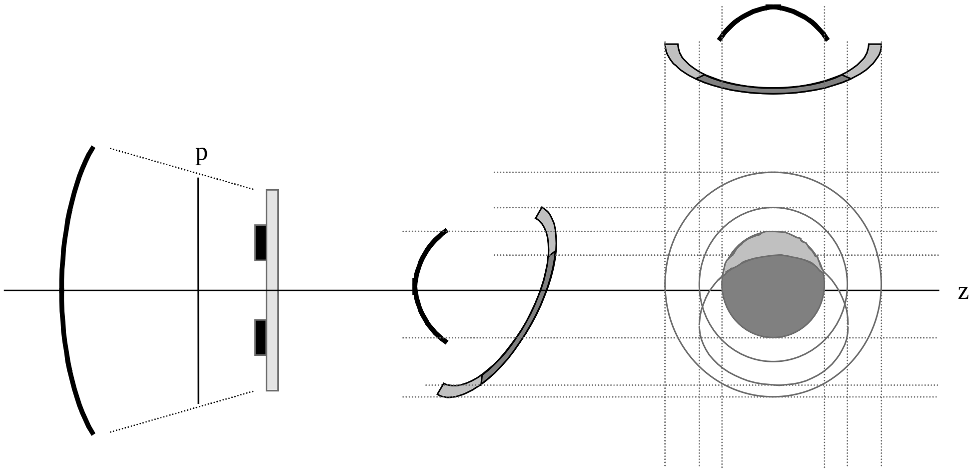

Figure 6–2: Tilted Radome and Projected Field Distribution

In this diagram, the darker region denotes where the incident fields penetrate the higher permittivity material (radome, $\varepsilon_r = 8.5$), while the lighter region indicates the corresponding region illuminated by the fields that penetrate the lower permittivity material (skirt, $\varepsilon_r = 4.2$).

The fields within these regions are obtained by analyzing the "normal" configuration (*Figure 5-1* of Chapter 5) using a 2½-D FDTD simulation (since the geometry has been made circularly symmetric by the Surface Equivalence Principle, as described in Sec. 5.2 above) with the entire radome consisting of first the higher permittivity material ($\varepsilon_r = 8.5$), then the lower permittivity material ($\varepsilon_r = 4.2$).

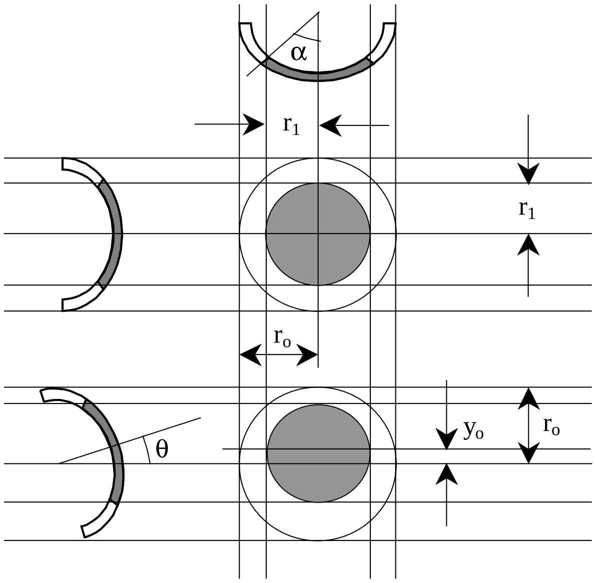

Figure 6–3: Tilted Radome and Projected Field Distribution, with Parameter Definitions

These fields are stored in a 2-D map (for both cases) at a z-position just inside the main reflector (between the main reflector and the feed, see *Figure 6–2*), then used to construct the "equivalent aperture" for the desired configuration and tilt angle. Note that the aperture fields are taken from those intercepted by the main reflector and focused onto the feed, as fields not captured by the main reflector have negligible effect on the fields produced on the feed structure.

Since the radome is circularly symmetric about the *z*-axis, it is sufficient to analyze the system with respect to one tilt angle, chosen to be in the elevation (*yz*) plane. A diagram of the system describing the parameters used for the aperture field construction is shown in *Figure 6–3*.

A circular region is formed when the reflector system is aligned with the radome structure (normal incidence, top drawing), while an elliptical pattern results when the radome structure is tilted relative to the reflector system (bottom drawing) by an angle θ. The center of the ellipse (or circle, in the normal case) relative to the center of the pattern, is determined by (see Appendix B for derivation)

$$y_o = r_o \sin\theta \cos\alpha \qquad (\ 6.1\ )$$

which is the center point between the top and bottom edges of where the radome material begins. The angle α is the angular displacement of the radome material and θ is the tilt angle of the radome structure with respect to the reflector system. Since the system is tilted in the elevation plane only, the major axis of the ellipse remains fixed at a length of r_1 (see *Figure 6–3*). The minor axis is calculated by the formula $b = r_1 \cos\theta$ (also derived in Appendix B). With all of the parameters known, the equation of the ellipse can then be written as

$$\left(\frac{x}{a}\right)^2 + \left(\frac{y}{b}\right)^2 = 1 \qquad (6.2)$$

in which $a = r_1$.

A condition which must be checked to obtain the correct aperture pattern is when $\theta - \alpha \leq -90^o$ or $\theta + \alpha \geq 90^o$. At these tilt angles, the bottom (top) edge of the ellipse begins to rise above (sink below) the top (bottom) edge of the radome structure. The condition of $\theta - \alpha = -90^o$ is illustrated in *Figure 6–4*:

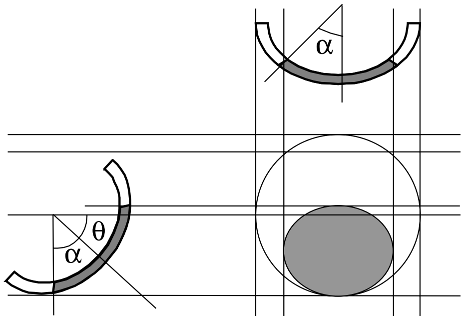

Figure 6–4: Tilted Radome: θ – α = -90°

To correct the elliptical pattern for angles beyond these special conditions ($\theta - \alpha \leq -90^o$ or $\theta + \alpha \geq 90^o$), the minor axis has been defined as two separate parameters, a lower and an upper length. When the condition is detected or exceeded, the lower (upper) minor axis is defined as the difference between r_o and the height of the center of the ellipse (6.1) for the $\theta - \alpha \leq -90^o$ ($\theta + \alpha \geq 90^o$) case. The upper (lower) minor axis remains the same ($b = r_1 \cos\theta$). To illustrate the effect of this correction, a drawing of the pattern for $\theta = -90^o$ is shown in *Figure 6–5* in which the upper minor axis is zero.

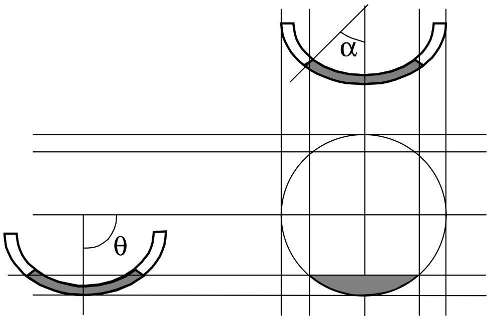

Figure 6–5: Tilted Radome: θ = -90^o

Once the distribution has been determined in the manner described above, it must be projected onto the radiating aperture of the reflector system. An example is shown in *Figure 6–6*:

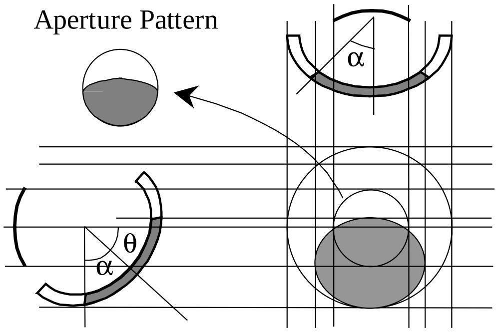

Figure 6–6: Projection of distribution onto Radiating Aperture

The upper left drawing in *Figure 6–6* shows the resulting aperture distribution projected onto the main reflector. The size of this aperture field distribution must then be adjusted (see *Figure 6–2*) based on the distance separating the aperture and the main reflector (full-size if the aperture is located at the main reflector and zero area if located at the focal point of the main reflector). The next step is to use this distribution as an input source for a 3-D FDTD simulation to propagate the fields onto the surface of the feed dielectric substrate. These fields are subsequently used to calculate the far-zone fields in accordance with the procedure described in Sec. 5.2.

6.2.2 3-D FDTD Simulation

To compute the radiation pattern for the reflector antenna system, the fields on the surface of the dielectric substrate are determined. These fields are then used in the Reciprocity Theorem, described in Sec. 5.2, to calculate the far-zone fields. Because the aperture distribution, determined from the procedure described in the last section, lacks circular symmetry, a 3-D FDTD algorithm is needed to determine the fields produced on the surface of the feed dielectric. The 3-D region simulated comprises 140 x 140 x 40 (784,000) cells, of which an 80 x 80 cell 2-D region, located at the dielectric substrate, is Fourier-transformed into the frequency domain. These resultant fields are then used in the Reciprocity Approach described in Sec. 5.2 to determine the far-zone radiation pattern for the entire reflector antenna system.

6.3 Numerical Results

To illustrate the procedure described in the last section, the field distribution in the focal region of a paraboloidal reflector antenna is calculated. The aperture fields for the radome are computed in two steps; first for the higher permittivity material ($\varepsilon_r = 8.5$), and then for the lower one ($\varepsilon_r = 4.2$). These distributions are shown in *Figures 6–7* and *6–8*, respectively. For this analysis, the tilt angle of the radome with respect to the reflector system was 30^o. The elliptical pattern projected onto the receiving aperture region and the resulting aperture pattern for this tilt angle are displayed in *Figures 6–9* and *6–10*. The fields in the upper portion of *Figure 6–10* correspond to those of *Figure 6–7* (fields through the higher permittivity material), while the lower portion corresponds to the fields in *Figure 6–8* (fields through the lower permittivity material). The regions of the combined pattern are defined in the center circle of *Figure 6–9*, which shows the aperture intercepting the incident radiation.

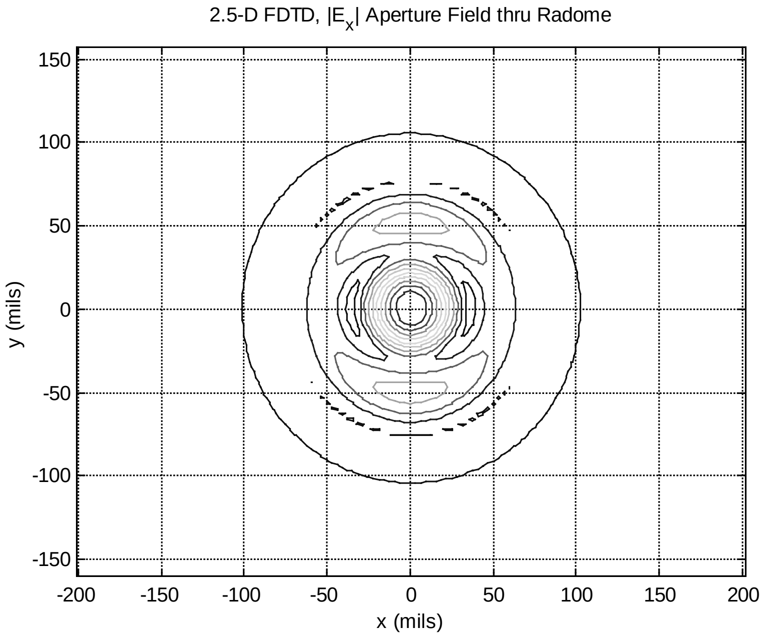

Figure 6–7: Aperture Field through Higher Permittivity Material ($\varepsilon_r = 8.5$)

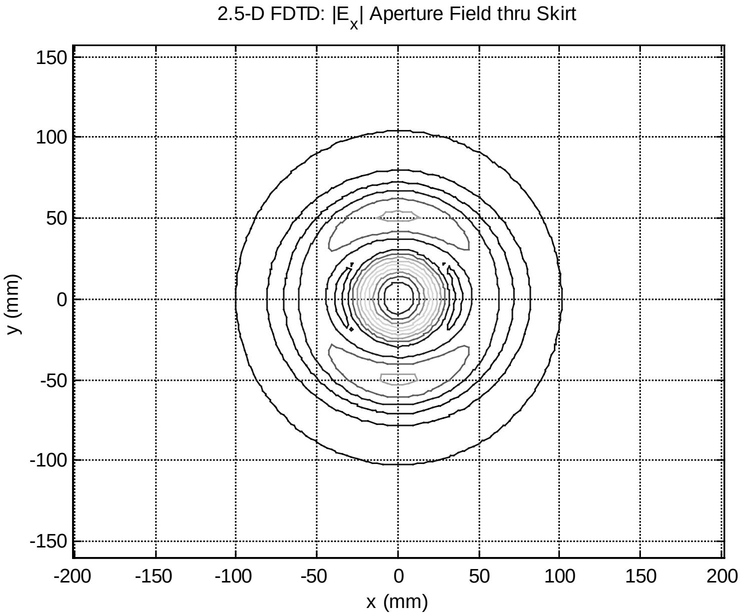

Figure 6–8: Aperture Field through Lower Permittivity Material ($\varepsilon_r = 4.2$)

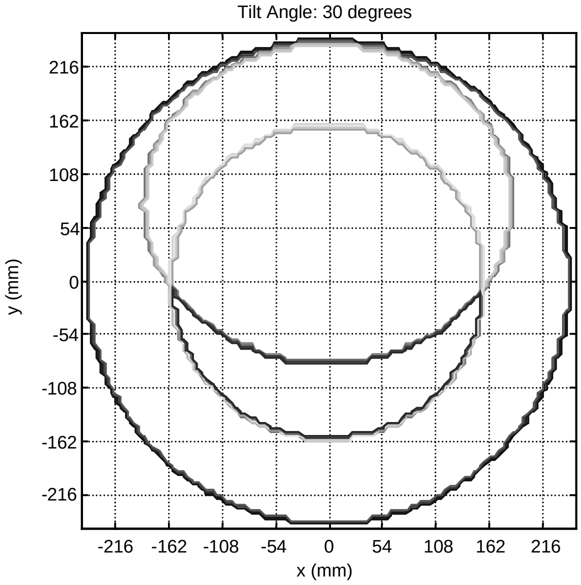

Figure 6–9: Elliptical Radome Pattern Projection onto Radiating Aperture

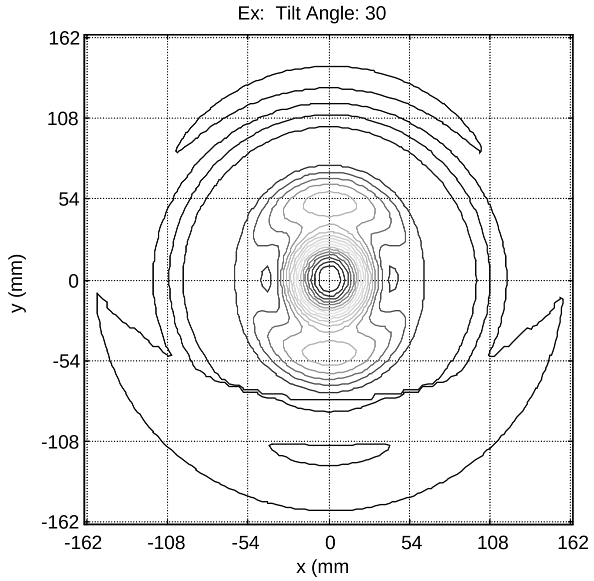

Figure 6–10: Resultant Aperture Field Pattern

As mentioned earlier, these aperture patterns are subsequently used as sources for the 3-D FDTD simulation to determine the fields on the surface of the feed dielectric. In accordance with the Reciprocity Procedure [equation (5.1)], a dot product of these fields and the surface currents on the four patches is evaluated to compute the far-zone electric field. Three different cases for the surface currents are considered, along with three different reflector system tilt angles.

The three current phasing configurations analyzed are the sum, azimuthal difference, and elevation difference patterns, which are created by controlling the relative phasing between excitation sources to the patches (as described in Sec. 5.1). The sum pattern has a peak in the normal direction (all patches fed in-phase relative to the circularly-polarized transmitted wave), while for the azimuthal and elevation difference patterns, a null exists along the *y*- and *x*-axes, respectively (see *Figure 6–11*).

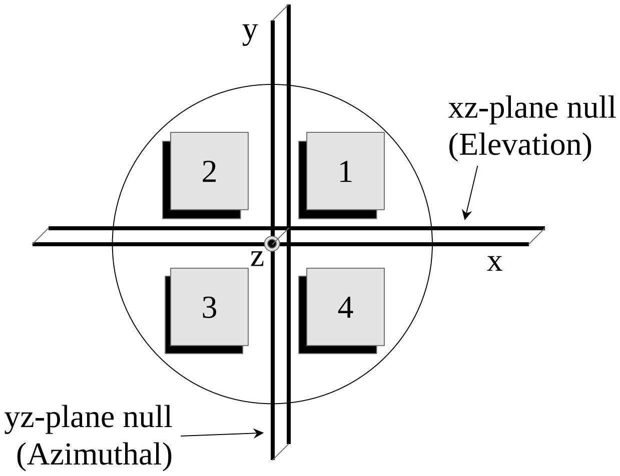

Figure 6–11: Patches on Feed Dielectric Surface

For difference patterns, the system is sensitive to differences across the null plane. The tilt angle analyzed was in the *yz*-plane with respect to the *z*-axis (out of *Figure 6–11*). As a result, the azimuthal difference pattern should be largely insensitive to the tilt angle, as differences in fields incident on patches 1 and 4 *vs.* those on patches 2 and 3 (along the null) should be small.

For the elevation difference pattern, a null exists along the *x*-axis. Therefore, this pattern should be sensitive to differences in the fields incident on patches 1 *vs.* 4 and 2 *vs.* 3. Since the tilt angle is in the *yz*-plane, fields of varying magnitude are intercepted by these pairs of patches due to the different radome materials as the tilt angle increases. This should lead to a larger change in radiated electric field magnitude.

The system was analyzed for tilt angles (θ in the *yz*-plane) of 30°, 40° and 50°. All far-zone field magnitudes were normalized to the sum pattern magnitude at boresight (0°). Both the co-polarization (left-hand circular polarization) and cross-polarization (right-hand circular polarization) radiation patterns were plotted for the sum, azimuthal difference and elevation difference pattern cases. The sum pattern is shown in *Figure 6–12*:

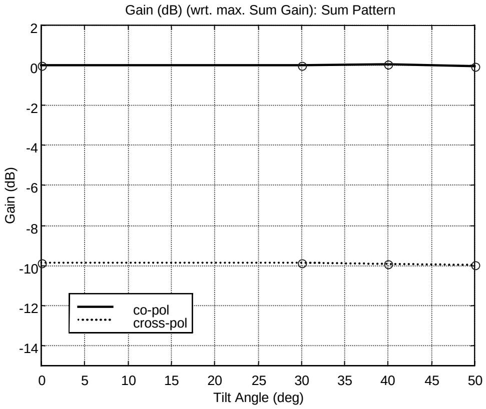

Figure 6–12: Sum Pattern (peak at boresight) *vs*. yz-plane Tilt Angle

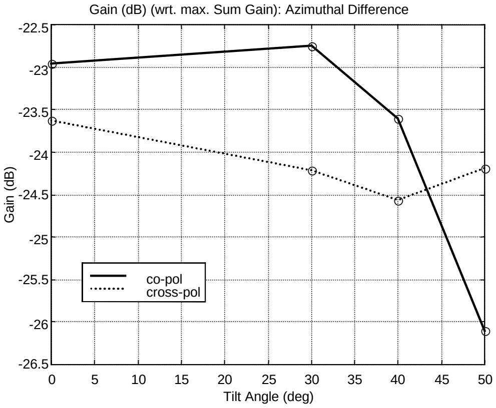

Figure 6–13: Azimuthal Difference Pattern (null along *y-axis*) *vs*. yz-plane Tilt Angle

Due to a broad peak appearing at boresight, the radiated field magnitude was insensitive to the tilt angle. This is the expected result as explained above. The field pattern for the azimuthal difference excitation is shown in *Figure 6–13*.

This pattern also showed only a slight change in radiated field magnitude due to the tilt angle being along the null. The magnitude was lower than that for the sum pattern due to the null. A difference of -3dB (70.7%) from the peak magnitude was noted at a tilt angle of 50°.

For the elevation difference pattern, a significant change in radiated field magnitude was noted due to the tilt angle being perpendicular to the null.

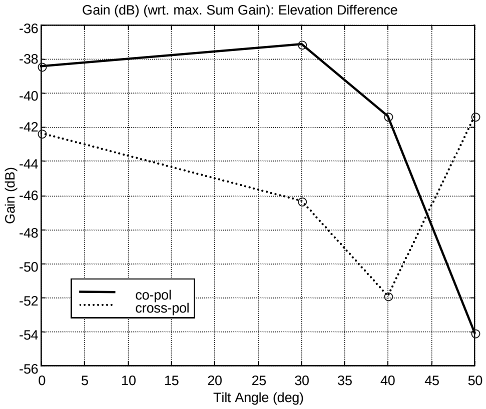

Figure 6–14: Elevation Difference Pattern (null along *x-axis*) *vs*. yz-plane Tilt Angle

This was as expected due to the relative positions of the null and tilt angle.

6.4 Summary

This chapter has presented an efficient method for determining radiation patterns for an electrically large reflector antenna system with a microstrip patch feed and a dielectric radome/skirt combination that has only partial circular-symmetry. The chapter shows how the existing symmetry of a large portion of the structure can be used to reduce the CPU time and memory requirements significantly. The Equivalence and Reciprocity Principles described in [58] and Sec. 5.2 are combined with the “equivalent” aperture approach to compute the radiation pattern of the reflector antenna system. Regarding computational requirements, for the above described problem geometry, only 0.65% of the total number of cells requires analysis, due to the reduction from three to two dimensions for a majority (98.4%) of the computational domain. The former figure (0.65%) is determined from a ratio of the number of 3-D cells included in both the 2½-D and 3-D FDTD simulations *vs*. the total number of 3-D cells. The latter figure (98.4%) is determined from the number of 2-D cells (ρz-plane) simulated in the 2½-D FDTD simulation *vs*. the total number of 2-D cells (ρz-plane). Thus, the application of the proposed method results in substantial savings in terms of both memory and run-time requirements. Numerical results for various current distributions are presented indicating the sensitivity of the system to tilt angles of the reflector antenna system with respect to the radome.

Chapter 7

CONCLUSIONS

This thesis has presented a general technique for the efficient analysis of aperture and microstrip conformal antennas. The technique exploits the homogeneity or the symmetry of the antenna structure to reduce computational resource requirements for calculating the radiation pattern. In particular, the Surface Equivalence Theorem is used to simplify the problem geometry, either by making the geometry completely homogeneous or circularly symmetric about an axis. The inhomogeneity or asymmetry is removed by replacing the radiating aperture with equivalent surface currents. By means of the Surface Equivalence Principle, the volume behind the radiating aperture – and within the mounting structure – may then be replaced by any material. Either perfectly conducting or dielectric material is chosen to produce a homogeneous or circularly symmetric structure.

The equivalent currents are determined by either the assumption or calculation of fields or currents that appear at the radiating aperture. Ideal field distributions were assumed for the slot configurations analyzed in Chapter 3, while current distributions were computed for the microstrip patch antennas by either the FDTD (Chapter 4) or MoM (Chapters 5 and 6) techniques.

The Reciprocity Theorem is then used to allow the computation of the radiation pattern via solution to a scattering problem. The fields and currents in the receiving and transmitting modes of the antenna system are related by the Reciprocity Theorem. In the receive mode, a dipole source is placed at the location of the desired far-zone field. This far-zone source thus produces plane waves in the vicinity of the structure under analysis. The tangential fields (either electric or magnetic) produced by the plane waves at the location of the radiating aperture are computed. The Reciprocity Theorem is then used to combine these tangential fields with the equivalent aperture currents determined earlier to compute the radiation patterns.

7.1 Efficiency Enhancement

For the microstrip patch antenna mounted on a large conducting structure, the proposed procedure takes advantage of the modeling capabilities of the FDTD method for the complex inhomogeneous region, which includes the patch antenna. It also exploits the efficiency of the MoM method in modeling homogeneous structures, which is created through application of the Surface Equivalence Principle. By using the new hybrid method, an extensive discretization of the entire geometry required by the FDTD method is avoided. Also, it is either very difficult or impossible to model the structure using the MoM method due to the complex structure in the region of the patch antenna. The hybrid technique used in this thesis avoids both of these difficulties and computes the radiation pattern efficiently and accurately. As mentioned in Chapter 1, less than 5% of the entire volume is modeled, compared to an FDTD-gridded simulation of the problem geometry.

For the reflector antenna system, the application of the hybrid method reduces the number of required dimensions from three to two for nearly all of the simulation domain. In this case, the MoM technique is used to compute the electric currents generated on microstrip patch antennas by a feed network. By replacing these patches with the currents

(Surface Equivalence Principle), the geometry is made circularly symmetric. However, due to the asymmetric currents, a 3-D simulation would still be necessary. By using the Reciprocity Theorem and operating the system in the receive mode, the fields produced at all points on the feed dielectric can be computed through a 2-D FDTD simulation, as the structure has been made circularly symmetric. While the fields are available at all locations on the dielectric substrate, only the fields at the position of the microstrip patch antennas are required for the pattern computation using the Reciprocity Approach. By reducing the number of dimensions from three to two for most of the simulation volume, less than 3% of the discretized volume is simulated. This figure is derived from the case where the entire simulation domain is discretized into 3-D FDTD cells.

The same reflector antenna system is also analyzed for a two-material radome tilted with respect to the remainder of the system. An “equivalent aperture” is constructed at a location between the main reflector and the feed antenna. The aperture is composed of fields at the aperture location, which have penetrated through one of the two materials comprising the radome. The projection of the radome structure onto the aperture of the main reflector determines which field is used at each location on the equivalent aperture. Although a 3-D FDTD simulation is required from this point, computational savings still exceed 99% (see Sec. 6.3).

7.2 Accuracy of the Method

The accuracy of the method has been verified for the slot configurations analyzed in Chapter 3. For slots mounted on infinite-length conducting cylinders, direct analytical relations exist for the pattern computations. These matched exactly with the Reciprocity-based patterns, thus validating the approach. For the cavity-backed microstrip patch antenna mounted on a conducting cylinder (Chapter 4), the effects of the cavity edges were noted. Radiating aperture fields polarized normal to the cavity edge radiate more energy in the shadow region compared to fields tangential to the edge. Patterns computed for this case were compared to those computed for a closely related geometry in which the dielectric cavity is extended throughout the conducting cylinder. In this way, cavity edge effects were studied.

For the normal case, patterns computed using the two geometries compared well. The pattern for the associated geometry had slightly deeper nulls produced by the stronger standing wave effects encountered in the cavity-free geometry. For the tangential case, the patterns did not compare well. This was due to the greater attenuation of the creeping waves emanating from the aperture by the cavity edge.

For the reflector antenna system, the accuracy of the hybrid method used in this thesis was verified against actual test data. Both the co- and cross-polarization patterns were computed and compared. Due to the narrow beamwidth of reflector antennas, the pattern computation extended to only 3^{o} in either direction away from boresight. Asymmetries in the measured pattern were most likely due to slight asymmetries in the structure of the actual antenna system. Despite these complications, the measured and computed patterns compared well. This further validated the accuracy of the Reciprocity Approach to pattern computation.

For the tilted radome analysis, simulations for all three feed network phasings had the correct response as the tilt angle was increased in the elevation plane. Both the sum and azimuthal difference patterns showed negligible changes in far-field magnitude, while substantial changes occurred for the elevation difference pattern. While test data for comparison purposes does not exist, the trend of the plots in all cases is correct.

7.3 Suggestions for Further Research

To extend the capabilities of the hybrid method used in this thesis, the conformal FDTD method could be generalized to allow analysis of either singly or doubly curved microstrip patches. This additional feature would allow determination of the radius of curvature relative to the patch size where the flat approximation to a curved patch antenna is no longer valid. Also, more generally shaped patch antennas could be modeled.

For the reflector antenna analysis, the replacement of the Mur absorbing boundary condition with PML would improve the accuracy of the model and eliminate the need for a relatively large number of cells between all antenna structures and the limits of the simulation domain. Also, a true plane wave could be used, thereby further improving the accuracy of the model.

BIBLIOGRAPHY

1. G. A. Deschamps, “Microstrip Microwave Antennas,” presented at the 3rd USAF Symp. on Antennas, 1953.

2. H. Gutton and G. Baissinot, “Flat Aerial for Ultra high Frequencies,” French Patent No. 703113, 1955.

3. R. E. Munson, “Conformal Microstrip Antennas and Microstrip Phased Arrays,” *IEEE Trans. Antennas Propagat.*, Vol. AP-22, no. 1, pp. 74-77, Jan. 1974.

4. J. Q. Howell, “Microstrip Antennas,” *IEEE Trans. Antennas Propagat.*, Vol. AP-23, No. 1, pp. 90-93, Jan. 1975.

5. K. S. Kunz and R. J. Luebbers, *The Finite Difference Time Domain Method for Electromagnetics*, CRC Press, Inc., Boca Raton, FL, 1993.

6. R. F. Harrington, *Field Computation by Moment Methods*, Macmillan, New York, NY, 1967.

7. R. F. Harrington, *Time-Harmonic Electromagnetic Fields*, McGraw-Hill, New York, NY, 1961.

8. D. Arakaki, D. H. Werner, and R. Mittra, “A Technique for Analyzing Radiation from Conformal Antennas Mounted on Arbitrarily-Shaped Conducting Bodies,” submitted to *Proceedings of the 16th Annual Review of Progress in Applied Computational Electromagnetics (ACES)*, Naval Postgraduate School, Monterey, CA, March 20-25, 2000.

9. W. Yu, D. Arakaki, and R. Mittra, “On the Solution of a Class of Large Body Problems with Full or Partial Circular Symmetry by Using the Finite Difference Time Domain (FDTD) Method,” submitted to *IEEE Trans. Antennas Propagat*.

10. D. Arakaki, W. Yu, and R. Mittra, “On the Solution of a Class of Large Body Problems with Partial Circular Symmetry (Multiple Asymmetries) by Using a Hybrid Dimensional Finite Difference Time Domain (FDTD) Method,” submitted to *IEEE Trans. Antennas Propagat*.

11. D. Arakaki, W. Yu, and R. Mittra, “An Efficient Finite Difference Time Domain (FDTD) Technique For Modeling a Reflector Antenna System with Partial Circu-

lar Symmetry," *IEEE AP-S International Symposium*, Orlando, FL, July 11-16, 1999, pp. 2344-2347.

12. W. Yu, R. Mittra, D. Arakaki, and D. H. Werner, "A Robust Conformal Finite Difference Time Domain (FDTD) Technique for Modeling Perfectly Conducting Objects," submitted to *Proceedings of the 16th Annual Review of Progress in Applied Computational Electromagnetics (ACES)*, Naval Postgraduate School, Monterey, CA, March 20-25, 2000.

13. W. Yu and R. Mittra, "Application of the Conformal FDTD Approach to Planar Microwave Circuits," submitted to *IEEE Microwave Guided Wave Lett*.

14. W. Yu and R. Mittra, "Modeling Planar Annular Microwave Resonators Using the Conformal Finite-Difference Time-Domain (FDTD) Approach," submitted to *IEEE Trans. Microwave Theory Tech*.

15. W. Yu and R. Mittra, "Applications of the Conformal Finite-Difference Time-Domain (FDTD) Approach to Planar Microwave Circuits," submitted to *IEEE Trans. Microwave Theory Tech*.

16. K. S. Yee, "Numerical Solution of Initial Boundary Value Problems Involving Maxwell's Equations in Isotropic Media," *IEEE Trans. Antennas Propagat*., Vol. AP-14, No. 3, May 1966, pp. 302-307.

17. A. Taflove, *Computational Electrodynamics – The Finite-Difference Time-Domain Method*, Artech House, Boston, MA, 1995.

18. A. F. Peterson, S. L. Ray, and R. Mittra, *Computational Methods for Electromagnetics*, IEEE Press, Inc., New York, NY, 1998.

19. M. J. Maron, *Numerical Analysis: A Practical Approach*, Macmillan Publishing Company, New York, NY, 1987.

20. D. F. Kelley and R. J. Luebbers, "Piecewise Linear Recursive Convolution for Dispersive Media Using FDTD," *IEEE Trans. Antennas Propagat*., Vol. 44, No. 6, June 1996, pp. 792-797.

21. E. Isaacson and H. B. Keller, *Analysis of Numerical Methods*, John Wiley & Sons, New York, NY, 1967.

22. A. Taflove and M. E. Brodwin, "Numerical Solution of Steady-State Electromagnetic Scattering Problems Using the Time-Dependent Maxwell's Equations," *IEEE Trans. Microwave Theory Tech*., Vol. MTT-23, Aug. 1975, pp. 623-630.

23. G. Mur, “Absorbing Boundary Conditions for the Finite Difference Approximation of the Time-Domain Electromagnetic Field Equations,” *IEEE Trans. Electromagn. Compat.*, Vol EMC-23, Nov. 1981, pp. 377-382.

24. J. P. Berenger, “A Perfectly Matched Layer for the Absorption of Electromagnetic Waves,” *J. Computational Phys.*, Vol. 114, 1994, pp. 185-200.

25. D. S. Katz, E. T. Thiele, and A. Taflove, “Validation and Extension to Three Dimensions of the Berenger PML Absorbing Boundary Condition for FD-TD Meshes,” *IEEE Microwave Guided Wave Lett.*, Vol. 4, No. 8, Aug. 1994, pp. 268-270.

26. Z. P. Liao, H. L. Wong, B. P. Yang, and Y. F. Yuan, “A Transmitting Boundary for Transient Wave Analysis,” *Scientia Sinica (Series A)*, Oct. 1984, pp. 1063-1076.

27. S. D. Gedney, “An Anisotropic Perfectly Matched Layer-Absorbing Medium for the Truncation of FDTD Lattices,” *IEEE Trans. Antennas Propagat.*, Vol. 44, No. 12, Dec. 1996, pp. 1630-1639.

28. S. Dey, R. Mittra, and S. Chebolu, A Locally Conformal Finite-Difference Time-Domain (FDTD) Algorithm For Modeling Three-Dimensional Perfectly Conducting Objects,” *IEEE Microwave Guided Wave Lett.*, Vol. 7, No. 9, Sept. 1997, pp. 273-275.

29. R. F. Harrington, “Matrix Methods for Field Problems,” *Proc. IEEE*, Vol. 55, No.2, Feb. 1967, pp. 136-149.

30. S. M. Rao, D. R. Wilton, and A. W. Glisson, “Electromagnetic Scattering by Surfaces of Arbitrary Shape,” *IEEE Trans. Antennas Propagat.*, Vol. AP-30, No. 3, May 1982, pp. 409-418.

31. E. Michielssen, “Electromagnetic Plane Wave Scattering from Periodically Loaded Cylinders and Doubly Periodic Slabs,” Ph.D. Dissertation, University of Illinois, Urbana-Champaign, IL, 1992.

32. C. A. Balanis, “*Advanced Engineering Electromagnetics*,” John Wiley & Sons, New York, NY, 1989.

33. C. A. Balanis, *Antenna Theory: Analysis and Design*, Second Edition, John Wiley & Sons, New York, NY, 1997.

34. A. W. Glisson and D. R. Wilton, “Simple and Efficient Numerical Methods for Problems of Electromagnetic Radiation and Scattering from Surfaces,” *IEEE Trans. Antennas Propagat.*, Vol. AP-28, No. 5, Sept. 1980, pp. 593-603.

35. E. Anderson, Z. Bai, C. Bischof, S. Blackford, J. Demmel, J. Dongarra, J. Du Croz, A. Greenbaum, S. Hammarling, A. McKenney, D. Sorensen, *LAPACK User's Guide*, Third Edition, Computer Based Learning Unit, University of Leeds, 1996.

36. International Business Machines Corporation, *Engineering and Scientific Subroutine Library (ESSL) for AIX*, Guide and Reference, First Edition, Dec. 1997.

37. IE3D, Release 4, Zeland Software, Inc., Fremont, CA.

38. C. Huygens, *Traite de la Lumiere*, Leyeden, 1690. Translated into English by S. P. Thompson, London, 1912, reprinted by The University of Chicago Press.

39. S. A. Schelkunoff, "Some Equivalence Theorems of Electromagnetics and Their Application to Radiation Problems," *Bell System Tech. J.*, Vol. 15, 1936, pp. 92-112.

40. A. E. H. Love, "The Integration of the Equations of Propagation of Electric Waves," *Phil. Trans. Roy. Soc. London, Ser. A*, Vol. 197, 1901, pp. 1-45.

41. J. C. Cheng, N. I. Nihad, and L. P. B. Katehi, "Theoretical Modeling of Cavity-Backed Patch Antennas Using a Hybrid Technique," *IEEE Trans. Antennas Propagat.*, Vol. 43, No. 9, Sept. 1995, pp. 1003-1013.

42. X. Yuan, D. R. Lynch, and J. W. Strohbehn, "Coupling of Finite Element and Moment Methods for Electromagnetic Scattering from Inhomogeneous Objects," *IEEE Trans. Antennas Propagat.*, Vol. 38, No. 3, Mar. 1990, pp. 386-393.

43. J. H. Richmond, "TE-Wave Scattering by a Dielectric Cylinder of Arbitrary Cros Section Shape," *IEEE Trans. Antennas Propagat.*, Vol. AP-14, No. 4, July 1966, pp. 460-464.

44. K. K. Mei, "Unimoment Method of Solving Antenna and Scattering Problems," *IEEE Trans. Antennas Propagat.*, Vol. AP-22, No. 6, Nov. 1974, pp. 760-766.

45. S. K. Chang and K. K. Mei, "Application of the Unimoment Method to Electromagnetic Scattering of Dielectric Cylinders," *IEEE Trans. Antennas Propagat.*, Vol. AP-24, No. 1, Jan. 1976, pp. 35-42.

46. D. J. Hoppe, L. W. Epp, and J. F. Lee, "A Hybrid Symmetric FEM/MoM Formulation Applied to Scattering by Inhomogeneous Bodies of Revolution," *IEEE Trans. Antennas Propagat.*, Vol. 42, No. 6, June 1994, pp. 798-805.

47. D. Jankovic, M. LaBelle, D. C. Chang, J. M. Dunn, and R. C. Booton, "A Hybrid Method for the Solution of Scattering from Inhomogeneous Dielectric Cylinders

of Arbitrary Shape," *IEEE Trans. Antennas Propagat*., Vol. 42, No. 9, Sept. 1994, pp. 1215-1222.

48. D. Sun, J. Manges, X. Yuan, and Z. Cendes, "Spurious Modes in Finite-Element Methods," *IEEE Trans. Antennas Propagat. Magazine*, Vol. 37, No. 5, Oct. 1995, pp. 12-25.

49. J. M. Jin and J. L. Volakis, "A Hybrid Finite Element Method for Scattering and Radiation by Microstrip Patch Antennas and Arrays Residing in a Cavity," *IEEE Trans. Antennas Propagat*., Vol. 39, No. 11, Nov. 1991, pp. 1598-1604.

50. J. Gong, J. L. Volakis, A. C. Woo, and H. T. G. Wang, "A Hybrid Finite Element-Boundary Integral Method for the Analysis of Cavity-Backed Antennas of Arbitrary Shape," *IEEE Trans. Antennas Propagat*., Vol. 42, No. 9, Sept. 1994, pp. 1233-1242.

51. L. C. Kempel and J. L. Volakis, "Scattering by Cavity-Backed Antennas on a Circular Cylinder," *IEEE Trans. Antennas Propagat*., Vol. 42, No. 9, Sept. 1994, pp. 1268-1279.

52. T. Ozdemir, M. W. Nurnberger, J. L. Volakis, R. Kipp, and J. Berrie, "A Hybridization of Finite-Element and High-Frequency Methods for Pattern Prediction for Antennas on Aircraft Structures," *IEEE Trans. Antennas Propagat*. *Magazine*, Vol. 38, No. 3, June 1996, pp. 28-38.

53. G. A. Thiele and T. H. Newhouse, "A Hybrid Technique for Combining Moment Methods with the Geometrical Theory of Diffraction," *IEEE Trans. Antennas Propagat*., Vol. AP-23, No. 1, Jan. 1975, pp. 62-69.

54. U. Jakobus and F. M. Landstorfer, "Improved PO-MM Hybrid Formulation for Scattering from Three-Dimensional Perfectly Conducting Bodies of Arbitrary Shape," *IEEE Trans. Antennas Propagat*., Vol. 43, No. 2, Feb. 1995, pp. 162-169.

55. T. T. Chia, R. J. Burkholder, and R. Lee, "The Application of FDTD in Hybrid Methods for Cavity Scattering Analysis," *IEEE Trans. Antennas Propagat*., Vol. 43, No. 10, Oct. 1995, pp. 1082-1090.

56. G. Cerri, P. Russo, A. Schiavoni, and G. Tribellini, "MoM-FDTD Hybrid Technique for Analyzing Scattering Problems," *Electronics Letters*, Vol. 34, No. 5, Mar. 1998, pp. 438-440.

57. Ensemble, Version 4.0, Boulder Microwave Technologies, Inc., Boulder CO.

58. R. Mittra, S. Dey, S. Chakravarty, and N. V. Veremey, "Reciprocity Approach to Pattern Computation of a Microstrip Antenna Operating in a Complex Environ-

ment," *IEEE AP-S International Symposium*, Atlanta, GA, June 21-26, 1998, pp. 1138-1141.

59. D. H. Werner, G. D. Mouyis, and R. Mittra, "A Reciprocity Approach for Determining Radiation Patterns of Patch Antennas on Circularly-Cylindrical Platforms," *IEEE AP-S International Symposium*, Atlanta, GA, June 21-26, 1998, pp. 1582-1585.

60. D. H. Werner, G. D. Mouyis, R. Mittra, and J. S. Zmyslo, "A Reciprocity Approach for Calculating Radiation Patterns of Arbitrarily Shaped Patch Antennas Mounted on Circularly-Cylindrical Platforms," *Proceedings of the 15th Annual Review of Progress in Applied Computational Electromagnetics (ACES)*, Naval Postgraduate School, Monterey, CA, March 15-20, 1999, pp. 508-515.

61. J. M. Jin, J. A. Berrie, R. Kipp, and S. W. Lee, "Calculation of Radiation Patterns of Microstrip Antennas on Cylindrical Bodies of Arbitrary Cross Section," *IEEE Trans. Antennas Propagat.*, Vol. 45, No. 1, Jan. 1997, pp. 126-132.

62. R. J. Allard, D. H. Werner, and J. A. Zmyslo, "A Domain-Decomposition Reciprocity Technique for the Analysis of Arbitrarily-Shaped Microstrip Antennas with Dielectric Substrates and Superstrates Mounted on Circularly-Cylindrical Platforms," submitted to *Proceedings of the 16th Annual Review of Progress in Applied Computational Electromagnetics (ACES)*, Naval Postgraduate School, Monterey, CA, March 20-25, 2000.

63. PATRAN, Version 8.5, MSC Software Corporation, Costa Mesa, CA.

64. Y. Chen and R. Mittra, "Finite-Difference Time-Domain Algorithm for Solving Maxwell's Equations in Rotationally Symmetric Geometries," *IEEE Trans. Microwave Theory Tech.*, Vol. 44, June 1996, pp. 832-839.

65. N. Kaneda, B. Houshmand, and T. Itoh, "FDTD Analysis of Dielectric Resonators with Curved Surfaces," *IEEE Trans. Microwave Theory Tech.*, Vol. 45, Sept. 1997, pp. 1645-1649.

Appendix A

Aperture Surface Integral: Integrand H*M Equivalence to E*J

In Chapter 3, the surface integral of ***–H*M_s*** over the radiating aperture is required for the computation of the far-zone electric field. This appendix proves the equivalence of this quantity to an integral of ***E*J_s*** taken over the aperture for a surface of general shape.

It is known from Sec. 2.3 that the surface electric current ***J_s*** can be expressed in terms of the magnetic field discontinuity at the surface,

$$\mathbf{J}_S = \hat{n}\times\mathbf{H} \qquad (\text{ A.1 })$$

where $\hat{n}$ is the unit vector normal to the surface and ***H*** is the magnetic field at the surface, assuming it is zero below the surface (see *Figure* 2-9). Taking the cross-product of equation (A.1) with the surface normal yields

$$\hat{n}\times\mathbf{J}_S = \hat{n}\times(\hat{n}\times\mathbf{H}) = (\hat{n}\cdot\mathbf{H})\hat{n} - (\hat{n}\cdot\hat{n})\mathbf{H} \qquad (\text{ A.2 })$$

which uses the vector identity

$$\mathbf{a}\times(\mathbf{b}\times\mathbf{c}) = (\mathbf{a}\cdot\mathbf{c})\mathbf{b} - (\mathbf{a}\cdot\mathbf{b})\mathbf{c} \qquad (\text{ A.3 })$$

Equation (A.2) then becomes

$$\hat{n}\times\mathbf{J}_S = \hat{n}H_{norm} - \mathbf{H} \qquad (\text{ A.4 })$$

where H_{norm} is the component of ***H*** normal to the surface. Therefore, the equivalent magnetic field is given by

$$\mathbf{H} = -\hat{n}\times\mathbf{J}_S + \hat{n}H_{norm} \tag{A.5}$$

Also proven in Sec. 2.3 is the expression for the equivalent magnetic surface currents in terms of an electric field discontinuity

$$\mathbf{M}_S = -\hat{n}\times\mathbf{E} \tag{A.6}$$

where ***E*** is the electric field at the surface, assuming that it is zero below the surface. Therefore, the dot product ***H*M*** can be written as

$$\begin{aligned} \mathbf{H}\cdot\mathbf{M}_S &= \left(-\hat{n}\times\mathbf{J}_S + \hat{n}H_{norm}\right)\cdot\mathbf{M}_S \\ &= \left(-\hat{n}\times\mathbf{J}_S\right)\cdot\mathbf{M}_S \\ &= \left(-\hat{n}\times\mathbf{J}_S\right)\cdot\left(-\hat{n}\times\mathbf{E}\right) \\ &= \left(\hat{n}\times\mathbf{J}_S\right)\cdot\left(\hat{n}\times\mathbf{E}\right) \end{aligned} \tag{A.7}$$

The second line results from the fact that $\boldsymbol{M_S}$ is tangential to the surface. Using the vector identity

$$\mathbf{a}\cdot\left(\mathbf{b}\times\mathbf{c}\right) = \left(\mathbf{a}\times\mathbf{b}\right)\cdot\mathbf{c} \tag{A.8}$$

the last line of equation (A.7) can be rewritten as

$$\begin{aligned} \left(\hat{n}\times\mathbf{J}_S\right)\cdot\left(\hat{n}\times\mathbf{E}\right) &= \left[\left(\hat{n}\times\mathbf{J}_S\right)\times\hat{n}\right]\cdot\mathbf{E} \\ &= -\mathbf{E}\cdot\left[\hat{n}\times\left(\hat{n}\times\mathbf{J}_S\right)\right] \end{aligned} \tag{A.9}$$

Using equation (A.3) again, the above relation can be simplified to

$$\begin{aligned} -\mathbf{E}\cdot\left[\hat{n}\times\left(\hat{n}\times\mathbf{J}_S\right)\right] &= -\mathbf{E}\cdot\left[\left(\hat{n}\cdot\mathbf{J}_S\right)\hat{n} - \left(\hat{n}\cdot\hat{n}\right)\mathbf{J}_S\right] \\ &= \mathbf{E}\cdot\mathbf{J}_S \end{aligned} \tag{A.10}$$

since the surface electric current $\boldsymbol{J_S}$ is tangential to the surface. Thus, for an integral taken over a surface of general shape, the following identity holds

$$\int_S \mathbf{H} \cdot \mathbf{M}_S \, d\mathbf{S} = \int_S \mathbf{E} \cdot \mathbf{J}_S \, d\mathbf{S} \qquad (\text{A.11})$$

Appendix B

Derivation of Tilted Radome Parameters

The derivation of the various parameters used for the tilted radome analysis of Chapter 6 will be presented here. First, the parameters y_o and b mentioned in the chapter will be derived, followed by a discussion about the special conditions when the bottom (top) edge of the radome lift above (below) the upper (lower) edge.

To reiterate the problem, *Figure 6-3* is reproduced here.

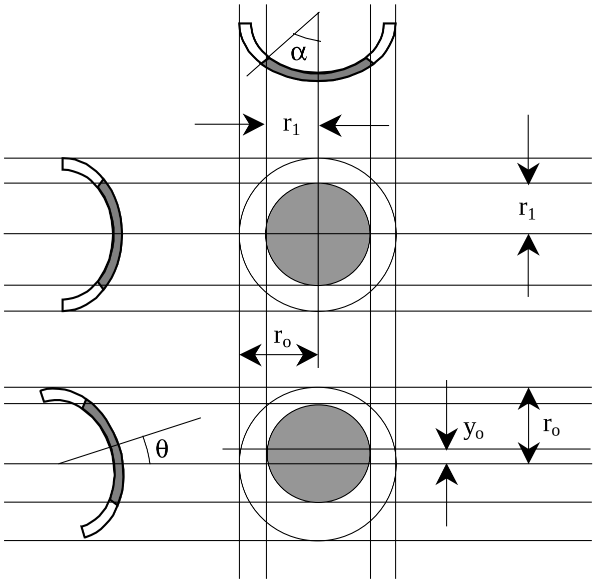

Figure B–1: Tilted Radome and Projected Field Distribution, with Parameter Definitions

Examining the lower left-hand side of *Figure B–1*,

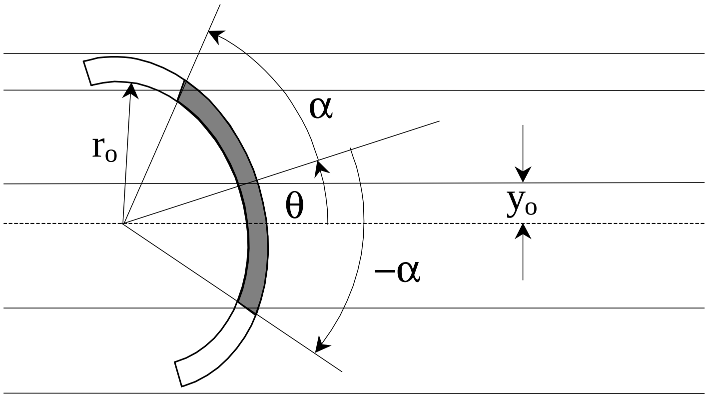

Figure B–2: Radome Projection onto Main Reflector

From *Figure B–2*, which defines the direction for positive angular displacement, the value for y_o can be found by averaging the sum of the y-projections of the radome above and below the centerline (dashed) of the above diagram. Thus,

$$y_o = \frac{1}{2}\left[r_o \sin(\theta + \alpha) + r_o \sin(\theta - \alpha)\right] \tag{B.1}$$

Using the trigonometric identity,

$$\sin\alpha\cos\beta = \frac{1}{2}\left[\sin(\alpha + \beta) + \sin(\alpha - \beta)\right] \tag{B.2}$$

equation (B.1) simplifies to

$$y_o = r_o \sin\theta\cos\alpha \tag{B.3}$$

The minor axis of the ellipse formed by the radome in *Figure B–1* above is the distance from the center of the ellipse to either the top or bottom edge. This can be found by subtracting y_o from the upper y-displacement as follows,

$$\begin{aligned} b &= r_o \sin(\theta+\alpha) - y_o \\ &= r_o \sin(\theta+\alpha) - \frac{1}{2}\left[r_o \sin(\theta+\alpha) + r_o \sin(\theta-\alpha)\right] \\ &= r_o \frac{1}{2}\left[\sin(\theta+\alpha) - \sin(\theta-\alpha)\right] \end{aligned} \qquad (\text{ B.4 })$$

which through another trigonometric identity,

$$\cos\alpha \sin\beta = \frac{1}{2}\left[\sin(\alpha + \beta) - \sin(\alpha - \beta)\right] \qquad (\text{ B.5 })$$

simplifies to

$$b = r_o \cos\theta \sin\alpha \qquad (\text{ B.6 })$$

But, from *Figure B–1*, $r_1 = r_o \sin\alpha$. Therefore,

$$b = r_1 \cos\theta \qquad (\text{ B.7 })$$

To accommodate the cases when $\theta - \alpha \leq -90^o$ or $\theta + \alpha \geq 90^o$, the pattern computation code defines two minor axes for the ellipse: upper and lower components (b_+ and b_-). For the former case,

$$\begin{aligned} b_+ &= r_1 \cos\theta \\ b_- &= \max(b_+, r_o + y_o) \end{aligned} \qquad (\text{ B.8 })$$

The lower minor axis takes into account that when $\theta - \alpha < -90^o$, the lower edge of the radome begins to rise above the bottom of the entire circle formed by the skirt/radome structure. Note that the upper minor axis b_+ becomes zero when $\theta = 90^o$ as shown in *Figure B–3*.

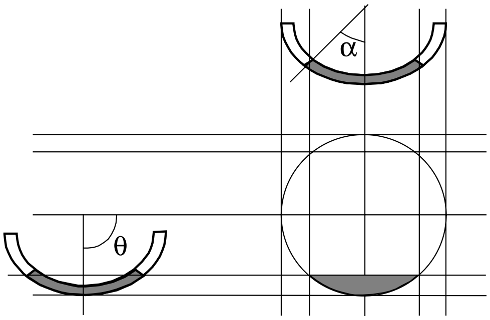

Figure B–3: Tilted Radome: θ = -90^o

For the latter case ($\theta + \alpha \geq 90^o$), the definitions for the upper and lower minor axes are transposed

$$\begin{aligned} b_+ &= \max(b_-, r_o - y_o) \\ b_- &= r_1 \cos\theta \end{aligned} \qquad \text{(B.9)}$$

A sign change is also necessary since $y_o > 0$ for $\theta > 0^o$. The case where $\theta = +90^o$ is accommodated in the same manner shown in *Figure B–3* for $\theta = -90^o$.

VITA

Dean Yasuo Arakaki was born in San Gabriel, CA on August 17, 1961. He graduated from Montebello High School, Montebello, CA in 1979, and enrolled in the electrical engineering program at California State Polytechnic University, Pomona in the fall of that year. He received the BSEE degree in June 1984, and worked as an engineer at several firms including TRW and Hughes Aircraft Company. From 1988 to 1993, he was employed as a power supply design engineer at Hughes and also pursued part-time graduate studies. He received the MBA and MSEE degrees from California State University, Long Beach in 1989 and 1992, respectively. After working at the General Electric Company (now Lockheed Martin) in Princeton, NJ from 1993 to 1994, he began graduate studies at the Pennsylvania State University in the fall of 1994. He has held both research and teaching assistantship positions within the Electrical Engineering Department and the Materials Research and Applied Research Laboratories at Penn State. He has also completed coursework in control systems theory, physics, chemistry, and material science in addition to electromagnetic theory. His current research interests are in the area of antennas and computational electromagnetics with an emphasis on hybrid numerical methods and the finite difference time domain (FDTD) technique.